Electron spins in reduced dimensions: ESR spectroscopy on semiconductor heterostructures and spin chain compounds

Dissertation

zur Erlangung des akademischen Grades

Doctor rerum naturalium (Dr. rer. nat.)

vorgelegt

der Fakultät Mathematik und Naturwissenschaften
der Technischen Universität Dresden

von

Master of Science
Ferdinand Lipps

geboren am 28.08.1982 in Hildesheim

Eingereicht am 10.06.2011
Verteidigt am 31.08.2011

Gutachter: Prof. Dr. B. Büchner
Prof. Dr. T. Schäpers

Abstract

Spatial confinement of electrons and their interactions as well as confinement of the spin dimensionality often yield drastic changes of the electronic and magnetic properties of solids. Novel quantum transport and optical phenomena, involving electronic spin degrees of freedom in semiconductor heterostructures, as well as a rich variety of exotic quantum ground states and magnetic excitations in complex transition metal oxides that arise upon such confinements, belong therefore to topical problems of contemporary condensed matter physics.

In this work electron spin systems in reduced dimensions are studied with Electron Spin Resonance (ESR) spectroscopy, a method which can provide important information on the energy spectrum of the spin states, spin dynamics, and magnetic correlations. The studied systems include quasi one-dimensional spin chain materials based on transition metals Cu and Ni. Another class of materials are semiconductor heterostructures made of Si and Ge.

Part I deals with the theoretical background of ESR and the description of the experimental ESR setups used which have been optimized for the purposes of the present work. In particular, the development and implementation of axial and transverse cylindrical resonant cavities for high-field high-frequency ESR experiments is discussed. The high quality factors of these cavities allow for sensitive measurements on μm-sized samples. They are used for the investigations on the spin-chain materials. The implementation and characterization of a setup for electrical detected magnetic resonance is presented.

In Part II ESR studies and complementary results of other experimental techniques on two spin chain materials are presented. The Cu-based material Linarite is investigated in the paramagnetic regime above $T > 2.8$ K. This natural crystal constitutes a highly frustrated spin 1/2 Heisenberg chain with ferromagnetic nearest-neighbor and antiferromagnetic next-nearest-neighbor interactions. The ESR data reveals that the significant magnetic anisotropy is due to anisotropy of the g-factor. Quantitative analysis of the critical broadening of the linewidth suggest appreciable interchain and interlayer spin correlations well above the ordering temperature. The Ni-based system is an organic-anorganic hybrid material where the Ni^{2+} ions possessing the integer spin $S = 1$ are magnetically coupled along one spatial direction. Indeed, the ESR study reveals an isotropic spin-1 Heisenberg chain in this system which unlike the Cu half integer spin-1/2 chain is expected to possess a qualitatively different non-magnetic singlet ground state separated from an excited magnetic state by a so-called Haldane gap. Surprisingly, in contrast to the expected Haldane behavior a competition between a magnetically ordered ground state and a potentially gapped state is revealed.

In Part III investigations on SiGe/Si quantum dot structures are presented. The ESR investigations reveal narrow lines close to the free electron g-factor associated with electrons on the quantum dots. Their dephasing and relaxation times are determined. Manipulations with sub-bandgap light allow to change the relative population between the observed states. On the basis of extensive characterizations, strain, electronic structure and confined states on the Si-based structures are modeled with the program nextnano^3. A qualitative model, explaining the energy spectrum of the spin states is proposed.

Contents

Abstract **i**

Contents **iii**

List of Figures **vi**

List of Tables **viii**

1 Preface **1**

I Background and Experimental **5**

2 Principles of ESR **7**
- 2.1 The Resonance Phenomenon 7
- 2.2 ESR Spectrum 10
  - 2.2.1 The g-factor 11
  - 2.2.2 Relaxation Times 12
  - 2.2.3 Lineshape Properties 13
- 2.3 Effective Spin Hamiltonian 15
- 2.4 Spin-Orbit Coupling 16
- 2.5 d-electrons in a Crystal Field 17
- 2.6 Interactions 23
  - 2.6.1 Dipolar Coupling 23
  - 2.6.2 Exchange Interaction 23
  - 2.6.3 Superexchange 24
  - 2.6.4 Symmetric Anisotropic Exchange 25
  - 2.6.5 Antisymmetric Anisotropic Exchange 25
  - 2.6.6 Hyperfine Interaction 26

3 Experimental **27**
3.1 Setup for Experiments at 10 GHz 27
3.2 Implementation of an EDMR Setup 29
3.2.1 Basic Characterization 31
3.3 High Frequency Setup 31
3.3.1 Millimeter Wave Vector Network Analyzer 33
3.3.2 Waveguides and Cryostats 34
3.4 Development of the Resonant Cavity Setup 35
3.4.1 Mode Propagation 38
3.4.2 Resonant Cavity Modes 40
3.4.3 Resonant Cavity Design 41
3.4.4 Resonant Cavity Sample Stick 45
3.4.5 Experimental Characterization 47
3.4.6 Performing an ESR Experiment 53

II Quasi One-Dimensional Spin-Chains **57**

4 Motivation **59**

5 Quasi One-Dimensional Systems **61**
5.1 Magnetic Order and Excitations 63
5.2 Competing Interactions 64
5.3 Haldane Spin Chain 66

6 Linarite **69**
6.1 Structure 70
6.2 Magnetization and ESR 71
6.3 NMR 79
6.4 Summary and Conclusion 81
6.5 Outlook 82

7 The Ni-hybrid $NiCl_3C_6H_5CH_2CH_2NH_3$ **83**
7.1 Structure 83
7.2 Susceptibility and Magnetization 85
7.3 ESR 88
7.4 Further Investigations 95
7.5 Summary and Conclusion 96

8 Summary **99**

III SiGe Nanostructures **101**

9 Motivation **103**

10 SiGe Semiconductor Nanostructures **107**
10.1 Background 107
10.1.1 Silicon and Germanium 107
10.1.2 Epitaxial Growth of SiGe Heterostructures 109
10.1.3 Strain 111
10.1.4 Band Deformation 112
10.2 Sample Structure and Characterization 114

11 Modelling of SiGe/Si Heterostructures **119**
11.1 Program Structure 120
11.2 Implementation of Si/Ge System 121
11.3 Results 123
11.3.1 Single Quantum Dot 123
11.3.2 Multiple Quantum Dots 127
11.4 Discussion 130
11.5 Summary 132

12 ESR Experiments on Si/SiGe Quantum Dots **135**
12.1 ESR on Si Structures 135
12.2 Experimental Results 137
12.2.1 Samples grown at 600°C 138
12.2.2 Samples grown at 700°C 139
12.2.3 T_1-Relaxation Time 143
12.2.4 Effect of Illumination 145
12.3 Discussion 148
12.3.1 Quantum Dots 149
12.3.2 Assignment of ESR Lines 150
12.3.3 Relaxation Times 153
12.3.4 Donors in Heterostructures 153
12.4 Summary 156

13 Summary and Outlook **157**

Bibliography **163**

Acknowledgements **176**

List of Figures

2.1 Zeeman splitting 8
2.3 ESR spectrum 10
2.4 Orbitals in a crystal field 18
2.5 Energy splitting in crystal field 18
2.7 $3d^8$ spin configuration 19
2.8 Single ion anisotropy 22
2.9 Schematic AFM, FM superexchange 24

3.1 ESR X-band setup 28
3.2 EDMR X-band setup 30
3.3 EDMR on Si diode 32
3.4 Working principle of the MVNA 33
3.6 Resonance peak of cylindrical resonator 36
3.8 Rectangular resonator: TE_{102} mode 40
3.9 Cylindrical resonator: TE_{011} and TE_{012} mode 42
3.10 Coupling to axial and transverse resonator 44
3.11 Probestick with resonant cavity 46
3.12 Axial and transverse resonant cavity 47
3.13 V-band resonance modes 49
3.14 Shift of f_0 and Q with temperature 51
3.16 Resonator at 83 GHz 52
3.17 Shift of f_0 due to sample holders 53
3.18 Q-factor correction 54

5.1 Schematic competing interactions in spin chains 64
5.2 Schematic energy gap 66

6.1 Crystal structure Linarite 70
6.3 Linarite: ESR spectra at 93 GHz 71

6.4 Linarite: Temperature dependence of inverse susceptibility . . . 72
6.5 Linarite: Magnetic field dependence of magnetization 73
6.6 Linarite: Temperature dependence of g-factors and linewidth . . 74
6.7 Linarite: Critical part of linewidth 75
6.8 Linarite: NMR linewidth 80

7.1 Crystal structure Ni-hybrid 84
7.2 Ni-hybrid: Susceptibility vs. temperature 85
7.3 Ni-hybrid: Magnetization vs. magnetic field 86
7.4 Ni-hybrid: Spin-susceptibility 88
7.5 Ni-hybrid: ESR spectra at 93 GHz 89
7.6 Ni-hybrid: Field dependence of ESR spectra 90
7.7 Ni-hybrid: Resonance modes 91
7.8 Ni-hybrid: Zero field μSR 95

10.1 Bandstructure Si and Ge 108
10.2 Schematic of Ge island growth 109
10.4 Type II band alignment 111
10.5 Overview sample structure 114
10.6 AFM image and statistical analysis 116
10.7 TEM analysis 116

11.2 Uniaxial strain profile 124
11.3 Conduction band profile single dot 124
11.4 Wave functions: s- and p-like-state 125
11.5 Wave functions: Size and magnetic field 127
11.6 Dots 80 nm: Conduction band profiles 128
11.7 Dots 200 nm: Conduction band profiles 129

12.1 Comparison of ESR spectra 137
12.3 ESR spectra: single peak 138
12.4 ESR specra: double peak 140
12.5 Angular dependence of g-factor 141
12.7 Power dependence 143
12.8 ESR spectra at selected microwave powers 144
12.10 Photoluminescence SiGe nanostructures 145
12.11 Illumination with sub-bandgap light 146

List of Tables

3.1 Characteristics of waveguides 40
3.2 Characteristics of resonant cavities 48

12.1 SiGe quantum dots: g-factors 139

CHAPTER 1

Preface

The technological development in the semiconductor industry is approaching the limit, in which the size of the fundamental devices is in the range of nanometers. Besides the technological challenge associated with the physics of material growth, at dimensions that small, quantum mechanical properties become relevant. In order to further increase information density without reducing the size of the system and in order to facilitate low energy operations, more complex components have to be developed. One way to achieve this is to facilitate not only the charge, but also the (electron) spin [1]. The concept of electronics based on spin is called spintronics.

Research on spintronics has developed into a diverse field. Phenomena of magnetic order [2], injection of spin between different materials and spin transport [3, 4] are among the topics under intense investigation. Persistent magnetic and electric states can be manipulated by electric and magnetic fields [5, 6]. Spintronics is closely related to the field of quantum computation which makes use of the quantum nature of a spin for logic operations. It was also proposed that semiconductor systems provide a good material system to facilitate quantum computational operations [7]. Logic operations have also been demonstrated in magnetically ordered systems [8]. For spin transport, spin storage and spin operations the timescales on which spin states are preserved and the timescales on which spins can be manipulated coherently are crucial. In order to develop spintronic devices it is necessary to understand the spin-physics in different materials. Processes causing energy relaxation between spin states or destroy spin coherence can originate from spin-orbit coupling or scattering effects on boundaries and impurities as well as energy exchange with the environment of the (electron) spin. Furthermore it is important to identify systems with competing interactions which can lead to externally tunable ground states.

In this work different types of low-dimensional systems were investigated with Electron Spin Resonance (ESR) spectroscopy. The systems can be classified as (i) semiconductor heterostructures and (ii) insulating crystals with magnetic ions.

In the semiconductor systems, the lattice structure consists of the single host atoms Si or Ge forming a uniform three-dimensional crystal. By combining different materials the electronic band structure is altered. The electronic properties depend on strain within the structures, the specific bandstructure of the host materials and band offsets between them. This way, the electrons (and holes) populating the bands can become confined to two-dimensional quantum wells, one-dimensional channels and quasi zero-dimensional quantum dots.

In the insulating crystals, the second material class investigated, the crystal structure is built from several different elements. The localization of an electron is not realized by a local confining potential of the band structure. Instead electrons are bound to certain ions in the crystal. These magnetic ions can interact through different mechanisms with each other. If the strength of the interactions is much stronger along defined crystallographic directions the dimensionality of the electronic structure relevant for the magnetism is effectively reduced. These low-dimensional systems can be two-dimensional lattices, one-dimensional spin chains or quasi zero-dimensional quantum magnets. Here the coherence of the electronic states and their low energy excitations are confined to the spin sector only, not involving charge degrees of freedom.

Although the magnetic properties for the two classes of materials investigated in this thesis are fairly different, the electron spin resonance (ESR) technique offers a powerful method to investigate both classes of materials. ESR directly probes static and dynamic properties of an electron system in the response to a magnetic field. Depending on the details of the experiments, information about the local spin environment, relevant interactions as well as dephasing and relaxation times can be extracted.

This thesis is structured in three parts. The first part provides the theoretical background of the ESR phenomena. The experimental developments and the implementation of new setups are discussed. In Part II investigations on the low-dimensional Cu-chain Linarite ($PbCuSO_4(OH)_2$) and an organic-anorganic hybrid system based on Ni ($NiCl_3C_6H_5CH_2CH_2NH_3$) are presented. Part III deals with the material system made from Si and Ge. The experiments on and the modeling of self-assembled Si/SiGe nanostructures is discussed.

Part I

Background and Experimental

2 **Principles of ESR**

2.1 The Resonance Phenomenon 7
2.2 ESR Spectrum 10
2.3 Effective Spin Hamiltonian 15
2.4 Spin-Orbit Coupling 16
2.5 *d*-electrons in a Crystal Field 17
2.6 Interactions 23

3 **Experimental**

3.1 Setup for Experiments at 10 GHz 27
3.2 Implementation of an EDMR Setup 29
3.3 High Frequency Setup 31
3.4 Development of the Resonant Cavity Setup 35

CHAPTER 2

Principles of ESR

Electron Spin Resonance (ESR) is the phenomenon of reorientation of electron spins in a magnetic field through the interaction with electromagnetic radiation. As a spectroscopic technique ESR was developed in the 1940s and soon became an important tool in solid state physics. As with any spectroscopy its frequency has to be relevant for the energy or time scale of the process under investigation. The energy splitting between electron spin states in a typical laboratory magnetic field translates to wavelengths in the microwave range.

In this chapter the fundamental physics of the ESR phenomena is discussed. Starting with the behavior of a free electron in a magnetic field the basic properties of ESR are illustrated. The role of spin-orbit coupling, the interaction of crystal fields and the interaction between electrons are discussed with regards to the systems investigated in Part II and Part III of this work. The theoretical background is mainly based on the books by Abragam and Bleaney [9], Poole [10], Blundell [11] as well as Kittel [12] and Ashcroft and Mermin [13].

2.1 The Resonance Phenomenon

To illustrate the principle of ESR one can first consider the case of a single electron in a magnetic field. The interaction of an electron with a magnetic

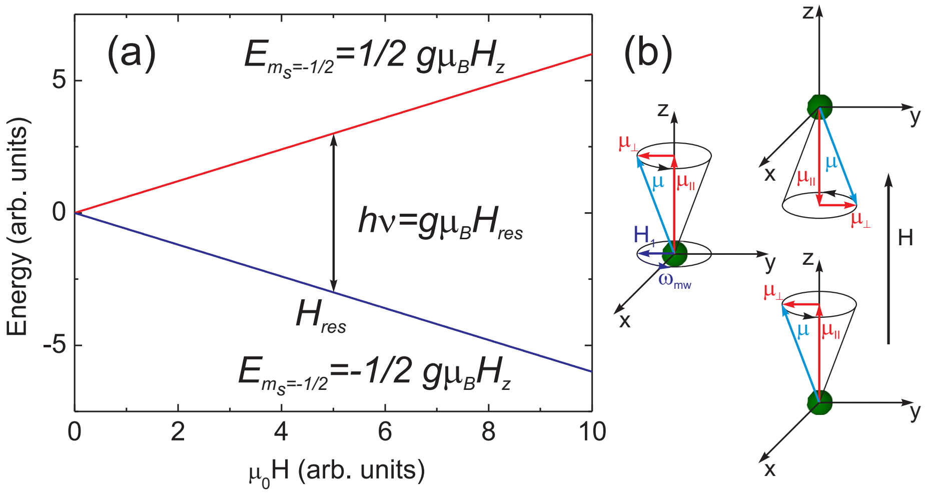

Figure 2.1: (a) Zeeman levels are split in energy in a magnetic field according to their spin state $S = \pm 1/2$. (b) Classical picture of the spin-flip. A magnetic moment $\boldsymbol{\mu}$ is precessing in the external magnetic field along z-direction. When the microwave magnetic field H_1 precesses with the same frequency ω_{mw} perpendicular to the external magnetic field, the magnetic moment is turned towards the opposite z-direction.

field is ascribed to the electron spin. Although the spin **S** is a purely quantum mechanical effect it is associated with an intrinsic magnetic moment. This magnetic moment $\boldsymbol{\mu}$ can be written as

$$\boldsymbol{\mu} = -g\mu_B \mathbf{S} \tag{2.1}$$

g is the so called g-factor and μ_B the Bohr Magneton (see below). The g-factor of the free electron is $g \approx 2.00232$. The deviation from 2 originates theoretically from a series expansion about the fine structure constant α and is explained by the emission and reabsorption of virtual phonons.

When an external magnetic field **H** is applied to the electron along an arbitrary direction z the spin becomes quantized with respect to the field direction. The energy of the system is then quantized as

$$E = g\mu_B \mathbf{S} \cdot \mathbf{H} = g\mu_B m_S H_z \tag{2.2}$$

Where m_S is the eigenvalue of the z-component S^z of the spin operator **S**. The energy splitting ΔE between different spin states m_S in an applied magnetic field is known as the Zeeman splitting. There are $2S$+1 Zeeman levels for the different values of m_S with $-S \leq m_S \leq S$. For the simple case of a free electron with $S = 1/2$ it follows $m_S = \pm 1/2$. For such a system with only two eigenstates the states are usually referred to as up- and down-spin. A transition between the different Zeeman levels can be induced through absorption of electromagnetic radiation matching the energy difference ΔE [Fig. 2.1(a)].

$$\Delta E = \hbar\omega = h\nu = g\mu_B \mid \Delta m_S \mid H_z \tag{2.3}$$

Classically the spin can be thought of as a magnetic moment $\boldsymbol{\mu}$ precessing around the applied external magnetic field [see Fig. 2.1(b)]. The microwave radiation is linearly polarized and its magnetic field vector $\mathbf{H}_1$ is perpendicular to the external magnetic field vector $\mathbf{H}$ along the z-direction. The linearly polarized wave can be thought of as the superposition of two circular polarized waves precessing clockwise and counterclockwise around $\mathbf{H}$. When the resonance conditionin equation (2.3) is fulfilled $\mathbf{H}_1$ precesses with the same frequency ω_{mw} around $\mathbf{H}$ as $\boldsymbol{\mu}$. The magnetic moment $\boldsymbol{\mu}$ is then turned to the opposite z-direction by precessing about $\mathbf{H}_1$. This corresponds to the spin-flip from spin-down to spin-up.

In addition to the quantum mechanical property spin an electron is characterized by charge $-e$ and mass m_e. With those two properties the behavior of the electron can be described classically. An orbital motion of the electron around a positive charge results in an angular momentum. At the same time the circling charge represents a current loop which results in a magnetic moment antiparallel to the angular momentum. The (negative) magnetic moment is called Bohr Magneton μ_B:

$$\mu_B = \frac{e\hbar}{2m_e} \tag{2.4}$$

In the quantum mechanical description electrons bound to the core of the atom exhibit discrete energy states which correspond to the occupation of certain orbitals. With each orbital there is an orbital angular momentum $\boldsymbol{\mu}_L$ associated. The eigenvalues or quantum numbers for the orbital momentum operator are $L(L+1)$ for $\mathbf{L}^2$ and m_l for L^z. Any electron in the environment of an atom is characterized by its intrinsic spin angular momentum and its orbital angular momentum.

For the magnetic dipole absorption in a general spin system the quantum

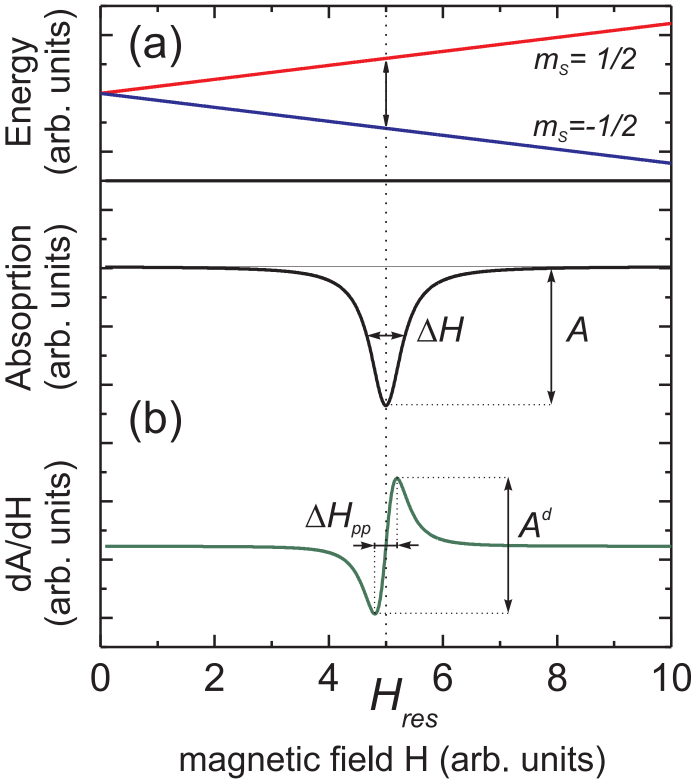

Figure 2.3: The Zeeman splitting in a magnetic field for a spin with $S = 1/2$ (a). The absorption spectrum and its derivative are shown (b). The absorption spectrum is centered at the resonance field H_{res} with the amplitude A and FWHM linewidth ΔH. The derivative of the absorption spectrum dA/dH is characterized by the peak-to-peak linewidth ΔH_{pp} and its amplitude A^d.

mechanical selection rules are

$$\Delta L = 0, \quad \Delta S = 0, \quad \Delta m_S = \pm 1 \tag{2.5}$$

2.2 ESR Spectrum

When performing ESR spectroscopy the resonance condition in equation (2.3) is fulfilled, when the energy difference at a certain magnetic field is matched by the energy of the microwave radiation of a certain frequency. Often the actual experiment is performed by applying microwaves at a fixed frequency (and intensity) and sweeping the magnetic field. When the resonance condition is fulfilled microwave radiation is absorbed. This absorption spectrum (Fig. 2.3) provides information about the spin system.

2.2.1 The g-factor

From the resonance field H_{res} the g-factor can be determined as

$$g = \frac{h}{\mu_B} \frac{\partial \nu}{\partial H_{res}} \tag{2.6}$$

If there is no zero-field energy gap Δ (cf. Section 2.5) it is valid:

$$g = \frac{h}{\mu_B} \frac{\nu}{H_{res}} \tag{2.7}$$

As a rule of thumb it is useful to remember:

$$g \approx \frac{1}{14} \frac{\nu[\mathrm{GHz}]}{H_{res}[\mathrm{T}]} \tag{2.8}$$

In general the g-factor is not necessarily isotropic and has to be treated as a tensor $\tilde{g}$. The $\tilde{g}$-tensor can be regarded as a spectroscopic factor of the ESR experiment. It provides information about the energy states of the spin system. For the free electron the isotropic g-factor is close to 2. For electrons in an atom, this value can shift from 2 due to the spin orbit coupling. If the atom is placed in an electrostatic field of surrounding atoms, the orbital energy levels shift. Eventually the $\tilde{g}$-tensor becomes anisotropic. If there is some form of interaction between different magnetic atoms, magnetic order can occur in the spin system and the resonance field can shift significantly. Because of those very diverse effects, one initially refers to the $\tilde{g}$-tensor as an effective g-factor, or simply g-factor, when describing an ESR-experiment. For many systems it is sufficient to describe the g-factor as a tensor in its principal axis system.

$$\tilde{g} = \begin{pmatrix} g_x & 0 & 0 \\ 0 & g_y & 0 \\ 0 & 0 & g_z \end{pmatrix} \tag{2.9}$$

with the effective g-factor

$$g = \sqrt{g_x^2 \sin^2\Theta \cos^2\Phi + g_y^2 \sin^2\Theta \sin^2\Phi + g_z^2 \cos^2\Theta} \tag{2.10}$$

Θ and Φ being the angles between the magnetic field with respect to the principal axis of the $\tilde{g}$-tensor. Equation (2.10) reduces for $g_x = g_y$ to

$$g = \sqrt{g_x^2 \sin^2\Theta + g_z^2 \cos^2\Theta} \tag{2.11}$$

By measuring the angular dependence of the effective g-factor it is possible to identify the $\tilde{g}$-tensor describing the physical system.

2.2.2 Relaxation Times

The transition between two spin states at the resonance field is not infinitesimal sharp as would be described by a δ-function. Instead for any excited spin state there exists a finite lifetime τ. It follows from the Heisenberg uncertainty principle [14] that the transition energy has a certain range $\Delta E \geq \hbar\tau^{-1}$. The probability for the state to be found at a certain energy translates into a finite linewidth for the ESR transition:

$$\Delta H \propto \frac{\hbar}{g\mu_B}\tau^{-1} \tag{2.12}$$

This natural linewidth depends only on the finite lifetime of a spin state and is the lower limit observed for the linewidth in an ESR experiment.

Since in a regular ESR experiment the measurement is performed on a macroscopic sample the overall response of the system is determined. The continuous wave (cw) ESR spectrum is that of a large ensemble of spins embedded in a solid. Macroscopically the response of a spin ensemble is that of the sum of its magnetic moments which is given by the magnetization M, which is actually defined as the density of magnetic moments. The classical description of the relaxation process of the magnetization in a magnetic field is given by the Bloch equations [15].

$$\frac{\partial \mathbf{M}(t)}{\partial t} = \frac{g_e\mu_B}{\hbar}(\mathbf{M}\times\mathbf{H}) - (\mathbf{M}-\chi_0\mathbf{H})\left(\frac{1}{T_1}e_\parallel + \frac{1}{T_2}(e_{\perp,1}+e_{\perp,2})\right) \tag{2.13}$$

where $e_\parallel, e_{\perp,1}, e_{\perp,2}$ are the unit vectors parallel and perpendicular to the magnetic field vector. Two relaxation times, T_1 and T_2, for the magnetization parallel and perpendicular to the magnetic field, are defined respectively.

T_1 describes the decay of the longitudinal magnetization $M_\parallel$. The T_1-relaxation time or spin-lattice relaxation time is the time for a spin to reverse its orientation in a magnetic field. Such a transition is associated with a change in the energy of the spin. In general an energy transfer to the spin system can be provided by thermal fluctuations (phonons) and magnetic excitations as well as by kinetic energy from conduction electrons.

T_2 describes the decay of the transverse magnetization $M_\perp$. The T_2-time is associated with the coherence of a spin state. The phase relaxation is not (necessarily) connected with a change in energy. In that sense it is a single-spin property. The loss of phase coherence can be caused for example by scattering events.

The T_2^*-time is the spin-dephasing time of a spin ensemble. For a spin ensemble there can be slight differences between the internal magnetic fields at the spin sites and there can be interactions between the spins. Because of this the coherence times are slightly different for the individual spins. The spin ensemble loses the spin coherence faster than an individual spin.

While the relaxation process always requires an energy transfer with the environment, the dephasing is not associated with a change in energy. Therefore usually $T_1 \gg T_2$. However, if electrons are mobile, e.g. in a conduction band of a semiconductor, sometimes, due to spin-orbit coupling, T_1 cannot exclusively be associated with a change in state occupation and eventually $T_1 \sim T_2$ [16].

In pulsed ESR experiments, certain microwave pulse sequences are applied to the sample at a fixed magnetic field. This way T_1- and T_2-time can be measured directly. This technique is very similar to NMR-spectroscopy (see e.g. [17]), but spin systems usually require relatively long coherence times to be measurable with pulsed ESR. From the ESR signal in a cw ESR experiment, information about T_1-relaxation- and T_2^*-dephasing-time can be extracted. ESR results presented in this work were exclusively determined with cw ESR experiments.

2.2.3 Lineshape Properties

The T_2^*-time can be directly related to the linewidth of a cw ESR experiment. However, different spin-spin interactions, discussed in Section 2.6, have an effect on the ESR linewidth. Individual spins are subjected to different internal magnetic fields, due to the magnetic dipoles of the spins in their vicinity. Then the individual ESR resonances occur at slightly different external magnetic fields. This translates into a statistical distribution of absorptions (each with the natural linewidth) around H_{res}. This effect is called *inhomogeneous broadening*. The linewidth has a Gaussian form.

$$f(H) = \sqrt{\frac{2}{\pi}} \frac{1}{\Delta H} \exp\left(-2\frac{(H-H_{res})^2}{\Delta H^2}\right) \tag{2.14}$$

An additional broadening effect is caused by a form of resonance interaction between identical spins. A magnetic dipole precessing in the external field emits radiation causing resonance transitions at identical spins. This interaction shortens the lifetime of an individual spin and the broadening is not completely inhomogeneous.

Besides magnetic dipole interaction the exchange interaction can cause broadening and narrowing of the line. If the exchange interaction is isotropic

$$\mathscr{H} = J_{ij}\mathbf{S}_i \cdot \mathbf{S}_j \tag{2.15}$$

the effect on the linewidth is that of an *exchange narrowing*. It results from dipole reorientations due the interaction with neighboring spins. The local internal field is effectively reduced and the inhomogeneous broadening narrowed by the exchange. Similarly if electrons are delocalized the time-averaged magnetic field at the spin is reduced. This effect is called *motional narrowing*. For both effects the line is described by a Lorentzian form.

$$f(H) = \frac{2}{\pi}\frac{\Delta H}{\Delta H^2 + 4(H - H_{res})^2} \tag{2.16}$$

If the exchange between the spins is anisotropic as described by

$$\mathscr{H} = \mathbf{S}_i \cdot \tilde{J}_{ij} \cdot \mathbf{S}_j \tag{2.17}$$

the result is a broadening of the line, similar to the magnetic dipole interaction discussed before.

In Fig. 2.3(b) a Lorentzian absorption line centered at the resonance field H_{res} is shown. The amplitude $A = f(H_{res})$ and the full-width-at-half-maximum (FWHM) linewidth ΔH are indicated. When a modulation technique is used for the ESR experiment the derivative of the Lorentzian is characterized by the peak-to peak linewidth $\Delta H_{pp} = \frac{1}{\sqrt{3}}\Delta H$ and its amplitude A^d.

The absorption of energy by the resonating spin system is described by the imaginary part of the dynamic susceptibility χ'' in response to the microwave magnetic field [9]. The integral over the ESR line is proportional to the local static spin susceptibility.

$$I \propto \chi_{spin} \int_{-\infty}^{+\infty} f(H)dH \tag{2.18}$$

If the lineshape can be described by Lorentzian or Gaussian form, its integral is proportional to linewidth times amplitude

$$I \propto A\Delta H \tag{2.19}$$

And for the derivative

$$I \propto A^d \Delta H_{pp}^2 \tag{2.20}$$

These relations make it easy for the experimentalist to determine the spin susceptibility from fits to the ESR-spectrum. Since its amplitude and eventually its linewidth depend on experimental conditions, absolute values of the spin susceptibility have to be determined from simultaneous measurements on standard samples or normalization to complementary measurements.

One experimental condition is the microwave power. Imagine a spin system in a magnetic field in thermal equilibrium. The different Zeeman levels at a given temperature are populated according to Boltzmann statistics. The probability for a transition from a down state, under the absorption of energy, and the transition from an up state, under induced emission, are equal. The ESR amplitude depends on the difference between photons emitted and absorbed, thus, the population difference between both states. For low microwave powers the system is in the thermal equilibrium. This can be imagined as an induced absorption and a relaxation of the same spin on the timescale of the state's lifetime. When higher microwave powers are applied, translating into more microwave quanta, an emission is induced before the excited spin state relaxes back. The ESR signal saturates and eventually decreases. This saturation technique allows the T_1-time of a spin ensemble to be determined with cw ESR [10]. This technique was used to estimate the saturation time of electrons on SiGe quantum dots as presented in Part III.

2.3 Effective Spin Hamiltonian

In an ESR experiment a spin system is probed in its response to an external magnetic field. This response is described by the Zeeman energy. The interactions of the spins with the lattice and other spins are usually larger than the Zeeman energy. For an ESR experiment it is often sufficient to combine the different interactions in an effective Hamiltonian. That means that the observed features in an ESR experiment are analyzed according to the fundamental interactions, as spin-orbit coupling, crystal-field and hyperfine splitting. Also the different spin-spin interactions have to be considered. A general effective Hamiltonian can be defined as

$$\mathscr{H}_{\text{eff}} = \mathscr{H}_Z + \mathscr{H}_{SO} + \mathscr{H}_{CF} + \mathscr{H}_{SS} + \mathscr{H}_{HF} \tag{2.21}$$

Depending on the system under investigation, different parts of the Hamiltonian are considered while others can be neglected. In the next sections, terms relevant for the systems investigated in this work are discussed.

2.4 Spin-Orbit Coupling

If we consider multiple electrons in the vicinity of the nucleus, there exists electrostatic repulsion between the electrons and dipole-dipole interaction between their spins. Additionally there exists an interaction between the spin (magnetic moment) and the movement of the electron in the electrostatic potential of the nucleus. Classically for a charge moving in an electric field, the electric field transforms into a magnetic field in the rest frame of the charge. This magnetic field acts on the spin moment. A general Hamiltonian for this interaction is written as

$$\mathscr{H}_{SO} = \frac{\hbar}{2m^2c^2} \nabla V(\mathbf{r}) \times \mathbf{p} \cdot \mathbf{S} \tag{2.22}$$

where $V(\mathbf{r})$ is the electrostatic potential and $\mathbf{p}$ the momentum operator. With $\mathbf{L} = \mathbf{r} \times \mathbf{p}$ it follows

$$\mathscr{H}_{SO} \propto \mathbf{L} \cdot \mathbf{S} \tag{2.23}$$

As discussed before, the orbital motion of an electron itself is characterized by the angular momentum operator **L**. The coupling 2.23 between angular orbital momentum and spin momentum is known as spin-orbit coupling. For weak spin-orbit coupling (LS-coupling or Russel-Saunders-coupling [18]) the paramagnetic response of an atom, as given by the Zeeman term, depends on the total orbital angular momentum and the total spin angular momentum for which the individual moments of electrons k in incomplete shells are added up.

$$\mathbf{L} = \sum_k \mathbf{L}_k \tag{2.24}$$

$$\mathbf{S} = \sum_k \mathbf{S}_k \tag{2.25}$$

For the LS-coupling the total angular momentum **J** is given as the sum of the total orbital momentum and the total spin momentum

$$\mathbf{J} = \mathbf{L} + \mathbf{S} \tag{2.26}$$

When the effect of spin-orbit coupling is considered relevant in the spin system the electron g-factor g_e has to be replaced by the Landé factor g_J defined as

$$g_J = \frac{3}{2} - \frac{L(L+1) - S(S+1)}{2J(J+1)} \tag{2.27}$$

The Zeeman energy for the ion is

$$E = \mu_B(\mathbf{L} + g_e\mathbf{S}) \cdot \mathbf{H} = \mu_B g_J \mathbf{J} \cdot \mathbf{H} \tag{2.28}$$

An effective Hamiltonian is defined to parameterize the spin-orbit coupling in case of LS-coupling as

$$\mathscr{H}_{LS} = \lambda \mathbf{L} \cdot \mathbf{S} \tag{2.29}$$

where λ gives the coupling strength. λ is positive for less than half filled shells and negative for more than half filled shells.

Spin-orbit coupling is not only relevant when looking at individual atoms. In semiconductors (and metallic structures) electrons can move constraint within certain bands. The general Hamiltonian defined in equation (2.23) also describes the spin-orbit coupling of electrons in the **k**-dependent (electrostatic) band potential. In semiconductors, the spin-orbit coupling depends, besides the host material, on the crystal symmetry. The group IV semiconductors Si and Ge, investigated in Part III, are centrosymmetric crystals and electrons in the populated bands are not subjected to (a significant) spin-orbit coupling. However by creating heterostructures the inversion symmetry of the crystal structure is broken. One effect which can cause spin-orbit coupling is the *structural inversion symmetry*. The asymmetry is caused by the combination of different materials or asymmetric electric fields [16]. The resulting spin splitting is described as the Byshkov-Rashba effect [19, 20].

2.5 *d*-electrons in a Crystal Field

Atoms which shells are not completely filled yield a (para)magnetic response. Because of interactions between magnetic ions magnetic ordering can occur in systems on the energy scale of the magnetic exchange. When dealing with the magnetism of transition metal ions Cu^{2+} and Ni^{2+}, as relevant for the investigations presented in Part II, the not completely filled electron orbitals contributing to the magnetism are of the $3d$-shell.

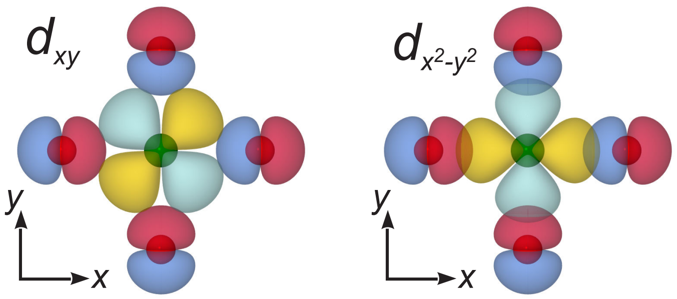
d_{xy}
y
x
$d_{x^2\text{-}y^2}$
y
x

Figure 2.4: Schematic view of a cut through the xy-plane of an atom in an octahedral crystal field. The d_{xy}-orbitals of the central atom point between the p_x-,p_y-orbitals of the surrounding atoms. The $d_{x^2-y^2}$-orbitals overlap. The d_{xy}-configuration is energetically favorable.

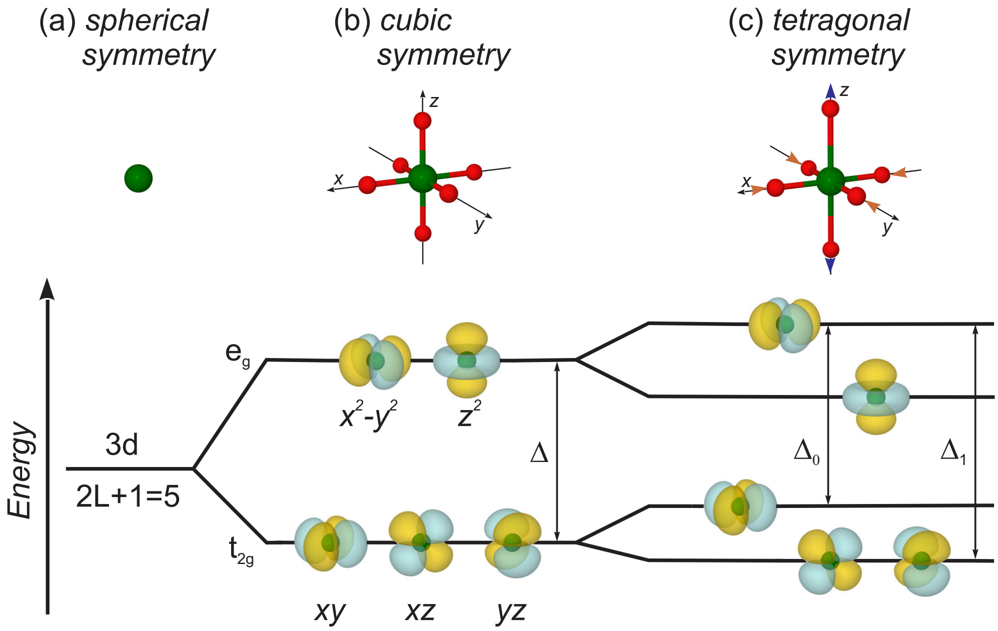
(a) *spherical symmetry*
(b) *cubic symmetry*
(c) *tetragonal symmetry*
z
x
y
z
x
y
Energy
3d
2L+1=5
e_g
t_{2g}
x^2-y^2
z^2
xy
xz
yz
Δ
Δ_0
Δ_1

Figure 2.5: In the free ion all energy states are degenerate. In a cubic symmetry the t_{2g}-orbitals are lowered in energy as compared to the e_g-orbitals as schematically explained in Fig. 2.4. An uniaxial expansion or a biaxial compression causes a tetragonal symmetry, in which the energy levels are split further.

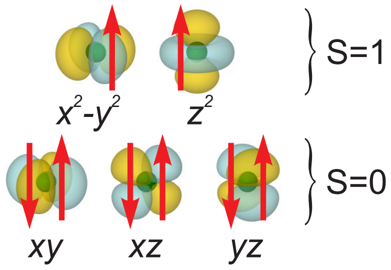

Figure 2.7: $3d^8$ spin configuration for a Ni^{2+}-ion in an octahedral crystal field. The t_{2g}-levels are completely filled, resulting in a total spin of $S = 0$. The e_g-levels are only occupied by two electrons, yielding a total spin of $S = 1$.

In many low-dimensional spin systems the transition metal ions form a covalent bonding with elements from the 6th or 7th group of the periodic table (e.g. O or Cl). The orbitals of those elements contributing to the bonding are p-orbitals. When orbitals overlap there is an electrostatic repulsion which changes the energy as compared to the free ion. Fig. 2.4 shows schematically the d_{xy}- and the $d_{x^2-y^2}$-orbital on the central atom surrounded by four atoms with a p_x- or a p_y-orbital in the xy-plane. This corresponds to the xy-plane of an ion in a octahedral crystal field. While the $d_{x^2-y^2}$-orbital overlaps with the surrounding orbitals, the d_{xy}-orbital points in between. The d_{xy}-configuration is energetically favorable because of the smaller electrostatic repulsion.

In a tetrahedral configuration the p-orbital atoms are placed on the diagonals and therefore the energy states are reversed.

The energy levels with the corresponding orbitals of the d-shell are shown schematically for different crystallographic configurations in Fig. 2.5. For the free ion the symmetry is spherical and the five levels are degenerate in energy. If the same ion is placed in an octahedral crystal field the e_g- and t_{2g}-levels are split by an energy difference Δ. This was explained above phenomenologically on the basis of the d_{xy}- and $d_{x^2-y^2}$-orbital. An uniaxial elongation of the octahedra or a biaxial compression distorts the octahedra to tetragonal symmetry. The energy levels are split further. The distortion shown corresponds to a single ion anisotropy $D > 0$. For additional distortions the symmetry is reduced further. Eventually all energy levels are split.

Let us consider the implications for the spins states of the $3d$-ions due to the crystal field environment. As an example let us choose Ni^{2+} with the

$3d^8$-configuration in an octahedral crystal field (Fig. 2.7). For $3d$-ions the crystal field energy is much larger than the spin-orbit coupling [11]. This results in an occupation of orbitals in the following way: The three t_{2g}-levels are filled completely with two spins each. The remaining two spins occupy the e_g-levels, which are half-filled with spins aligned parallel. The spin state expected is characterized by $S = 1$ and $L = 3$ yielding a $J = 4$. However the experimentally observed value for the magnetic moment does not agree with this. Responsible for this is the quenching of the orbital moment: The t_{2g}-levels are completely filled so these orbital do not contribute to the magnetism. The operator L^z acting on the e_g-wave functions gives the following results [21, 22]:

$$L^z|d_{z^2}\rangle = 0 \quad L^z|d_{x^2-y^2}\rangle = 2i|d_{xy}\rangle \tag{2.30}$$

and therefore all expectation values are zero:

$$\langle d_{z^2}|L^z|d_{z^2}\rangle = 0 \quad \langle d_{x^2-y^2}|L^z|d_{x^2-y^2}\rangle = 2i\langle d_{x^2-y^2}|d_{xy}\rangle = 0 \tag{2.31}$$

Similarly, this holds for the operators L^x, and L^y and with that for $\mathbf{L}$. That means that the orbital moment vanishes in the case of $3d^8$-ion in an octahedral crystal field also for the e_g-levels. The orbital moment is said to be quenched and $J = S$. The effective magnetic moment is:

$$\mu_{eff} = g_J \mu_B \sqrt{J(J+1)} = g\mu_B \sqrt{S(S+1)} \tag{2.32}$$

Nevertheless the spin-orbit coupling cannot be neglected completely: In second order perturbation theory excited orbital states $|n\rangle$ are admixed to the ground state $|0\rangle$ via the orbital momentum operator $\mathbf{L}$ as described by $\mathcal{H} = -\lambda^2 \mathbf{S} \cdot \tilde{\Lambda} \cdot \mathbf{S}$ with

$$\Lambda_{ij} = \sum_{n \neq 0} \frac{\langle 0|L^i|n\rangle\langle n|L^j|0\rangle}{E_n - E_0} \tag{2.33}$$

with $\Delta = E_n - E_0$ the energy difference between the orbital states. Because of the mixing of orbital states the g-factors deviate from the free electron value according to the spin-orbit coupling λ and the energy splitting Δ. For an octahedral crystal field the g-factor (tensor) is isotropic with

$$g = g_e - 2\lambda/\Delta \tag{2.34}$$

If the octahedral symmetry is tetragonally distorted there is an energy difference between the states admixed by different components of $\mathbf{L}$. The corresponding energy splittings Δ_0, Δ_1 are indicated in Fig. 2.5. The g-factor tensor becomes anisotropic reflecting the axial symmetry of the distortion. For the $3d^8$ configuration it reads

$$g_{\parallel} = g_e - \frac{8\lambda}{\Delta_0} \tag{2.35}$$

$$g_{\perp} = g_e - \frac{8\lambda}{\Delta_1} \tag{2.36}$$

with $g_{\parallel}$ parallel to the distorted axis and $g_{\perp}$ perpendicular to it. The g-factor tensor is characteristic for the magnetic ion and its crystal field environment.

The energy splitting between spin states can be described defining the single ion anisotropy parameter $D_{ij} = \lambda^2 \Lambda_{ij}$ which in case of tetragonal symmetry is given as $D \propto \lambda^2/\Delta_1 - \lambda^2/\Delta_0$. The behavior of the spins states can then conveniently be described using an effective Hamiltonian. The Hamiltonian for a spin in a crystal field environment (and magnetic field) is given as

$$\mathcal{H} = \mathcal{H}_{CF} + \mathcal{H}_Z = \mathbf{S} \cdot \tilde{D} \cdot \mathbf{S} + \mu_B \mathbf{S} \cdot \tilde{g} \cdot \mathbf{H} \tag{2.37}$$

where $\tilde{D}$ is the single ion anisotropy tensor. With the diagonal form of the tensor, the crystal field splitting is usually given as [9]:

$$\mathcal{H}_{CF} = D\left((S^z)^2 - \frac{1}{3}S(S+1)\right) + E(S_+^2 - S_-^2) \tag{2.38}$$

where

$$D = D_{zz} - (D_{xx} + D_{yy})/2 \qquad E = (D_{xx} - D_{yy})/2 \tag{2.39}$$

and $\frac{1}{3}S(S+1)$ a constant which just shift the energy levels. D describes the axial anisotropy and E the transverse anisotropy of the spin system.

In the case of the symmetrical octahedral crystal field, the single ion anisotropy tensor is isotropic with $D_{xx} = D_{yy} = D_{zz}$. This results in $D = 0$ and $E = 0$. From this one can see that there is no preferential orientation for the spin. Alone the direction of the magnetic field determines the quantization axis. For a $S = 1$ state there are three projections $m_S = \pm 1, 0$ of the spin in a magnetic field with states $|\pm 1\rangle, |0\rangle$. In the octahedral crystal field environment the states are degenerate at zero-field and the energy splitting in an applied magnetic field is given by the Zeeman energy as shown in Fig. 2.8(a).

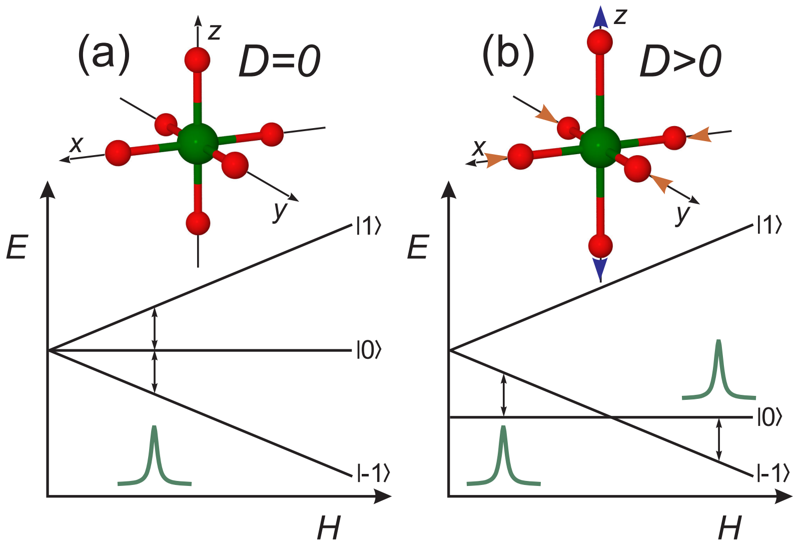

Figure 2.8: Effect of single ion anisotropy on the spin states and the Zeeman splitting. (a) For the octahedral crystal field configuration the spin states are degenerate at zero magnetic field. Only one ESR absorption is observed. (b) For a tetragonal distortion of the octahedra there is a zero-field splitting and two ESR absorptions are observed for the same frequency at different fields.

For a fixed microwave frequency, Zeeman transitions from $|-1\rangle \rightarrow |0\rangle$ and $|0\rangle \rightarrow |1\rangle$ occur at the same magnetic field [Fig. 2.8(a)].

When the octahedron is uniaxially distorted according to Fig. 2.8(b), $D_{zz} > D_{xx} = D_{yy}$ leads to $E = 0$ and $D > 0$. The positive D describes a splitting of the three projections $m_S = \pm 1, 0$ already in zero magnetic field. The ground state is the nonmagnetic singlet state $|0\rangle$. Since only the energy of the $|\pm 1\rangle$ states changes with magnetic field there is a crossing of $|-1\rangle$ with the non magnetic state $|0\rangle$. For higher fields than this critical field, $|-1\rangle$ has the lowest energy and is therefore the ground state of the system. With the same constant microwave frequency as applied before, two Zeeman transitions $|-1\rangle \leftrightarrow |0\rangle$ are possible which occur now at different magnetic fields. Due to the zero-field splitting the transition $|0\rangle \rightarrow |1\rangle$ is not possible at the same energy, but would require a larger microwave frequency. Therefore an ESR experiment is a highly sensitive tool to probe the local crystal field symmetry of a magnetic ion.

2.6 Interactions

2.6.1 Dipolar Coupling

When dealing with spins in a solid there exist different interactions between them. Thinking of spins as magnetic moments we can construct the magnetic dipolar or dipole-dipole interaction between two magnetic dipoles as

$$E = \frac{\mu_0}{4\pi r^3}\left(\boldsymbol{\mu}_1 \cdot \boldsymbol{\mu}_2 - \frac{3}{r^2}(\boldsymbol{\mu}_1 \cdot \mathbf{r})(\boldsymbol{\mu}_2 \cdot \mathbf{r})\right) \tag{2.40}$$

The energy depends on the relative orientation of the magnetic moments $\boldsymbol{\mu}$ and their distance $\mathbf{d}$. The energy for moments with $\mu \approx 1\mu_B$ and $d \approx 1\,\text{Å}$ is around $T = 1\,\text{K}$ [11]. The effect of magnetic dipole interactions on the linewidth was discussed before in Section 2.2.3 and may be relevant for the quantum dot systems investigated in Part III of this work.

2.6.2 Exchange Interaction

An interaction which can have a larger energy scale is the exchange interaction. Known from the Pauli exclusion principle, the total wave function consisting of the spatial and the spin wave function parts of two electrons, has to be antisymmetric under particle exchange. Since the linear combination of the spatial wave functions are a symmetric and an antisymmetric state there have to be two spin part wave functions as well: One being an antisymmetric singlet ($S = 0$) and the other a symmetric triplet ($S = 1$). There exists an energy difference between singlet and triplet states and the effective Hamiltonian for the spin-dependent part can be written as

$$\mathscr{H} = J\mathbf{S}_1 \cdot \mathbf{S}_2 \tag{2.41}$$

where the exchange constant J is defined as

$$J = \frac{E_T - E_S}{2} \tag{2.42}$$

If $J < 0$ the singlet energy is larger than that of the triplet state with $S = 1$. The spins are coupled ferromagnetically. For $J > 0$ the singlet state with $S = 0$ is favored and the ground state is antiferromagnetic.

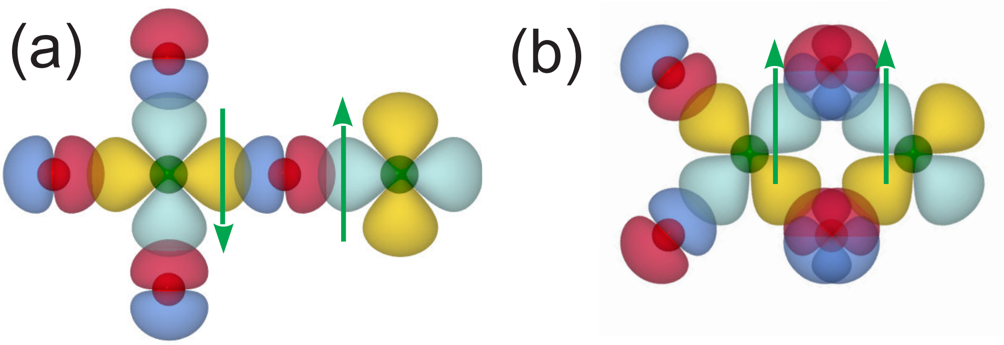

Figure 2.9: Schematic of AFM (a) and FM (b) superexchange. For a 180°-exchange path AFM is favored due to the overlap of the *d*-orbitals with one *p*-orbital. For 90° FM is dominant. Two *p*-orbitals contribute to the exchange.

When considering not only two spins but many spins each coupling to their neighbors the Heisenberg Hamiltonian [23, 24] follows.

$$\mathscr{H} = \frac{1}{2}\sum_{ij} J_{ij}\mathbf{S}_i \cdot \mathbf{S}_j \tag{2.43}$$

For the transition metal oxide system, as investigated in Part II, the exchange interaction is relevant. Usually the distances between neighboring magnetic ions are too large for a direct exchange, but the exchange can be mediated through orbitals of the surrounding atoms. This is called superexchange.

2.6.3 Superexchange

Microscopically the origin of the superexchange is explained by a second order perturbation theory within the Hubbard model [11, 25]. The exchange constant J_{ij} is defined as

$$J_{ij} \propto \frac{t_{\mathrm{eff}}^2}{U} \tag{2.44}$$

where t_{eff} is the effective hopping integral and U the on-site Coulomb interaction. The Goodenough-Kanamori-Anderson-rules [26, 27, 28, 29] indicate if the superexchange is antiferromagnetic or ferromagnetic.

The superexchange is visualized in a simplified comic-like way in Fig. 2.9. Two atoms (e.g. Cu) shown with their $d_{x^2-y^2}$-orbital are next to atoms in a

p_x- or p_y-orbital configuration (e.g. O). The two different colors of each orbital indicate the up- and down-spin configuration respectively. The Cu ion holds an effective spin of S=1/2, while all p-orbitals of the oxygen are completely filled. If there is an overlap between orbitals from different atoms the electrons can become delocalized if spins are aligned antiferromagnetically within this extended orbital, therefore lowering its kinetic energy. The unpaired spins of Cu align antiparallel with the oxygen spins. One can see that the two Cu spins align antiparallel if only a single p-orbital is involved in the superexchange. This is the case for a 180° exchange path shown in Fig 2.9(a) which is the strongest AFM superexchange coupling. In Fig. 2.9(b) the configuration is shown for a 90° exchange. Here the two different Cu spins couple to a p_x and a p_y-orbital of the same oxygen respectively. The oxygens p-orbitals are fully occupied. From one p-orbital respectively electrons can hop to the Cu d orbital if they have opposite spin to the electron on the Cu. Electrons at the oxygen can maximize their spin, which is energetically favorable, when the Cu spins are parallel. The superexchange is ferromagnetic.

In general different d-orbitals can contribute to the superexchange. Since the kinetic exchange term depends on the overlap with a single p-orbital AFM is favored for relatively small deviations from the FM 90°-exchange path already.

2.6.4 Symmetric Anisotropic Exchange

When the g-tensors of interacting magnetic ions are anisotropic the Hamiltonian describing the exchange can be written as:

$$\mathscr{H}_{AE} = \mathbf{S}_i \cdot \tilde{J}_{ij} \cdot \mathbf{S}_j \tag{2.45}$$

In that sense it is similar to magnetic dipole interaction [9].

2.6.5 Antisymmetric Anisotropic Exchange

The Dzyaloshinsky-Moriya interaction [30, 31] describes the interaction of an excited state on one magnetic ion with the ground state of another, due to spin-orbit coupling. This results in an anisotropic exchange between the magnetic ions of the form:

$$\mathscr{H}_{DM} = \mathbf{J}_{ij} \cdot (\mathbf{S}_i \times \mathbf{S}_j) \tag{2.46}$$

It does not exist if there is an inversion symmetry of the crystal field with respect to the center between the magnetic ions.

When dealing with low-dimensional systems as discussed in Part II, anisotropic exchange interactions can be relevant and has to be kept in mind. However in the investigated systems in this work effects due to anisotropic exchange have not been observed.

2.6.6 Hyperfine Interaction

Besides the electron-electron interactions at an atom there can also be interactions with its nucleus. The nuclei can carry a magnetic moment with the nuclei spin operator **I**. The magnetic field produced by the electrons interacts with the nuclear magnetic moment and vice versa. The relevant interactions causing hyperfine splitting are magnetic dipolar interaction and the much stronger Fermi contact interaction [11]. For the latter a finite electron probability at the nucleus is required, which is only given for s-(like-)states.

The Hamiltonian describing the hyperfine interaction can be written as

$$\mathscr{H}_{HF} = \mathbf{J} \cdot \tilde{A} \cdot \mathbf{I} \tag{2.47}$$

where $\tilde{A}$ depends on the type of interaction.

Since the energy scale of the hyperfine interaction is much smaller than the Zeeman interaction, it is visible in an ESR experiment as a (symmetric) splitting of a central line. Depending on the nuclear spin several lines can be observed. For the analysis of donor states in Si the hyperfine interaction was, and still is, very important. Isolated donors in Si show a pronounced hyperfine split doublet. With this the donor ground states could be identified as symmetric singlet states with a finite probability at the donor nucleus (see Section 12.1). The splitting is characteristic for the type of donor.

CHAPTER 3

Experimental

In this chapter the setups used for the ESR experiments at different frequencies and magnetic fields are described. The implementation of an electrical detected magnetic resonance (EDMR) setup at 10 GHz is highlighted. Furthermore instrumental development of microwave resonant cavities at different frequencies in the V- and W-band is discussed and their experimental characterization is presented.

3.1 Setup for Experiments at 10 GHz

The microwave frequency range from 8 - 12 GHz is referred to as "X-band". This is the most commonly used band for ESR experiments. For the experiments performed at X-band frequencies, a commercial EMX spectrometer from Bruker Biospin is available. The watercooled magnet allows sweeps of the external magnetic field of up to 1 T. The spectrometer operates at a fixed frequency around 9.6 GHz. The samples are positioned at the maximum of the magnetic field component of the microwave standing wave (Fig. 3.1) within the resonant cavity. For the ESR experiments performed for this work, two different rectangular resonant cavities were mounted in the center of the external magnetic field. The first resonator operates in the TE_{102} configuration (cf. Fig. 3.8) and was used mainly for measurements at room temperature. The second cavity has an optical transmission pathway, which allows to illuminate samples during an ESR experiment. Because of

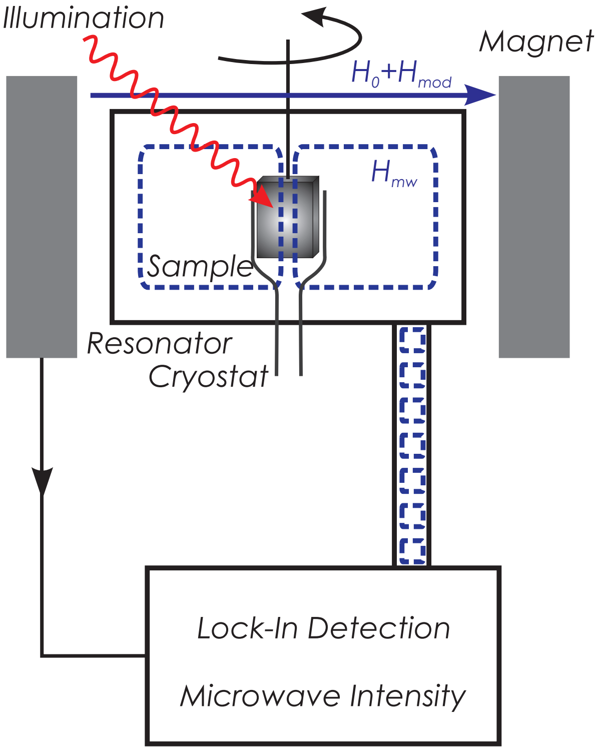

Figure 3.1: Schematic of the ESR setup at X-band frequencies; A sample is placed in a cryostat inside a rectangular resonator. Changes in the microwave intensity are detected as a function of external magnetic field H_0. Lock-in detection with a modulating magnetic field H_{mod} is used. Illumination of samples is possible in the visible and infra-red frequency range.

the optical path, the coupling of the waveguides to the resonator is realized from the top, which makes a TE_{103} mode configuration necessary. However only a single maximum of the microwave magnetic field is in contact with the sample equivalent to the TE_{102} configuration. When unloaded, the quality factor for both resonators reaches up to 5000. Samples are glued to quartz substrates or are sealed into ESR quartz tubes. Temperature dependent measurements were realized with a continuous-flow liquid helium cryostat from Oxford Instruments which enables measurements from room temperature down to about 3.7 K. Since the cryostat is inserted in the resonator the quality factor is already reduced. Typically, quality factors of the loaded resonator (cryostat and sample) of 3500 could be reached. A goniometer allows to turn the sample with respect to the external magnetic field even at cryogenic temperatures. In order to ensure high precision measurements the spectrometer can be equipped with an additional NMR sensor with accuracy of 10^{-3} Oe and an external frequency counter. In addition to the applied external magnetic field, a small AC modulation field is applied and with that a lock-in detection of the microwave intensity is realized. This results in a higher signal/noise ratio and higher sensitivity compared to a detection scheme without modulation. Typically, modulation amplitudes from 8 Oe down to 0.01 Oe and modulation frequencies from 100 kHz to 10 kHz are used, depending on the spectral features of the investigated samples.

Illumination of samples can be realized with individual laser diodes at different wavelengths, a halogen white light lamp and a tunable light source from Newport, the last of which allows continuous tuning of the wavelength from 800 to 2400 nm.

3.2 Implementation of an Electrical Detected Magnetic Resonance Setup

The original X-band spectrometer setup probes the change in microwave radiation as a function of magnetic field. When the ESR resonance condition is fulfilled, absorption is visible as a change of the microwave power which is converted to a DC voltage. The sensitivity in a conventional ESR Experiment is limited to quiet large numbers of spins $n \gtrsim 10^{10}/G$. There exists an alternative detection scheme which makes it possible to detect spin dependent phenomena on less than 100 spins [32]. This technique measures changes in the electrical resistance of the sample under microwave irradiation and magnetic field. This technique is referred to as electrical detected magnetic resonance (EDMR). EDMR was implemented in this work at the existing X-band spectrometer.

For the electrical detection scheme, it is necessary to define the active area on the sample by electrical contacts. Since the microwave standing waves in resonators are drastically disturbed by conducting substances, the amount of metallic parts (wires, contacts) is kept as small as possible. Samples are glued on quartz substrates and bonded to metal lines sputtered onto the substrates. These electrical lines consist of about 50 nm of either gold or

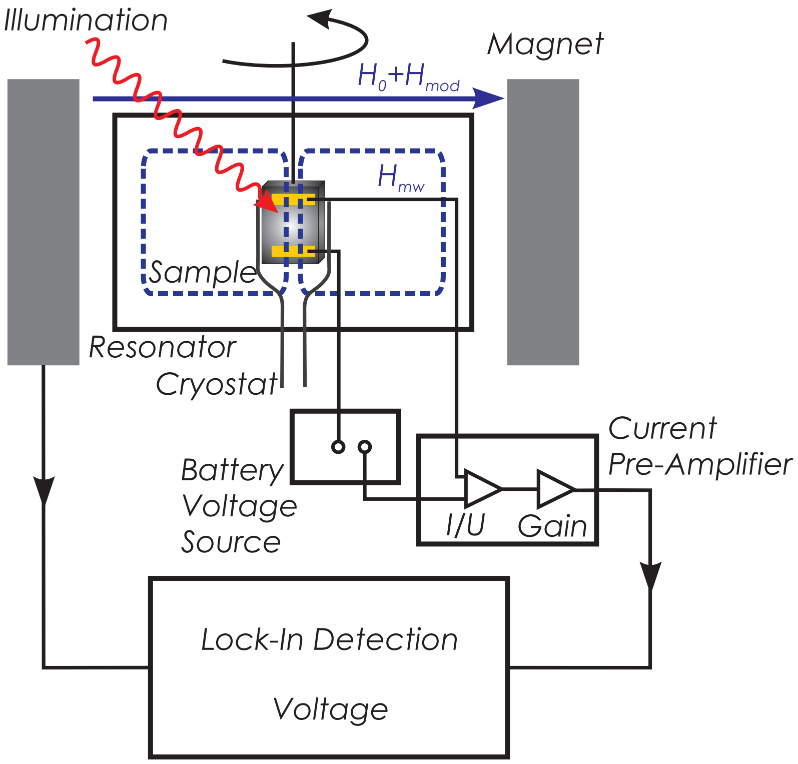
Illumination
Magnet
H_0+H_{mod}
H_{mw}
Sample
Resonator
Cryostat
Battery
Voltage
Source
Current
Pre-Amplifier
I/U
Gain
Lock-In Detection
Voltage

Figure 3.2: Schematic of the EDMR setup at X-band frequencies. A sample, with electrical contacts, is placed in a cryostat inside a rectangular resonator. A bias is applied to the sample with a battery voltage source. The current is measured and converted to a voltage using a preamplifier. The voltage change is measured as a function of external magnetic field H_0 using lock-in detection with a modulating magnetic field H_{mod}. Illumination of samples is possible in the visible and infrared frequency range.

aluminium on top of a 10 nm chrome adhesion layer. Since the skin depth at a frequency of 10 GHz is above 500 nm, the microwaves can penetrate through the metal lines and the standing wave pattern is not disturbed. With a length of 5 cm, the quartz substrates extend outside of the resonator. Here copper wires are glued with silver paste to the metal lines and the wires are guided inside a metallic sample holder to a four-pin connector.

A battery voltage source SIM928 from Stanford Research allows to apply DC voltages from 1 mV to 20 V to the sample. The current is detected via a DLPCA-200 current preamplifier from Femto and its output voltage signal is fed to the lock-in amplifier of the spectrometer (Fig. 3.2). Alternatively to the current measurement configuration the voltage between two contacts can be measured. For this a low-noise voltage preamplifier SR560 from Stanford Research is available.

3.2.1 Basic Characterization

Defects in Si-based systems have been investigated intensively with ESR [33, 34, 35] and EDMR [35, 36]. The multitude of different ESR active centers is well documented (for an overview see [37, 38]). Although almost all centers are distinguishable in terms of g-factor anisotropy and linewidth, their characteristics can be quiet similar and most signals are found around a g-factor of $g = 2$. Without discussing the physics of the defects present, a standard Si diode (1N4007 from VISHAY) was chosen to quantify the sensitivity of the EDMR setup. The plastic housing was removed in parts from the diode and the diode was glued to the quartz sample holder. Silver paste was used to ensure good electrical contact between the sputtered metal lines of the sample holder and the diode structure. By illuminating with the white light source and applying a bias in forward or reverse bias direction, the change in the current as a function of applied magnetic field was measured. Fig. 3.3 (a) shows the as measured EDMR signal dI/dH around $g = 2$ with a maximum microwave power of $P_{\mathrm{mw}} = 200\,\mathrm{mW}$ and reverse bias $U = -5\,\mathrm{V}$. The signal/noise ratio in this measurement is about 10:1. With micro structured samples, which are described in [39], better signal/noise ratios were achieved. By calibrating the internal lock-in of the EMX with an applied bias, the absolute current change could be determined. The integrated signal is plotted in Fig. 3.3 (b). The change in the current over the whole signal is on the order of pA, corresponding to a relative change on the order of $\Delta I/I_0 = 10^{-5}$. From the non-resonant background it can be seen that relative current changes of $\Delta I/I_0 = 10^{-6}$ can be detected with this EDMR setup. This is comparable to measurements reported in literature [40, 41].

3.3 High Frequency Setup

In addition to the X-band spectrometer, a high-field/ high frequency setup is available at the ESR lab at the IFW Dresden. A millimeter wave vector network analyzer (MVNA) is combined with cryogenic magnets, for which static magnetic fields up to 17 T can be reached. The microwaves are guided

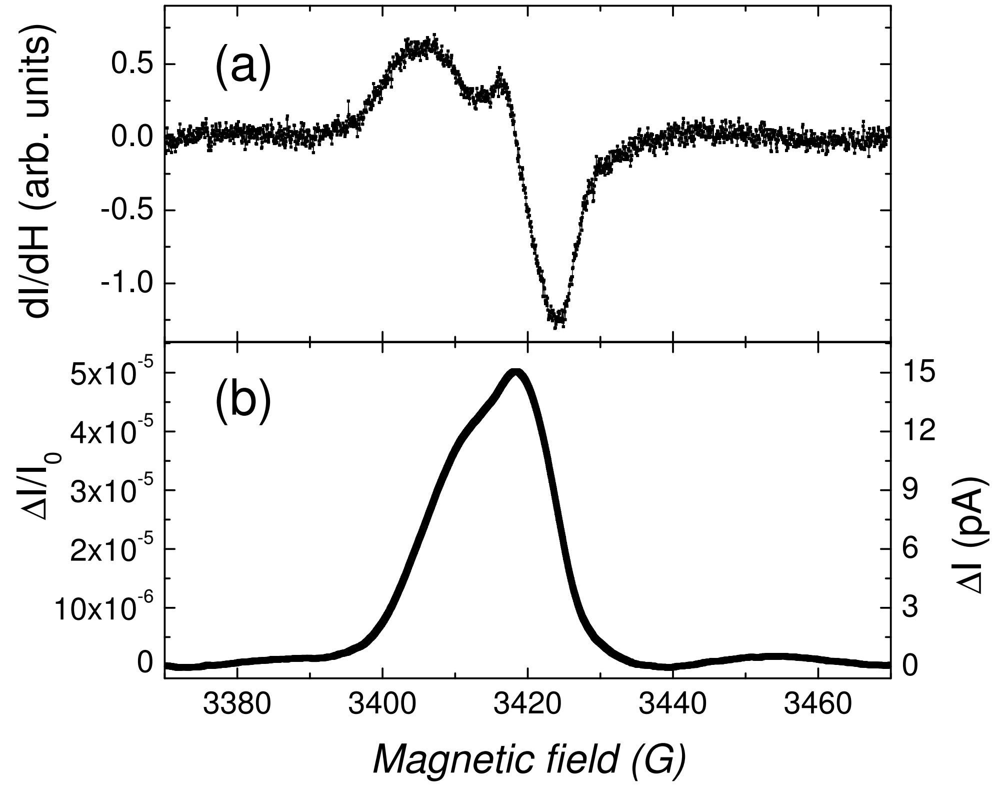

Figure 3.3: EDMR measurement on Si diode 1N4007. (a) current change dI/dH measured as a function of magnetic field at T = 20 K with U = −5 V, $f \approx 9.56$ GHz and P_{mw} = 200 mW. Ten scans were averaged. (b) Integration of dI/dH gives the relative current change $\Delta I/I_0$. From the noise floor it can be seen that current changes below pA and relative current changes on the order of 10^{-6} can be detected.

through specially constructed waveguides to the sample placed in magnetocryostats. With this home made spectrometer the energy scale, i.e. frequency and magnetic field, is widened significantly and allows versatile possibilities to investigate different spin systems of interest.

The components of the high frequency setup and their principles of operation are described in the following sections. A very good in-depth description of the original setup can be found in [22]. The focus in this section will be on the implementation of the resonant cavities to the existing setup.

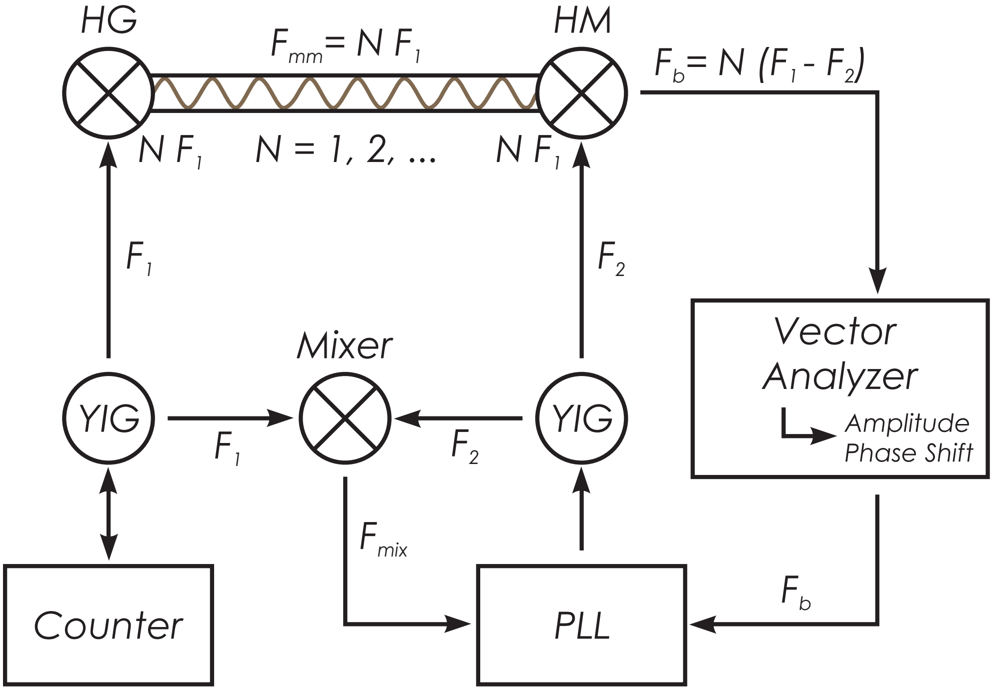

Figure 3.4: Working principle of the Microwave Vector Network Analyzer for frequencies up to 100 GHz. The two base frequencies are multiplied and phase and amplitude changes in the beating signal are detected. For details see text.

3.3.1 Millimeter Wave Vector Network Analyzer

The Millimeter Wave Vector Network Analyzer (MVNA) by AB Millimètre deployed in the experiments allows frequency tuning between 8 GHz and about 800 GHz. This large frequency range is achieved by using different non-linear solid state devices to generate and detect microwave radiation as well as to amplify and filter harmonics of the adjustable fundamental frequency. The fundamental frequency is tunable between 8 - 18 GHz and is created by yttrium iron garnet (YIG) oscillators. Two YIGs create slightly de-tuned base frequencies F_1 and F_2, which are phase-locked with one another over a Schottky diode mixer and a phase-lock loop (PLL). In the frequency regime up to about 100 GHz the working frequency is achieved with two Schottky diodes: The harmonic generator (*HG*) acts as the microwave source and the harmonic mixer (*HM*) as the detector in the experiment. They create multiple harmonics $N \cdot F_{1/2}$ of the base frequencies F_1 and F_2 respectively. Because of the de-tuned base frequency, a beat frequency is established which is characteristic for the multiplication factor N and with that the working frequency. The beat frequency $F_\mathrm{b} = N \cdot F_1 - N \cdot F_2$ is in the MHz range and is fed back to the spectrometer. With F_b and the mixed frequency F_{mix} the YIG frequency F_2 is stabilized with respect to F_1 over the PLL. A schematic of this setup is shown in Fig. 3.4.

The decrease in power with higher harmonics makes it necessary to modify the system by using different components at high frequencies. From frequencies of about 70 GHz upwards, it is possible to exchange the HG by a Gunn oscillator. In contrast to the passive YIG-driven Schottky diode the Gunn diode is powered independently from the YIG and its frequency is tuned independently as well. However, the stabilized YIG frequency is still needed for the phase lock loop (cf. [22]). Up to frequencies of about 240 GHz it is possible to use one Gunn diode and one Schottky diode. For higher frequencies the second Schottky diode is replaced by another Gunn diode. Using different multiplicators and filters, frequency ranges up to about 800 GHz are accessible with this configuration.

3.3.2 Waveguides and Cryostats

In the original setup, microwaves are guided from the Schottky or Gunn diodes by cylindrical tubes to the sample space. These oversized waveguides transmit microwaves in a broad range of frequencies. This is advantageous since one sample probe can be used with the different configurations of the MVNA, allowing for experiments over a broad frequency range. In general two configurations of sample probes are available. In the transmission probehead microwaves from the source penetrate the sample and only transmitted microwaves are detected. This probehead consists of two vertical oversized waveguides which are connected by two 45° mirrors. The sample is placed just on top of one mirror on the side of the source. On top a tapered metal part is used to focus the microwave radiation on the sample. The reflection probehead only consists of a single tube where source and detector arm are connected to the waveguide outside the cryostat separated by a polarizer. Microwaves penetrating the sample are reflected within the skin depth from the sample or by a metallic mirror placed underneath the sample.

For frequencies above 250 GHz, additionally a quasi-optical setup can be used. Here, the microwave radiation is guided by parabolic mirrors and directed to a corrugated waveguide as sample probe. This highly sensitive setup is described in detail in [42].

The sample probes can be placed in different magnetocryostats. Most experiments were performed with a magnetocryostat from Oxford Instruments allowing field sweeps of up to 17 T. A variable temperature insert (VTI) enables measurements in the temperature range from 2.5 K to above 300 K. The size of the cryostat makes it necessary for the length of the probe stick to be about 2 m. This means that the microwaves propagate along the metallic tubes for about 4 m. The attenuation for an electromagnetic wave propagating along an oversized waveguide is typically about 1 dB/m as determined in a simple transmission measurement at about 90 GHz.

Additionally, a cryogen-free magnet from Cryogenic Ltd. is available. The magnetocryostat is equipped with two coils: A main coil with a maximum magnetic field of 15 T and a sweep coil for narrow sweeps of the magnetic field in the range of 20 mT. This combination of coils and their very good magnetic field homogeneity allows to resolve very narrow lines in an ESR experiment even at high magnetic fields. Because of the smaller height of the magnet, probe sticks of about 1.2 m length can be used. The total microwave path is then about 2.5 m. This cryostat can be used with the quasi optical setup, but also a sample stick using only rectangular waveguides was constructed.

3.4 Development of the Resonant Cavity Setup

An ESR experiment can be performed simply by inserting a sample in the microwave path and measuring the interaction of the sample in terms of absorbed or reflected microwave radiation as a function of the applied external magnetic field. However, the sensitivity will be greatly enhanced when the experiment is performed using a microwave resonant cavity or, in short, a resonator.

A resonator can be thought of as an oscillating circuit with a characteristic inductance L, conductance C and resistivity R. Such a system has a characteristic resonance frequency

$$\omega_0 = 2\pi f_0 = \frac{1}{\sqrt{LC}} \tag{3.1}$$

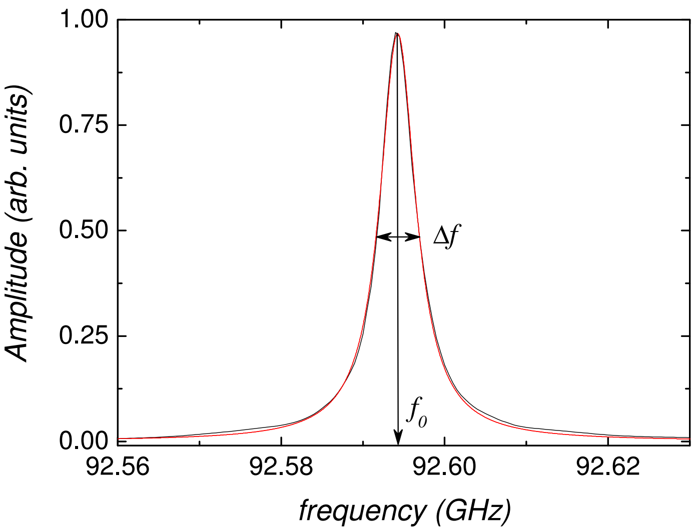

Figure 3.6: Microwave amplitude as a function of frequency around the resonance frequency f_0 of a cylindrical resonator at W-band and Lorentzian fit. The FWHM Δf and the resonance frequency can be determined experimentally. Based on that the Q factor can be calculated with equation (3.4)

If the resonator is excited by an oscillating electromagnetic field or an AC bias with a frequency ω close to the resonance frequency ω_0 energy is absorbed. When the excitation is turned off, the energy stored in the resonator decays exponentially over time due to ohmic and radiation losses. A measure for how well the resonator stores energy is the quality factor Q. The quality factor is defined as [10]

$$Q = 2\pi \frac{\text{Energy stored}}{\text{energy dissipated per cycle}} \tag{3.2}$$

For an RLC circuit Q is given by

$$Q = \frac{\omega_0 L}{R} = \frac{1}{\omega_0 C} \tag{3.3}$$

which leads to [10]

$$Q = \frac{\omega_0}{\Delta\omega} = \frac{f_0}{\Delta f} \tag{3.4}$$

where Δf is the full width at half maximum (FWHM) of the Lorentzian absorption peak of the resonance. This relation is experimentally accessible and can be used to characterize constructed resonators (cf. Fig. 3.6). At microwave frequencies standard electronic components cannot be used to build a resonator. However there are many different types of resonators which can be used for experiments at wavelengths in the microwave range.

Their characteristics, as Q-factors and possible frequency range, can differ significantly and it is necessary to find a suitable design for any desired application.

In the lower GHz regime stripline resonators [43] or microstrip resonators [44] are commonly used. The quality factors are fairly low, but can be compensated by large filling factors when enough sample material is available. More recently planar microcoil resonators working up to several GHz were developed [45, 46]. The metallic lines are fabricated with lithography techniques on different substrate materials. This kind of resonators are suitable for μm-sized, but highly spin concentrated sample materials. Because of the relatively low Q-factors pulsed experiments are possible with those structures.

Mainly at frequencies above 100 GHz Fabry-Perot resonators are used [47]. By adjusting a reflective mesh the resonance frequency can be tuned and frequency shifts due to temperature dependent measurements can be compensated.

In the intermediate regime (whispering gallery) dielectric resonators [48, 49] as well as metallic resonators are most commonly used. Metallic resonant cavities were chosen as the resonator design. The reasons for our choice of resonators are their fairly easy implementation into the existing high field setup and their convenient dimensions as suited for the samples to be investigated.

In metallic resonators electromagnetic standing wave patterns are formed, dependent on the geometry and dimensions of the resonant cavity. The main reasons for energy losses in metallic resonators are ohmic losses in the cavity walls, radiation leakage through coupling holes, losses due to an eventual dielectric medium in the resonator as well as dielectric losses due to sample and sample holder. The experimental reciprocal Q-factor is therefore given by the sum of the individual losses:

$$\frac{1}{Q} = \frac{1}{Q_{\text{walls}}} + \frac{1}{Q_{\text{holes}}} + \frac{1}{Q_{\text{dielectric}}} \tag{3.5}$$

Cylindrical resonators can reach very high quality factors of up to 10000 [50]. The reason is that, due to their larger volume to surface ratio, cylindrical resonators can store more energy and therefore exhibit larger quality factors than rectangular ones [10]. Because of this the instrumentation of choice for the desired experiments are cylindrical resonators.

3.4.1 Mode Propagation

Let us consider the propagation and distribution of electromagnetic waves in order to understand how the microwave components can be combined and optimized for the experimental setup: An electromagnetic wave propagating along z-direction can be described by its vectors of the electric $\mathbf{E}(z)$ and the magnetic field component $\mathbf{B}(z)$ as a plane wave

$$\mathbf{E}(z) = \mathbf{E}_0 \exp i(kz - \omega t) \qquad \mathbf{B}(z) = \mathbf{B}_0 \exp i(kz - \omega t) \tag{3.6}$$

where the z-component for $\mathbf{E}_0$ and $\mathbf{B}_0$ is zero and $\mathbf{E}(z)$ and $\mathbf{B}(z)$ are perpendicular to each other. k is the wave vector along z and ω is the angular frequency.

When transmitted quasi-optically through air or in oversized waveguides the plane wave equations satisfy the Maxwell equations in vacuum. In contrast to oversized waveguides in which the millimeter waves can propagate quasi optically, metallic tubes can be chosen as waveguides with dimensions on the order of the wavelength. Then an electromagnetic wave propagates, restricted by the boundary conditions for electric and magnetic fields at the (perfectly) conducting metallic surface:

$$E_{\parallel} = 0 \tag{3.7}$$

$$B_{\perp} = 0 \tag{3.8}$$

In coaxial cables the waves are usually transverse electromagnetic (TEM) waves, for which $B_z = E_z = 0$ [10]. Coaxial cables are commonly used in the MHz and lower GHz regime, but special coaxial-like cables can be used for frequencies up to about 80 GHz. This becomes important when concerned with measurements at very low temperatures (e.g. in dilution refrigerators) [51], where the microwave has to be applied locally to a sample structure and where the thermal heat transferred has to be minimized. For this, pure metallic waveguides are a poor choice. However the power losses are usually slightly higher in such cables [1]. For the regular ESR measurements high microwave powers can be necessary and usually macroscopic samples are investigated. Therefore our setup built for temperatures down to about 2.5 K comprises of oversized and connected rectangular waveguides as described in Section 3.4.4. In rectangular (and cylindrical) waveguides TEM waves cannot be transmitted [10]. Instead there are transverse electric (TE) waves with $E_z = 0$ and $B_z \neq 0$ and transverse magnetic (TM) waves with $B_z = 0$ and $E_z \neq 0$.

---

[1] A typical micro-coax cable UT-085 exhibits losses of about 0.6 dB/m at 1 GHz (e.g. Micro-Coax - www.micro-coax.com). The losses increase with increasing frequency.

Let us consider a rectangular waveguide with dimensions a and b along the x and y directions respectively. The electromagnetic wave is propagating along z. Because of the boundary conditions standing waves are formed with the allowed wave vectors being quantized in the transverse directions x and y. The allowed wave vectors **k** are given in integers of the half-wavelength in the appropriate direction:

$$\mathbf{k} = (k_x, k_y, k_z) = \left(\frac{m\pi}{a}, \frac{n\pi}{b}, k_z\right) \tag{3.9}$$

The dominant mode in the rectangular waveguide is the fundamental TE_{10} mode where the subscripts refer to the number of half-wavelengths $m = 1$ and $n = 0$.

Electromagnetic waves can be transmitted as single modes only in a limited frequency range which depends on the dimensions of the waveguide. For a waveguide, where the dimensions are very large compared to the wavelength, different modes are very close in frequency and no defined single standing wave is possible. When the dimensions of the waveguide become too small the boundary conditions cannot be fulfilled anymore. This places an upper limit on the frequency (lower limit on the wavelength) for any given mode. The cutoff-frequency for free propagation is defined as:

$$f_c = \frac{1}{2\pi}\sqrt{\left(\frac{m\pi}{a}\right)^2 + \left(\frac{n\pi}{b}\right)^2} \tag{3.10}$$

The microwave power for the radiation is attenuated due to ohmic losses in the conducting waveguide walls. When the frequency of the propagating wave is larger than the cutoff-frequency, those losses are significantly enhanced.

Losses of about 3.3dB/m at a frequency of 20 GHz are to be expected. An (ideal) metallic rectangular waveguide experiences losses of only about 1.5 dB/m at 50 GHz and 3 dB/m at 90 GHz. [52]

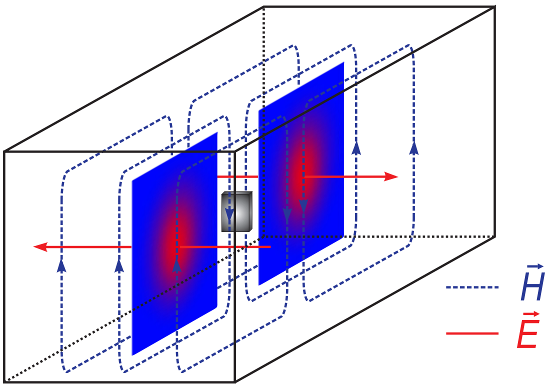

Figure 3.8: Schematic drawing of the TE_{102} mode pattern in a rectangular resonant cavity. Microwave magnetic field lines (dashed blue lines) and electric field lines (red lines) are indicated. The contour plot indicates the field distribution. Samples are placed at the maximum of the magnetic field component.

In order to minimize losses but still be able to keep the experimental effort to a minimum, only two different waveguides were chosen which allow for measurements within certain frequency bands. Inner waveguide dimensions for different frequency bands are standardized and waveguides from different materials are commercially available. Characteristics of the waveguides used are listed in Table 3.1.

Band	width [mm]	height [mm]	freq. range [GHz]	cutoff-freq. [GHz]
V	3.76	1.88	50 - 75	40
W	2.54	1.27	75 - 110	59

Table 3.1: Frequency bands and waveguide characteristics.

3.4.2 Resonant Cavity Modes

We can think of a resonator as a terminated waveguide, e.g. a cut waveguide where metallic plates are placed on its end. Therefore the electromagnetic standing waves - in rectangular waveguides confined in the transverse direction only - become confined in the z-direction (the propagation direction in a waveguide) as well. The modes in resonators are then labeled with subscripts m, n, p, which again refer to the number of half-wavelength. For the rectangular resonator of length d the wave vector is then:

$$\mathbf{k} = (k_x, k_y, k_z) = \left(\frac{m\pi}{a}, \frac{n\pi}{b}, \frac{p\pi}{d}\right) \tag{3.11}$$

The resonance frequency of a resonator depends on the actual mode present and the dimension of the resonator. It can be calculated as

$$f_0 = \frac{1}{2}\sqrt{\frac{(m/a)^2 + (n/b)^2 + (p/d)^2}{\mu\epsilon}} \tag{3.12}$$

where μ is the permittivity and ϵ the dielectric constant of the medium inside the resonator.

The commercial setup used for ESR experiments at 10 GHz works in the mode configuration TE_{102} or TE_{103}. The TE_{102} mode is visualized in Fig. 3.8.

In order to calculate the electromagnetic waves in a cylindrical resonator, an appropriate coordinate system has to be chosen. Thus, for a cylindrical resonator, the mode profiles are calculated using the Laplace equation in cylindrical coordinates [53, 10]. The solution of this are modes characterized as TE_{mnp} and TM_{mnp} modes, where the subscripts m, n, p refer to the half wavelengths along the angular ϕ, radial r and longitudinal direction z of the resonator.

The resonance frequency can be calculated for a certain TE mode with

$$f_0 = \sqrt{\left(\frac{c(k_c a)'_{mn}}{\pi}\right)^2 + \left(\frac{cp}{2}\right)^2\left(\frac{2a}{d}\right)^2} / (2a) \tag{3.13}$$

where a is the radius, d the length of the resonator, c the speed of light in vacuum and $(k_c a)'_{mn}$ the nth root of the mth order Bessel function $J'_m(k_c a)$ [10]. From equation 3.13 the resonance frequencies of a certain mode can be easily calculated for different resonators. The actual cavities designed, their dimensions, resonance frequencies and quality factors are listed in Table 3.2 in Section 3.4.5.

3.4.3 Resonant Cavity Design

As in every waveguide, there are losses of microwave energy due to the dissipation in the waveguide walls. They increase with increasing frequency and are several db/m for a typical rectangular waveguide [52]. Especially when measuring at a frequency where only small power is available, the losses due to the fixed length of the waveguide of about 4 m can become a critical issue for the experiment. The dimensions of the resonant cavities were

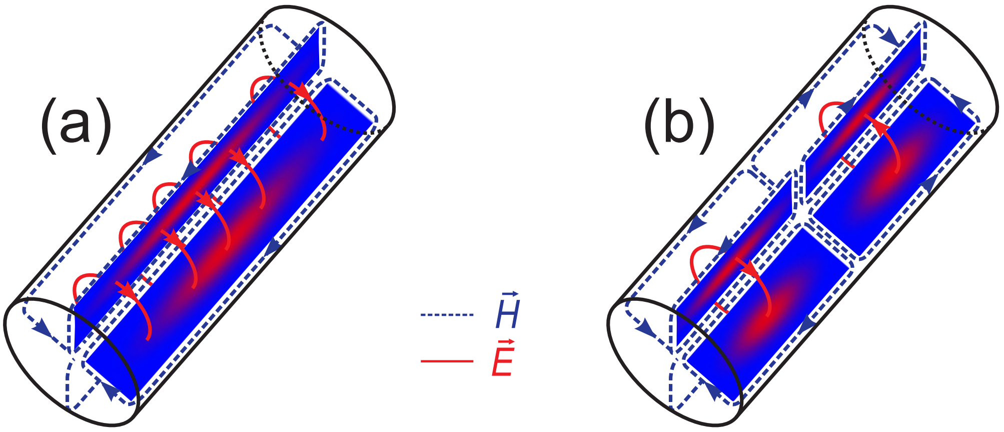

Figure 3.9: Schematic of the (a) TE_{011} and (b) TE_{012} mode pattern in a cylindrical resonant cavity. Microwave magnetic field lines (dashed blue lines) and electric field lines (red lines) are indicated. The contour plots indicate the field distribution.

therefore chosen in a way that the resulting resonance frequencies are close to the maximum output powers of the high frequency setup.

The chosen design is that of a cylindrical resonant cavity, which exhibits quality factors around 10000 [50], larger than those of rectangular resonant cavities. To achieve high microwave intensity at the sample, the fundamental mode TE_{011} and, as an additional option, the TE_{012} is desired. Two different cavity configurations were constructed in this work: The axial resonant cavity [Fig. 3.12(a)], in which the sample is placed at the end plate and the transverse resonant cavity [Figure 3.12(b)], in which the sample can be mounted on a sample holder centered in the resonator. Depending on the sample geometry it is advantageous to use one or the other resonator, since the sample has to be small compared to the nodes of the microwave radiation. In an ESR experiment the microwave magnetic field has to be perpendicular to the applied external field. Since the applied field axis is fixed by the superconducting magnet system and the coupling configuration on the resonator is fixed as well, indeed two different resonant cavities are necessary.

A transmission setup was chosen, in which two rectangular waveguides couple each to a separate coupling hole in the cavity. If one wants to excite not only the TE_{011} but also the TE_{012} mode the waveguides have to be placed centered at 1/4 and 3/4 the length of the resonator for the transverse one and at ±1/2 the radius for the axial one.

Since for TE modes there are no currents flowing between the end plates and the cylindrical body [50], the quality factor is not decreased when assembling a cavity from different parts, which allows for easier experimental handling.

At the axial resonator the coupling is realized through one of the end plates instead of the cylindrical body. It consists of three parts [Fig. 3.12(a)]. At the center of the bottom part a sample can be placed. The cylindrical center part is placed on top. On top of this the coupling plate with pockets for the waveguides is positioned. Two screws connect the three parts. For all resonators the waveguides are first joined with a clamp and then screwed tightly to the resonators.

The transverse resonator [Fig. 3.12 (b)] consists of a cylindrical center part, where two coupling holes were drilled at 1/4 and 3/4 of its length. The cylindrical transverse resonator is closed off with two circular plates on its ends which can be screwed to the center part individually. Through a hole at the center of both coupling plates a small sample holder can be accurately positioned and a sample can be mounted in the center of the resonator.

The coupling between waveguide and resonator was optimized. For large coupling holes the leakage of microwave radiation from the cavity is large and the microwave standing wave decays quickly. If the holes are small most of the microwaves are reflected back into the waveguide, but not fed through to the resonator. For coupling hole diameters of around 0.5 mm, good Q values were found for the cavities. Another factor is the coupling plate or the wall thickness between resonator and waveguide. This has to be as thin as possible since the microwave is attenuated when passing through the coupling plate. On the other hand the mechanical stability is crucial since the waveguide is pressed against the thin plate. For the constructed cavities, wall thicknesses around 0.2 mm were found to be a good compromise. In order to have a continuation of the microwave magnetic field direction in waveguide and resonant cavity, the waveguides have to be placed with their shorter walls facing each other (Fig. 3.10). This denotes a min-

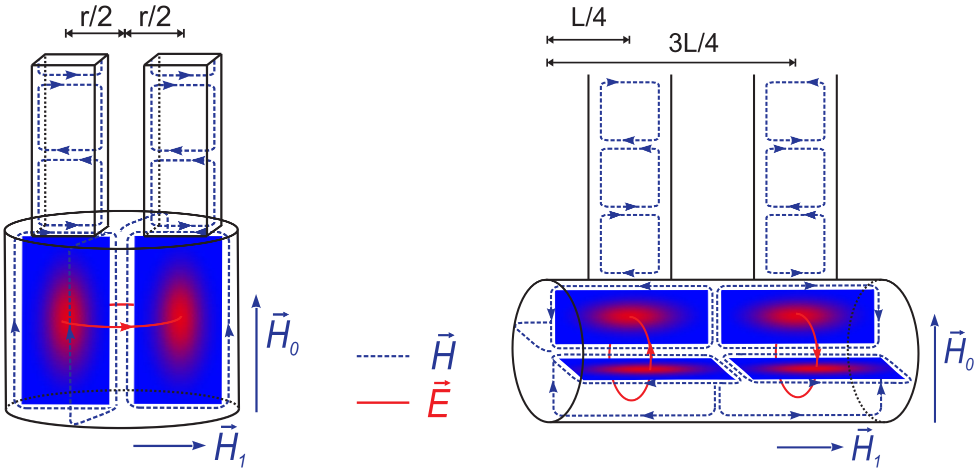

Figure 3.10: Schematic of coupling between rectangular waveguide and (a) axial resonant cavity and (b) transverse resonant cavity in the TE_{011} configuration. The microwave magnetic field $\vec{H}_1$ has to be perpendicular to the external magnetic field $\vec{H}_0$ for an ESR experiment. Waveguides are centered at half the radius for the axial resonator and at 1/4 and 3/4 the length of the transverse resonator. The microwave magnetic field lines (dashed blue lines) from the waveguide are aligned to those in the resonator. Electric field lines are indicated as red lines. The contour plots indicate the electric and magnetic field distribution.

imum size for the coupling plates of the resonant cavity of two times the longer waveguide side plus four times its wall thickness. This adds up to a minimum width or diameter of about 12 mm for V-band and about 9.5 mm for W-band resonators. Another limiting factor is the sample space in the cryostat with diameter $d = 24$ mm.

The microwave power as a function of frequency is fairly irregular, due to the characteristics of the individual devices of the MVNA. In "W-band" the maximum power can be reached with a Gunn diode at 83 GHz. Around a frequency of 93 GHz an additional preamplifier with an adjustable attenuator can be employed, which allows for high power measurements and power dependent measurements at this selected frequency using either Schottky or Gunn diodes. Resonant cavities were designed in such a way that, within the dimensional constrains discussed above, their resonance frequencies are close to frequencies with maximum power within the desired band. The different resonant cavities designed and constructed are listed in Table 3.2.

3.4.4 Resonant Cavity Sample Stick

To allow the use of microwave resonant cavities a new sample stick was designed (see Fig. 3.11).

From the MVNA configuration for the desired frequency, a monochromatic millimeter wave is coupled into an oversized cylindrical waveguide in the usual way (see Section 3.3.1). The oversized waveguide is connected via a transition part to a rectangular waveguide. The transitions have a circular opening on top, which reduces conically towards a rectangular opening at the bottom with the standardized dimensions for a rectangular waveguide for the corresponding frequency band. The bottom part was soldered to the rectangular waveguide in such a way, that the rectangular opening aligns with the opening of the rectangular waveguide. The top part was inserted up to the middle of a circular cartridge and fixed by soldering. From the top the oversized waveguide was inserted into the cartridge and screwed tightly to the transition. This way, rectangular waveguides for different frequency ranges can be easily replaced and used with the same pair of oversized waveguides. The two rectangular waveguides can be fixed in position with clamps to ensure the waveguides are parallel and do not bend. The end parts are then pressed on a resonant cavity which is screwed to the clamp [Fig. 3.11(c), (e)]. For an easier and reproducible positioning of the waveguides, the resonators have rectangular pockets centered at the coupling holes. The bottom ends of the rectangular waveguides were polished and thin layers of indium were placed in the pockets. The waveguides press the soft indium layers in place, ensuring good electrical conductivity between the different components. That way, leakage of microwave radiation directly between the two waveguides - without going through the resonator - is reduced significantly. Two sample probes using rectangular waveguides for V- and W-band were constructed. All resonant cavities were plated with $200\,\mu$m gold. The skin depth in gold is below $1\,\mu$m [54]. Thus microwaves do not penetrate into the brass. Therefore eventual (para-) magnetic impurities in the brass cannot cause spurious ESR signals, which might overlap with signals originating from the sample. Additionally, the higher microwave conductivity of gold allows for higher quality factors as compared to brass. For the transverse resonators, a quartz rod of 0.5 mm diameter is axially centered between the two end plates and samples are placed in the middle of it. For the axial resonator samples are positioned at the bottom of the resonator, removing the need for an additional sample holder.

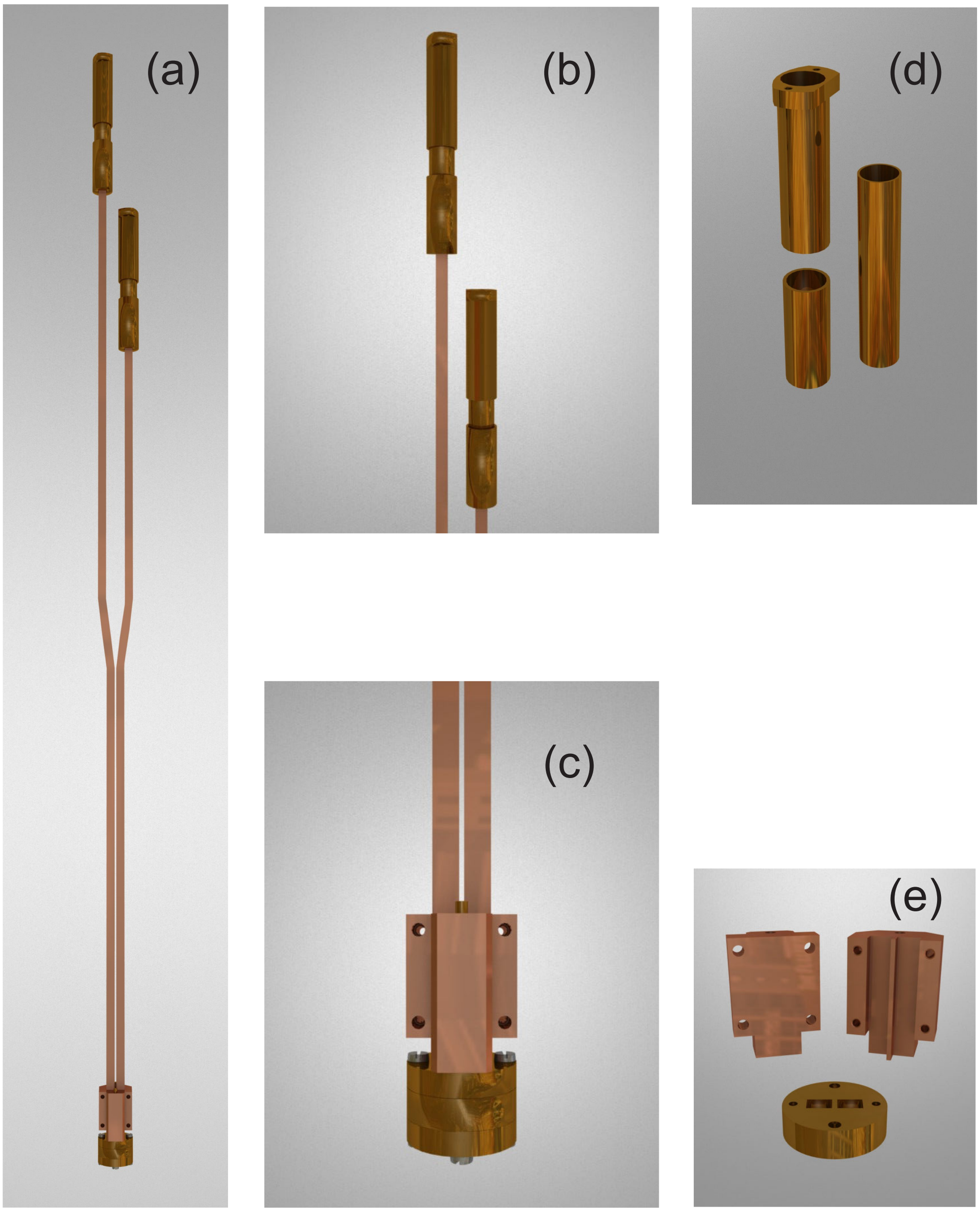

Figure 3.11: Probestick with axial resonant cavity. The probestick (a) consists of two rectangular waveguides connected to a transition part (b), (d) to which a circular oversized waveguide can be connected. At the bottom (c), (e) the rectangular waveguide are set in the pockets of the axial (or transverse - not shown) resonator and are fixed with a clamp.

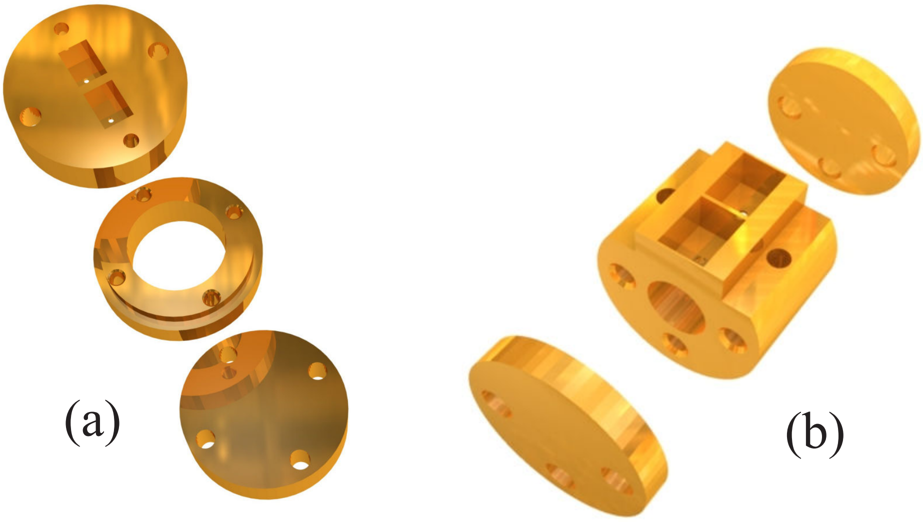

Figure 3.12: Axial (a) and transverse (b) resonant cavity. Two axial cavities (W3a, W4a) were constructed for W-band. Different resonance frequencies are achieved by exchanging the cylindrical body with one of different dimensions. In total four transverse resonators were built. Two resonators at V-band (V1t, V2t) have the same dimensions, but V2t has 0.2 mm wide cuts at 1/4 and 3/4 of the length of the cylindrical body. The transverse resonators at W-band (W1t, W2t) have different inner diameters and with that different resonance frequencies (cf. Table 3.2)

.

To ensure temperature control, a calibrated Cernox temperature sensor was glued to the resonator. A twisted Manganite wire of about 70 Ω was wrapped tightly around the clamp close to the resonator. Varnish with high thermal conductivity was used to ensure a good thermal contact between temperature sensor and resonator as well as heater and resonator.

3.4.5 Experimental Characterization

The MVNA setup allows frequency scans in a small frequency range of about 10 GHz. This constitutes a convenient way to identify and characterize the different modes of the resonant cavities by sweeping the frequency through

cavity	diameter [mm]	length [mm]	Mode	th. freq. [GHz]	exp. freq. [GHz]	Q at 300 K
V1t	7.4	13.0	TE_{011}	50.78	50.66	10000
V2t	7.4	13.0	TE_{011}	50.78	50.66	6700
			TE_{012}	54.57	54.42	6600
W1t	4.5	9.8	TE_{011}	82.75	82.17	9600
			TE_{012}	86.89	86.33	5100
W2t	4.0	9.8	TE_{011}	92.75	92.64	9200
			TE_{012}	96.47	96.13	9600
W3a	11.0	2.25	TE_{011}	74.50	74.78	4200
W4a	11.0	2.0	TE_{011}	82.05	81.78	2300

Table 3.2: Axial and transverse resonant cavities at V- and W-band: Physical dimensions, mode configuration, theoretical and experimental resonance frequencies as well as experimentally determined Q-factors of the unloaded resonators. There are two transverse resonators at V-band (V1t, V2t), which are identical in their dimensions. V2t was modified from V1t by cutting slits at 1/4 and 3/4 of its length to suppress TM modes. This significantly decreased the Q-factor. At W band there exist two transverse (W1t, W2t) and two axial (W1a, W2a) resonators.

the resonance. Exemplarily Fig. 3.13 shows the microwave intensity as a function of frequency for the unloaded resonant cavity "V2t" at 300 K. The spectrum was obtained by coupling the microwaves with short quasi optical waveguides to the lower part of the waveguide (Fig. 3.11). Three major peaks are visible in Fig. 3.13. They correspond to the TE_{011} and the TE_{012} modes. The third peak is close to the resonance frequency of the TE_{311} mode. The peaks can be fitted as Lorentzian lines. From the resonance position f_0 and the full width at half maximum (FWHM) Δf, the quality factor Q can be calculated.

$$Q = \frac{f_0}{\Delta f} \tag{3.14}$$

All the experimentally determined resonance frequencies $f_{011} = 50.66\,\mathrm{GHz}$, $f_{012} = 54.42\,\mathrm{GHz}$ and $f_{311} = 55.23\,\mathrm{GHz}$ are close to the theoretically calculated values. The quality factors for TE_{011} and TE_{012} modes of about 6700 are significantly higher than for the TE_{311} mode, for which the quality factors only borders $Q = 1000$. The coupling of the waveguide to the resonator is optimized for the TE_{012} configuration. The microwave magnetic field component is maximum at the position of the coupling holes. This is re-

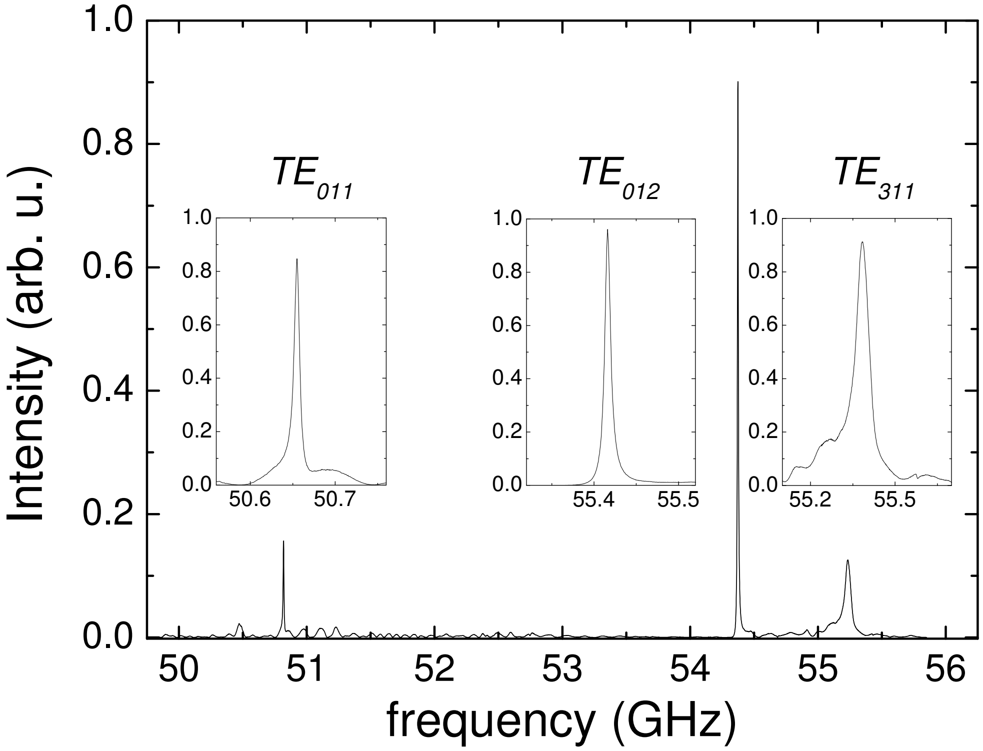

Figure 3.13: Resonance modes of a resonant cavity in the V-band frequency range. Insets show the three resonances visible. They are identified as TE_{011}, TE_{012} and TE_{311} modes respectively.

flected in the much higher intensity of the TE_{012} compared to the TE_{011}-mode. Additionally, a MVNA configuration was used which allowed a single frequency sweep through all resonances. For this configuration the microwave power is higher at the resonance frequency f_{012}.

Although the generation of the TE_{311} mode is obviously possible it is damped significantly which results in the much smaller quality factor of this mode. Also, the TE_{311} mode pattern does not pose a convenient configuration for the ESR experiment. The parameter $m = 3$ for the azimuthal angle ϕ results in a non-zero electric field at the center of the resonator where the sample is mounted. However, the presence of this mode does not limit the functionality of the resonator. The frequency of the microwave setup can be stabilized with the feedback loop to an accuracy in the kHz range. The different modes are separated on the order of GHz. Therefore it is possible to generate a single particular mode in the resonator and to perform ESR experiments with a defined mode pattern. This allows for ESR experiments at different but relatively close frequencies using a single resonant cavity. In addition to the possibility to measure closely spaced points in the plot frequency vs. magnetic field, this can be of importance to make sure an observed signal is indeed due to a resonance effect and not an "artificial" signal due to possible temperature drops or the magnetic field dependency of the temperature sensor at very low temperatures.

In order to prevent the generation of TM-modes, which are degenerate in frequency to the corresponding TE-modes, slits are cut at 1/4 and 3/4 of the length of the cylindrical body for resonator V2t. However it was found that the quality factor was decreased compared to the original design (cf. Q-factors V1t and V2t in Table 3.2). Besides the transverse V-band resonant cavities, resonators for W-band were constructed as listed in Table 3.2. The resonance frequencies for W1t and W2a are close to the frequency with maximum output power of the MVNA system when using a Gunn diode. W2t is used with an additional amplifier, with a maximum output power of the system around 93 GHz.

In general the quality factors for the transverse cavities (V1t, V2t, W1t, W2t) are comparable but higher than for the axial resonators (W1a, W2a). This is probably due to the relatively large surface area of the cylindrical body of the transverse resonators compared to those of the axial resonators and the larger volume to surface ratio.

When performing a frequency sweep, the detected microwave intensity at an individual frequency depends on the output power of the MVNA as well as propagation of the radiation through the sample stick. When microwave radiation is guided between the Schottky (or Gunn) diodes by rectangular waveguides only, the intensity oscillates as a function of frequency. For certain frequencies, standing waves form in the waveguides depending on their length. This spectrum is usually very smooth and varies on the order of about 10 dB. When the microwaves are coupled quasi-optically to the transitions or oversized waveguides, this regular pattern is disturbed. Firstly, due to the additional length of the oversized waveguides, the overall microwave power is reduced accordingly. Secondly, the polarization of the microwave radiation is not fixed as in the rectangular waveguides and therefore changes as a function of frequency. This results in drops of the intensity

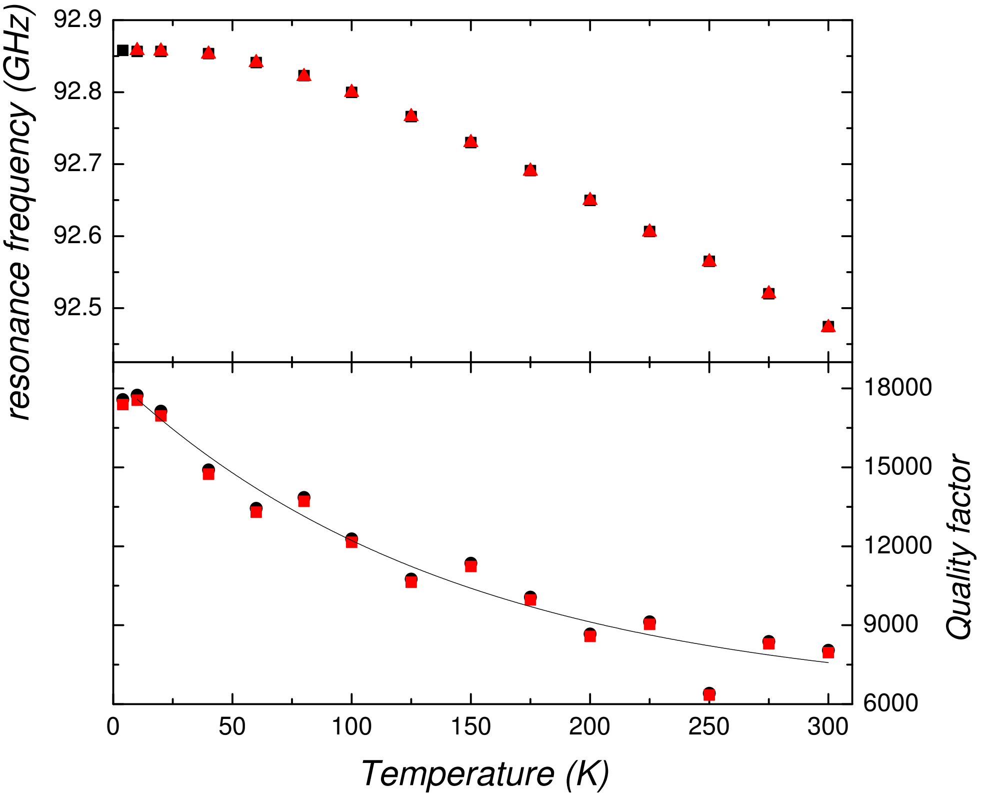

Figure 3.14: Shift of the resonance frequency and quality factor of the TE_{011} mode of a W-band resonator with sample holder as a function of temperature. A first order exponential fit to $Q(T)$ is drawn as a black line. Data for decreasing (black circles) and increasing temperature (red squares) are shown.

to nearly zero at frequencies where the polarization of the electromagnetic wave is perpendicular to the desired polarization direction at the detector. Additionally, multiple reflections are possible due the small gaps between oversized waveguides and transitions, as well as transitions to rectangular waveguides. The spectrum measured around the resonance frequency of a resonator is then also a function of the non-resonant frequency dependent background and the resonance peak of the cavity. Usually the non-resonant features are broader than the sharp resonance. However, if the resonance is close to a minimum of the background, shape and intensity of the resonance can be influenced and the Lorentzian fit to the peak is affected. In contrast to some commercial ESR setups, the resonant cavity in this setup is inserted into the cryostat and has to be cooled to the temperature, at which

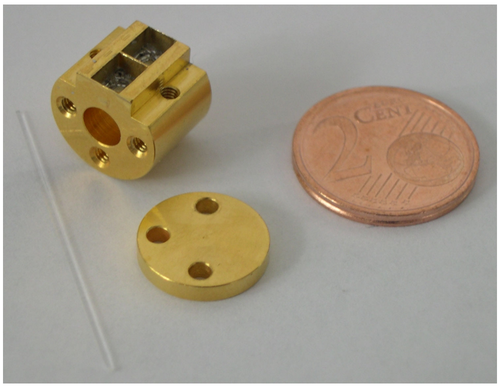

Figure 3.16: Photograph of resonator with $f_0 \approx 83\,\mathrm{GHz}$. Cylindrical body, one end plate and the sample holder used in experiments are shown.

experiments are to be carried out. This can become an issue in determining the quality factor correctly, since the resonance frequency changes as a function of temperature. With changes in temperature, the electric (microwave) conductivity of the metallic parts changes, as well as the dimensions of the resonator, due to thermal expansion. This results in a change of resonance frequency and quality factor with temperature (Fig. 3.16). The resonance frequency is constant in the low temperature regime up to about 50 K, from there it starts to decrease until the frequency shift with temperature can be approximated linearly from below 150 K to 300 K. The total frequency shift over the whole temperature range from 4 K to 300 K is small with only $\Delta f = 0.4\,\mathrm{GHz}$.

With decreasing temperature, the (microwave) conductivity increases. This is reflected in the behavior of the quality factor. It increases almost exponentially with decreasing temperature but then levels out and becomes approximately constant at low temperatures. The relative increase of the quality factor comparing 300 K to 4 K is usually about a factor of two to three.

For the transverse resonators, it is necessary to mount the sample on an axially centered sample holder in such a way that the magnetic field component of the microwave standing wave has its maximum at the sample position (Fig. 3.9). Sample and sample holder, as with all dielectric materials, locally disturb the electromagnetic mode pattern and additional leakages might be introduced at the end plates. This results in a shift of resonance frequency and a decrease in the quality factor compared to the empty resonator. Fig. 3.17 shows the change of the TE_{011} mode of a resonator at W-

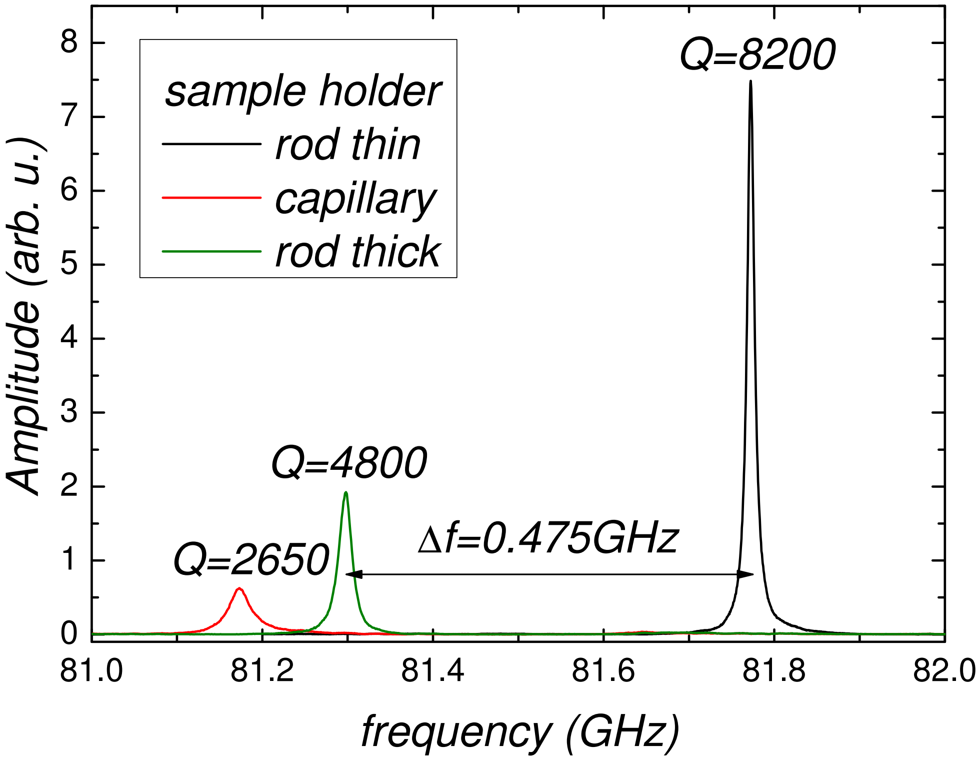

Figure 3.17: Frequency shift and change of Q-factor of the TE_{011} mode of a W-band resonator due to different sample holders

band due to different quartz sample holders of varying thickness. The thin quartz rod of diameter 0.5 mm was chosen as the sample holder in all experiments. It was accurately mounted between the center of the two end plates where the electric field component is at its minimum. For this configuration a small shift in the resonance frequency is observed and the losses in intensity are acceptably small. The sample holder is still robust enough for experimental handling.

3.4.6 Performing an ESR Experiment

In order to perform an ESR experiment using a resonant cavity, the microwave frequency has to be fixed at the resonance frequency f_0. The MVNA allows to precisely tune the frequency to the appropriate value within the accuracy of several kHz. Then the magnetic field is scanned through the ESR resonance with the fixed frequency f_0. Since the sample and eventu-

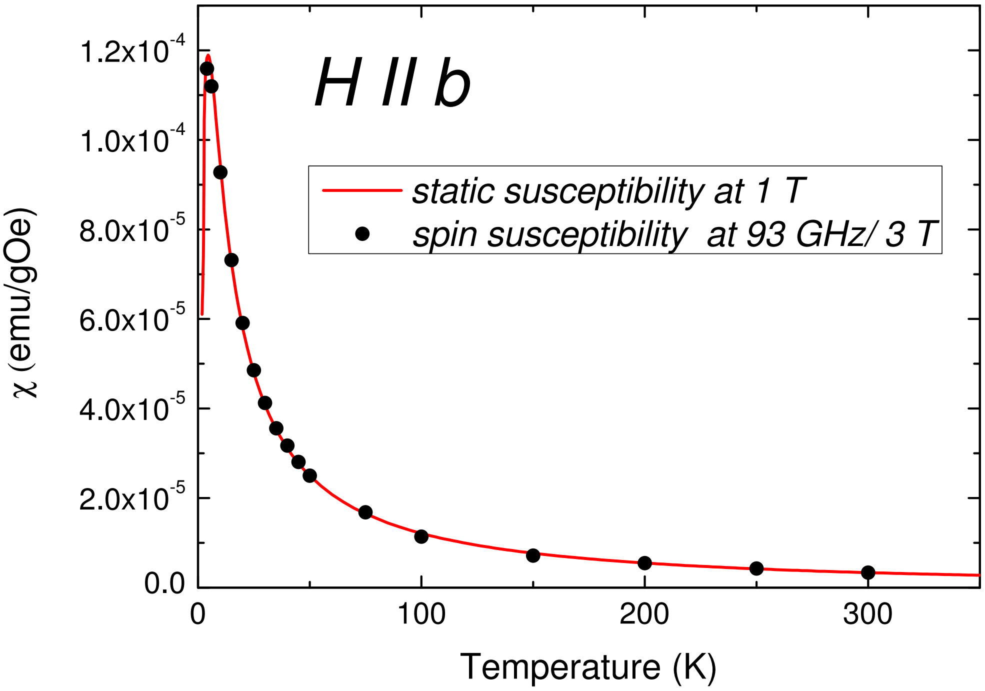

Figure 3.18: Spin susceptibility $\chi_s(T)$ corrected by the quality factor $Q(T)$ as determined by ESR and static susceptibility

ally the sample holder might change the resonance frequency slightly, the new resonance frequency has to be determined before every measurement. In contrast to the experiment at X-band frequencies, where the continuous-flow cryostat is located inside the resonator, the resonant cavities at V- and W-band are inserted into the VTI and cooled down to the sample temperature. As seen in Fig. 3.16 the resonance frequency shifts with the temperature and has to be adjusted accordingly. The quality factor is determined by a frequency sweep through the resonance at every temperature and the quality factors are calculated. Since the quality factor is also changing with temperature and can reach values of close to 20000 at temperatures of 4 K, the measured ESR intensity and, with that, the corresponding intrinsic spin susceptibility has to be corrected accordingly. As an example Fig. 3.18 shows the spin susceptibility of the low-dimensional system Linarite for $H \parallel b$ measured with a transverse resonator around 93 GHz as compared to the static susceptibility determined by SQUID measurements. The data is normalized to the 300 K value of the static susceptibility, since the absolute value of the spin susceptibility could not be determined. The as-measured values are corrected by a first order exponential fit through the temperature dependence of the quality factor of the empty cavity. This works as long as the sample is small and does not change the properties of the resonator. The data shows perfect agreement between static and intrinsic spin susceptibility. In contrast to that, a point-to-point correction did result in a larger scattering around the static susceptibility values. Due to the irregular background in frequency of the microwave power in combination with the frequency drift of the resonance, the Q-factor values could not be accurately determined at some temperatures/ frequencies. Therefore this error directly reflects on the spin susceptibility when using a point-to-point correction. Experiments on the spin-chain material Linarite are further discussed in Chapter 6.

Part II

Quasi One-Dimensional Spin-Chains

---

4 Motivation

5 Quasi One-Dimensional Systems

5.1 Magnetic Order and Excitations 63
5.2 Competing Interactions 64
5.3 Haldane Spin Chain 66

6 Linarite

6.1 Structure 70
6.2 Magnetization and ESR 71
6.3 NMR 79
6.4 Summary and Conclusion 81
6.5 Outlook 82

7 The Ni-hybrid $NiCl_3C_6H_5CH_2CH_2NH_3$

7.1 Structure 83
7.2 Susceptibility and Magnetization 85
7.3 ESR 88
7.4 Further Investigations 95
7.5 Summary and Conclusion 96

8 Summary

CHAPTER 4

Motivation

Let us follow up on the Preface, where low-dimensional systems of insulating crystals and semiconductor heterostructures where introduced. In comparison to the semiconductor systems the couplings between magnetic ions in the insulating crystals are usually much stronger since the relevant physics takes place on atomic length scales. The specific nature of the exchange or coupling depends on the crystal structure. In low-dimensional systems often there is a competition between different exchange interactions possible which can lead to frustrated magnetic order. At temperatures on the order of the exchange interactions, long range magnetic order or quantum ground states can be established. In frustrated systems helical ground states which are connected to magnetoelectric behavior can be realized [55]. In magnetically ordered materials the transfer of electrical signals by spin-waves has been shown recently [4]. As a prerequisite to establishing devices based on such effects, the fundamental interactions giving rise to this behavior have to be identified. The study of the magnetic properties of low-dimensional systems with competing interactions provides insight into the fundamental magnetic interactions on the atomic scale. For this ESR is an important tool, since it allows the local magnetism of the relevant magnetic ions to be studied. ESR studies on two one-dimensional spin chains with competing interactions have been performed and are reported in this part. Among other methods, measurements of static susceptibility and magnetization were used to characterize the magnetic properties of the studied materials.

CHAPTER 5

Quasi One-Dimensional Systems

In many naturally occurring or man made solids the magnetic interactions are restricted to less than their three dimensions. This is the case when the crystal structure assembles in such a way that the couplings between spins along certain directions are much stronger than along others. There are two-dimensional systems in which interaction takes place predominantly between magnetic ions arranged in a plane [56]. In other systems magnetic ions are arranged in one-dimensional structures, forming so called spin-chains. In systems with reduced dimensionality quantum effects become more relevant and ground states can be established not observed in three-dimensional systems. Ground state properties and excitation spectra depend critically on the dimensionality of the interaction, the dimensionality of the spin and the interplay between different interactions. Let us establish the general properties for the (quasi) one-dimensional spin chain materials, relevant to the systems investigated in Chapters 6 and 7.

The nearest-neighbor Heisenberg Hamiltonian was already introduced in Section 2.6 to describe the exchange interaction as

$$\mathscr{H} = \frac{1}{2}\sum_{ij} J_{ij}\mathbf{S}_i \cdot \mathbf{S}_j \tag{5.1}$$

This generalized Hamiltonian can be used to describe the superexchange interaction between magnetic ions, as it is relevant in the spin chains from transition metal oxides.

For an isotropic spin system in which the nearest-neighbor (NN) coupling between all interacting spins is the same it writes

$$\mathscr{H} = \frac{1}{2}\sum_{ij} J\mathbf{S}_i \cdot \mathbf{S}_j \tag{5.2}$$

The Hamiltonian can be generalized for a potentially anisotropic coupling to the form

$$\mathscr{H} = \frac{1}{2}\sum_{ij} [J_x S_i^x S_j^x + J_y S_i^y S_j^y + J_z S_i^z S_j^z] \tag{5.3}$$

Since in this work we are only concerned with (quasi-)one-dimensional systems we consider only the coupling along one lattice direction, where each spin $\mathbf{S}_i$ has only two nearest neighbors. Then the Hamiltonian reduces to

$$\mathscr{H} = \sum_{i} [J_x S_i^x S_{i+1}^x + J_y S_i^y S_{i+1}^y + J_z S_i^z S_{i+1}^z] \tag{5.4}$$

The coupling between nearest-neighbor (NN) spins can be either antiferromagnetic (AFM), for $J > 0$, or ferromagnetic (FM), for $J < 0$.

According to the dimensionality n of the spin (coupling) the system can be categorized as:

$n = 1$	Ising model	$J_x = J_y = 0,\ J_z \neq 0$
$n = 2$	XY model	$J_x \neq J_y \neq 0,\ J_z = 0$
$n = 3$	XXZ model	$J_x = J_y \neq 0,\ J_z \neq 0$
$n = 3$	Heisenberg model	$J = J_x = J_y = J_z \neq 0$

The dimensionality n means that the spin can be imagined to be restricted to point along certain directions. For the Ising model [57], $n = 1$, a spin at site i can only be in the up or down configuration, represented by $S_i^z = \pm S$. For the isotropic Heisenberg model, $n = 3$, spins can point in any direction and are therefore represented by vectors $\mathbf{S}_i,\mathbf{S}_{i+1}$.

The spin dimensionality is connected to its local crystal field anisotropy. This is determined by the single ion anisotropy discussed in Section 2.5. In the absence of single ion anisotropy no restrictions are placed on the spin orientation and the spin is Heisenberg-like. The dimensionality of the spin is critical for an eventual magnetic order to occur and the excitation spectrum of the system [58]. This single ion anisotropy should however not be confused with an eventual anisotropy of the spin-spin interactions as caused by anisotropic exchange.

5.1 Magnetic Order and Excitations

In a solid the atoms at $T = 0$ are rigid except for zero-point fluctuations [59]. At finite temperatures excitations in the form of quantized lattice vibrations, the phonons, are possible. Similarly, a ferromagnet is ordered perfectly at $T = 0$ except for quantum fluctuations. The excitations in magnetically ordered solids are quantized magnons or spinons.

Mermin, Wagner [60] and independently Berezinkii [61], showed for the isotropic Heisenberg model, no long range magnetic order occurs for temperatures $T > 0$ in one- and two-dimensional systems. The situation can be rationalized as the following: The rotation of an isotropic Heisenberg spin does not cost any energy. At finite temperature spin fluctuations created by thermal fluctuations are present. Such fluctuations destroy the long range order in the low-dimensional system [11]. However, if there is a spin anisotropy present the energy costs for rotating a spin are larger. For a large enough anisotropy, as compared to the thermal energy, long range order is also established in a spin-chain system.

In a general way the Heisenberg spin-chains can be classified according to their spin value and the dominant NN interaction. One can distinguish between half-integer spins ($S = \frac{1}{2}, \frac{3}{2}, \frac{5}{2}, ...$) and integer spin systems. The NN coupling can be either FM or AFM.

In FM chains the excitations are called magnons. In the ground state of a ferromagnetic chain all spins are aligned parallel. The first excitation would be a spin-flip of a single spin. However, this excited state would not be an eigenstate of the Hamiltonian. The solution is a linear combination of the N spin sites with one flipped spin. This can be thought of as a flipped spin being effectively smeared out over the chain with N spins. This represents a collective excitation of the FM spin chain. The dispersion relation is [11]

$$E(k) = -2NS^2J + 4JS(1 - \cos(ka)) \tag{5.5}$$

where k is the wave vector and a the lattice constant.

The energy excitations in a AFM Heisenberg chains are called spinons. A spinon corresponds to two moving domain walls. The spinon dispersion relation is [11]

$$E(k) = \pi |J \sin(ka)| \tag{5.6}$$

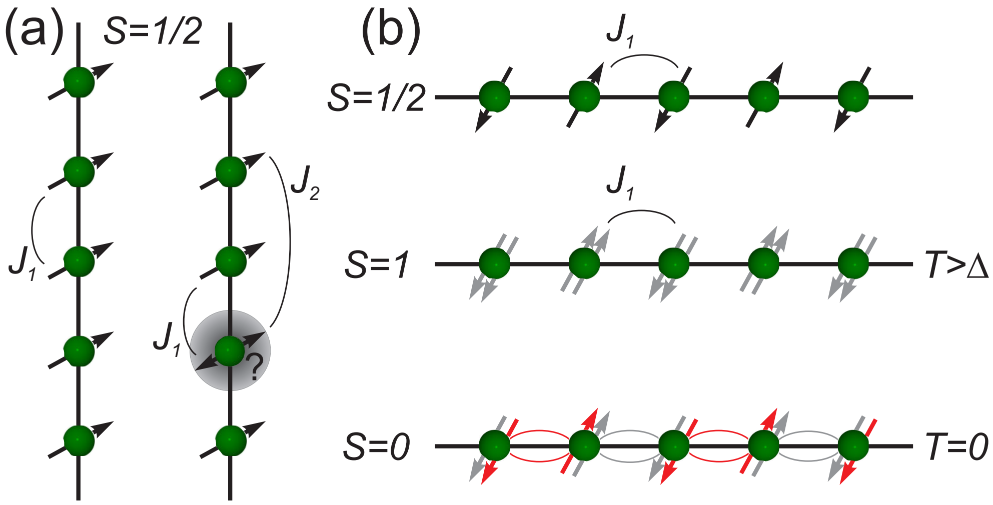

Figure 5.1: Schematic of competing interactions in different spin chains. (a) $S = 1/2$ chain with FM NN interaction J_1 and additional AFM NNN interaction J_2. The competing interaction cause a frustrated ground state. (b) Spin chain with AFM NN coupling for $S = 1/2$ and $S = 1$. For the valence-bond solid model the $S = 1$ are thought of two coupled $S = 1/2$ spins. Below a critical temperature Δ, the $S = 1/2$ spins from different atoms form a $S = 0$ ground state.

where k is the wave vector and a the lattice constant. At $k = 0, \pm\pi/a$ the energy is $E = 0$. That means that the excitation spectrum for the AFM $S = 1/2$ chain is gapless. However, a gap can be opened due to the spin-Peierls transition. This results from spin-phonon coupling which causes a dimerization along the spin chain, effectively doubling the unit cell [11]. In contrast to the AFM $S = 1/2$ chain, the initial $S = 1$ chain already exhibits a gap between its non-magnetic ground state and the excited triplet state. This will be discussed in Section 5.3.

5.2 Competing Interactions

Other interactions can be present in real systems which go beyond the simple NN Heisenberg Hamiltonian introduced before. There are other spin sites which can become relevant for the exchange: If the exchange couplings from different sites to a single spin are comparable, the ground state is degenerate. For this consider a one-dimensional spin chain with FM coupling J_1 between nearest-neighbor spins $\mathbf{S}_i$ and $\mathbf{S}_{i+1}$ [Fig. 5.1(a)]. The

AFM coupling between next-nearest neighbors (NNN) $\mathbf{S}_i$ and $\mathbf{S}_{i+2}$ can be described by the coupling constant J_2. If $J_2 \approx J_1$ the interactions for $\mathbf{S}_i$ cannot be satisfied completely. The ground state is degenerate. The system or spin is said to be frustrated.

At very high temperatures, thermal fluctuations larger than the coupling energies destroy any long range magnetic order. When such a system is cooled, a phase transition to the ordered state at temperature T_C can occur. In addition to classical phase transitions driven by temperature, phase transitions due to quantum fluctuations are possible. The critical parameter at which such a phase transition occurs is called a *quantum critical point.* Quantum phase transitions can be driven by parameters such as strain or magnetic field [11]. A quantum critical point is proposed for the frustrated spin chain with FM NN and AFM NNN interaction. Depending on the ratio between the coupling constants $\alpha = J_1/J_2$ different ground states as ferromagnetic, spin helical and antiferromagnetic order can be established in the system [11].

In real systems the boundary between one-, two- or even three-dimensional systems might not always be clean-cut. For the spin chains one distinguishes between the intra-chain or in-chain interaction J (interaction between spins within the same chain) and inter-chain interaction J' (being the interaction of neighboring spins in different chains). Typically, a good one-dimensional system is realized for $|J/J'| \approx 10^3 - 10^4$ [58]. If the coupling with spins from different chains is relevant, three-dimensional magnetic order will be established below a finite temperature T_C.

There can also be variations between the bond length within the chain causing variation of the coupling. This can lead to alternating or even random chains [62].

These kinds of competing interactions (and their combination in real systems) can lead to very complex behavior in the low-dimensional spin systems. Not only can the ground state be affected, but the excitation spectrum can also show interesting deviations from the pure magnon or spinon spectrum.

In addition to interactions with different spin sites, sometimes the model description of the system has to be extended. As mentioned before, the su-

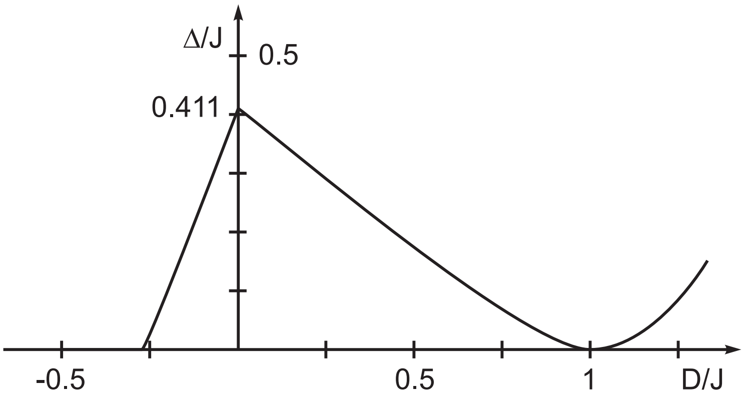

Figure 5.2: Schematic view of the Haldane energy gap Δ in dependence of the single ion anisotropy D in units of the coupling constant J for NN AFM exchange. For $D > J$ the gap is an anisotropy gap. *Reproduced from* [58].

perexchange is derived from perturbation theory. Eventually higher order terms are relevant and have to be considered to describe physics observed in experiment. In addition to the bi-linear NN coupling a bi-quadratic NN exchange has to be included in the Hamiltonian [58]:

$$\mathcal{H} = J\sum_i [\mathbf{S}_i\mathbf{S}_{i+1} + \beta(\mathbf{S}_i\mathbf{S}_{i+1})^2] \tag{5.7}$$

Depending on the strength of the bi-quadratic exchange the system can be found in different ground states. This can be very relevant for the $S = 1$ Haldane spin chain discussed in the following section.

5.3 Haldane Spin Chain

The Haldane chain is a one-dimensional Heisenberg spin chain with integer spins and antiferromagnetic nearest-neighbor coupling. Haldane predicted that the ground state of such a system would be a non-magnetic singlet state which would be separated in energy from the excited triplet state by a gap Δ [63]. This gap is not an anisotropy gap, but is due to the quantum nature of the $S = 1$ system. Haldane considered the pure Heisenberg Hamiltonian for an easy axis configuration [63]. In order to explore the limits of the Haldane phase bi-quadratic exchange and single ion-anisotropy, among other parameters, can be taken into account. Already those simple extensions reveal rich physics involved in the quasi-one-dimensional antiferromagnetic integer Heisenberg spin chains. A general Hamiltonian of the Haldane system is given in [58]:

$$\mathscr{H} = J\sum_i [\mathbf{S}_i \mathbf{S}_{i+1} + \beta(\mathbf{S}_i \mathbf{S}_{i+1})^2] + \sum_i [D(S_i^z)^2 - g\mu_B S_i^\alpha H^\alpha] \tag{5.8}$$

Here J is the energy coupling constant between neighboring spins $\mathbf{S}$. β describes the bi-quadratic exchange. Uniaxial single ion anisotropy is considered. With z being the chain direction either easy-axis (spin along the chain, $D < 0$) or easy-plane (spin perpendicular to the chain, $D > 0$) is favored. The interaction with a magnetic field H is described by the typical Zeeman term.

A good visualization of the Haldane system is the so-called valence-bond solid (VBS) as shown Fig. 5.1(b). The $S = 1$ spin at the magnetic ion is thought of two coupled $S = 1/2$ spins. Two spins on different ions with opposite spins are thought to couple strongly and form a non-magnetic singlet. The VBS state was calculated as a special realization of the Haldane phase considering bi-quadratic exchange [64], but physics for VBS and the pure Heisenberg Hamiltonian are found to be identical [58]. For larger contributions of bi-quadratic exchange other ground states are realized. Dimerized and trimerized antiferromagnetic ground states and a ferromagnetic phase have been identified [58].

Besides the bi-quadratic exchange the single ion anisotropy plays a crucial role for the realization of a Haldane system. The energy gap Δ between the singlet ground state $|0\rangle$ and the excited triplet state $|1\rangle$ directly depends on the value of D. The gap is largest for the absence of single ion anisotropy, but an energy difference exists within a certain range of D as visualized in Fig. 5.2. For $D > J$ an anisotropy gap opens.

The first material discovered to realize the Haldane system was $\mathrm{Ni(C_2H_8N_2)_2}$-$\mathrm{NO_2ClO_4}$ (NENP) [65]. Similar to the system studied in this present work NENP contains the transition element Ni realizing the chain structure in an organic matrix. NENP exhibits a single ion anisotropy [65], which results in the splitting of the excited triplet state [66] and with that an anisotropic Haldane gap. However the ground state is still the singlet state. A $S = 1$ antiferromagnetic spin chain based on Ni is investigated in Chapter 7.

CHAPTER 6

Linarite

Linarite is a natural mineral of bright blue color. $PbCuSO_4(OH)_2$ belongs to the family of cuprates in which Cu ions are arranged along chains. The Cu ions are surrounded by oxygen atoms which mediate magnetic exchange between Cu spins. Although Linarite occurs naturally, its magnetism has only been studied recently [67, 68, 69]. In this initial study combining zero-field susceptibility, specific heat data and electronic structure calculations, it was concluded that Linarite is a quasi one-dimensional spin system. It is thought to be highly frustrated due to nearest-neighbor (NN) ferromagnetic and next-nearest-neighbour antiferromagnetic couplings along the Cu chain direction. The exchange constants were found as $J_1 \approx -30\,\mathrm{K}$ and $J_2 \approx 15\,\mathrm{K}$ [68]. A magnetically ordered state is observed below temperature $T_N \approx 2.8K$ for which a helical ground state is proposed [68]. Only a brief study at room temperature probing the local magnetism in Linarite has been reported so far [70]. Local probe techniques like ESR and NMR, however, can provide further information about competing interactions in this material.

Here, a study of the paramagnetic regime of Linarite is presented in order to address the question of competing interactions in the system. The results of the ESR measurements are correlated with static susceptibility and magnetization measurements as well as NMR experiments.

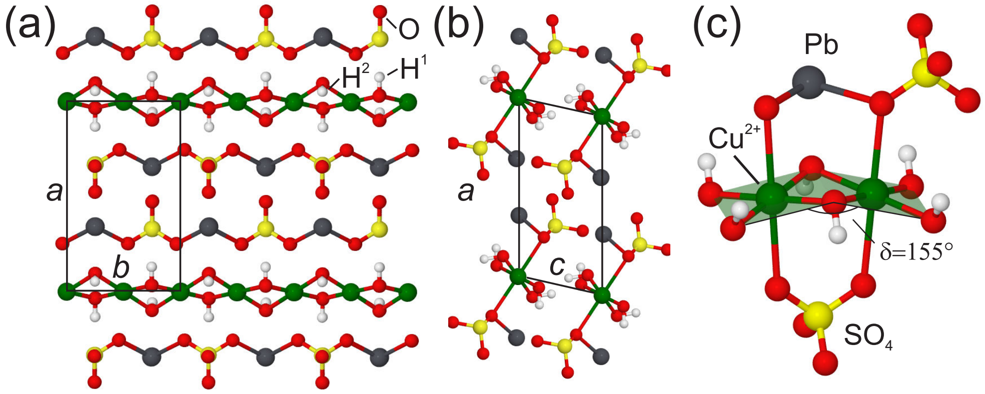

Figure 6.1: Crystallographic structure of Linarite $PbCuSO_4(OH)_2$. Shown are the view on the *ab*-plane (a), *ac*-plane (b) and a close-up (c) of the smallest unit, consisting of two tilted edge-sharing distorted octahedra. The CuO_4-planes are indicated. Crystallographic data taken from [71].

6.1 Structure

Linarite crystallizes in a monoclinic structure with the lattice constants $a = 9.682\,Å$, $b = 5.646\,Å$ and $c = 4.683\,Å$ with $\beta = 102.65°$. The Cu chain is along the *b*-direction. Cu ions are surrounded by four oxygens in an almost square plane [Fig. 6.1(c)]. The CuO_4-planes are tilted by an angle of $\delta \approx 155°$ with respect to neighboring planes. Together with the oxygens of the SO_4- and PbO_2-group this results in two tetragonal distorted octahedra tilted in a zigzag way towards and away from each other. The long axis of the octahedra (O-Cu-O) is 5.41 Å, while the short axes are 3.84 Å and 3.92 Å, respectively. As visible in Fig. 6.1 the axes of the local octahedra do not coincide with the crystallographic axes. An initial study of ESR and optical absorption spectroscopy indicated the tetragonal distorted oxygen octahedra around the Cu ions in Linarite [70].

The single crystals of $PbCuSO_4(OH)_2$ used in this study for the magnetization, NMR and X-band ESR measurements are natural minerals with their origin in California, USA (Blue Bell Mine, Baker, San Bernadino). A second set of naturally grown single crystals of smaller size (Siegerland, Germany) was used for the ESR measurements in the resonant cavity at a frequency of about 93 GHz. All crystals show well-defined facets and the principal axes *b* and *c* can be identified easily. Single crystallinity of our samples has been

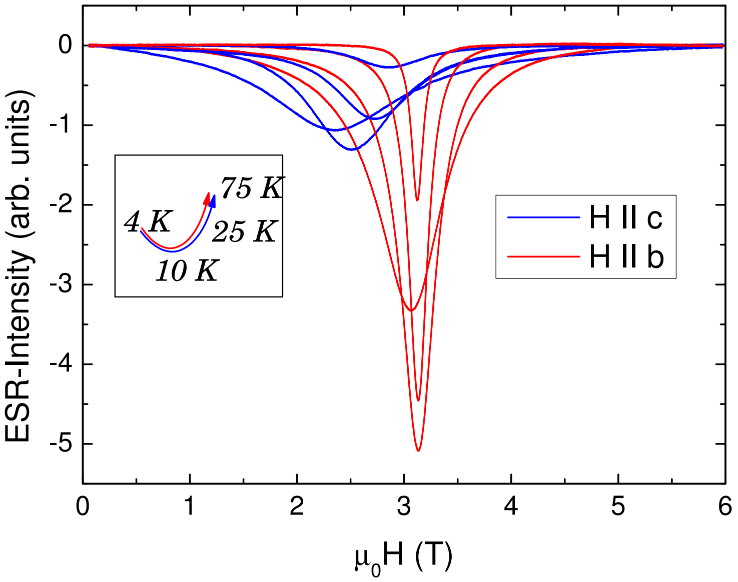

Figure 6.3: ESR spectra for different temperatures measured at 93 GHz with the magnetic field H applied along the crystallographic *b* and *c* axes. Spectra for H along *a* (not shown) are similar to spectra for H along *c*. Arrows on the left side indicate temperatures of the individual ESR spectra.

checked by X-ray diffraction. For both sets of single crystals no magnetic impurity phases as evidenced by a low temperature Curie tail in the magnetic susceptibility were observed.

6.2 Magnetization and ESR

Magnetization measurements were performed at the High Magnetic Field Lab at FZ Dresden Rossendorf by M. Uhlarz. Static susceptibility measurements were conducted by A. U. Wolter using a commercial SQUID magnetometer in the range 1.8-400 K and an external magnetic field of 0.4 T.

ESR measurements were performed at the X-band spectrometer described in Section 3.1 and using a resonant cavity at 93 GHz in combination with a 17 T magnet as described in Chapter 3.3. At a frequency of 93 GHz the ESR resonance field is found around 3 T. The spectrum consists of a single line of Lorentzian shape (Fig. 6.3). From a fit to the lines the ESR intensity, resonance field and linewidth are extracted. From those parameters the integrated ESR intensity, which is determined by the intrinsic spin susceptibility, is calculated. Since the resonator is inserted into the cryostat its

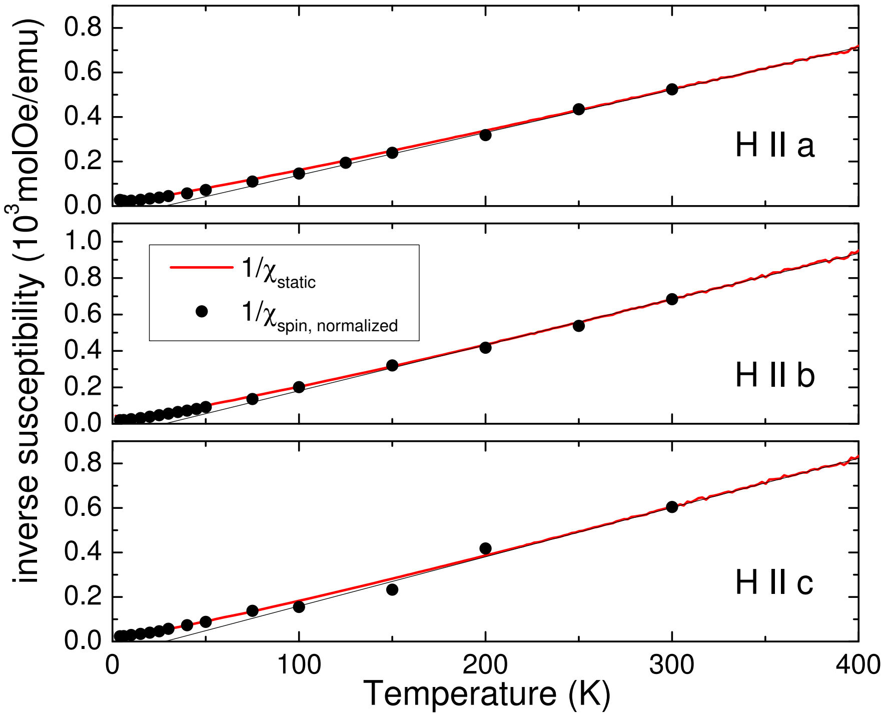

Figure 6.4: Inverse static susceptibility and inverse spin susceptibility for the external magnetic field applied along the crystallographic axes *a*, *b*, and *c*. The spin susceptibility as determined via ESR at about 3 T was normalized to the high temperature (300 K) value of the static susceptibility. Black lines indicate a Curie-Weiss-fit to the static susceptibility with $\Theta_{cw} = 28(2)$ K for all directions. *Measurement static susceptibility: A. U. B. Wolter*

quality factor Q and its resonance frequency ν_{res} change with temperature. Q and ν_{res} are determined with frequency sweeps around the resonance frequency at every temperature. The spin susceptibility χ_s and the resonance field $\mathrm{H}_{\mathrm{res}}$ are corrected accordingly. For details of this procedure see Section 3.4.6. The spin susceptibility is then normalized to the static susceptibility at 300 K.

The inverse spin susceptibility $1/\chi_s$ is plotted in Fig. 6.4 as a function of temperature together with the inverse static susceptibility. From this figure it is clearly visible that the static susceptibility coincides with the intrinsic spin susceptibility over the whole temperature range along the crystallographic directions *a*, *b* and *c*. This indicates that any temperature independent part

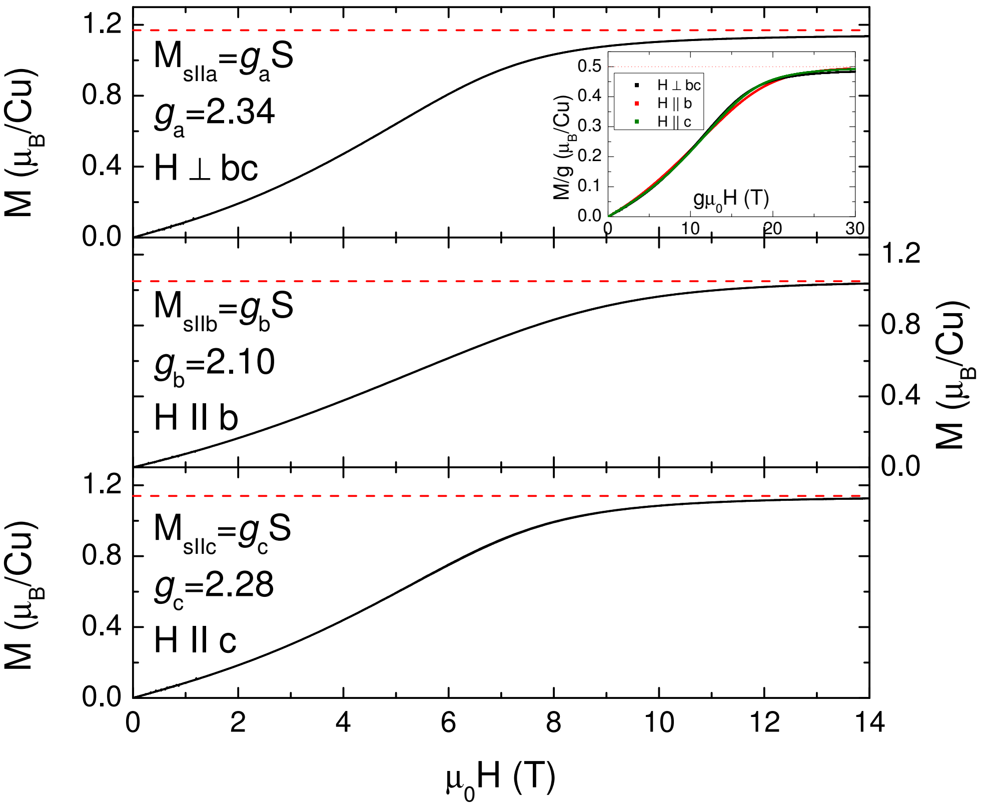

Figure 6.5: Magnetization as a function of magnetic field along different crystallographic directions at $T = 2.8\,\mathrm{K}$. The saturation magnetization $M = gS$ is indicated as a dashed line. Inset shows the spin expectation value $< S_z >= M/g$ (μ_B/Cu) as a function of the scaled magnetic field $g\mu_0 H$ along the different directions. *Measurement magnetization: M. Uhlarz*

of the static susceptibility is small and that the static susceptibility is dominated by the intrinsic spin susceptibility. However, small temperature independent contributions to the susceptibility can already influence a quantitative analysis. In agreement with the ESR measurements the intrinsic susceptibility is determined from the NMR shift in a NMR experiment. The high temperature regime (250 K-400 K) of the inverse intrinsic spin susceptibility can be fitted by a Curie-Weiss law $\chi^{-1}(T) \propto (T - \Theta_{cw})$. The resulting Curie-Weiss constant $\Theta_{cw} = 28(2)$ K is isotropic within the experimental error [72]. The Curie-Weiss behavior with $\Theta_{cw} = 28(2)$ K is indicated as black lines in Fig. 6.4. The positive Curie-Weiss-constant indicates a dominant

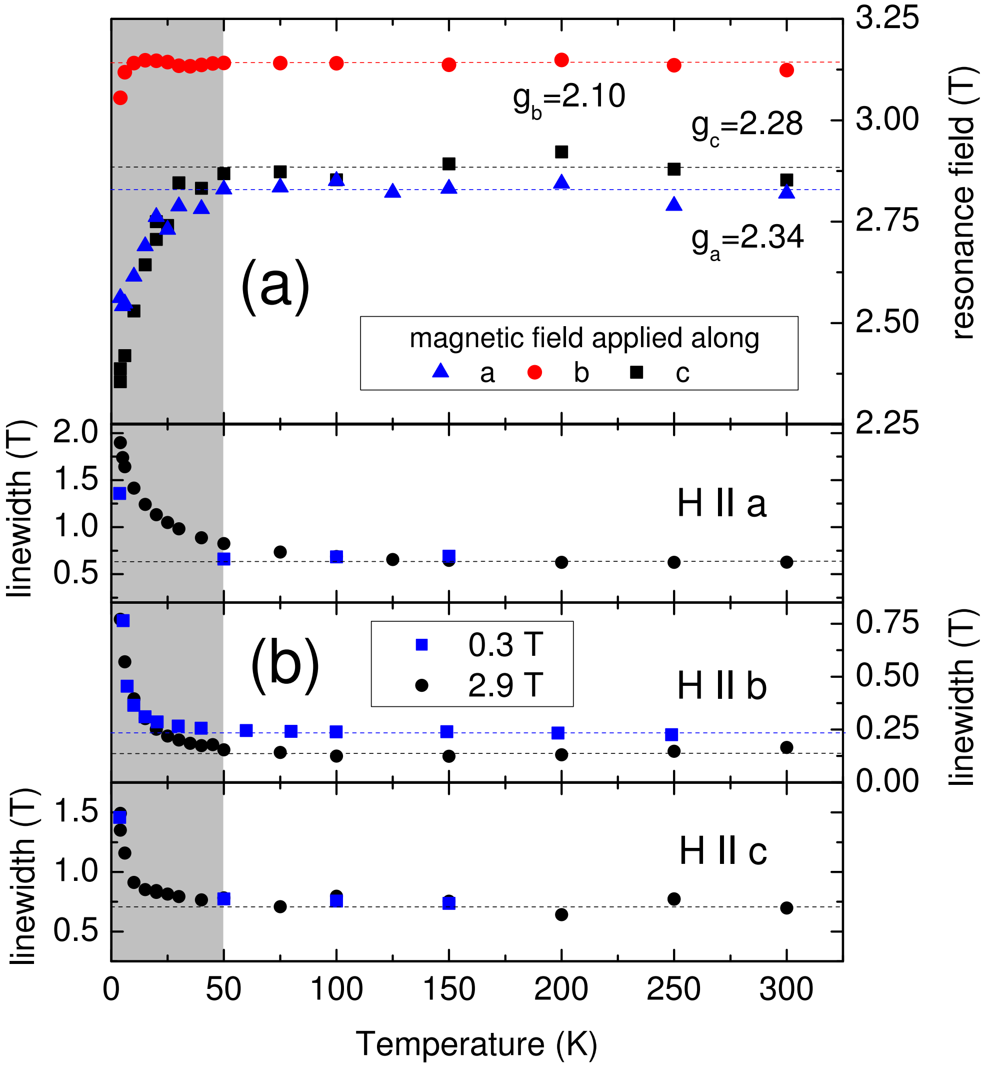

Figure 6.6: Resonance fields at about 93 GHz (a) and linewidth for resonance fields of about 0.3 T and 2.9 T (b) of the ESR signal as a function of temperature for the external magnetic field applied along the crystallographic axes *a*, *b* and *c*. The resonance field is temperature independent above temperatures of about 50 K and decreases with decreasing temperatures. For the high temperature regime the corresponding *g* factor values are listed. The linewidth is significantly smaller for H ∥ *b*. For the *b* direction the change of the linewidth depends on the applied field as approaching the ordering temperature.

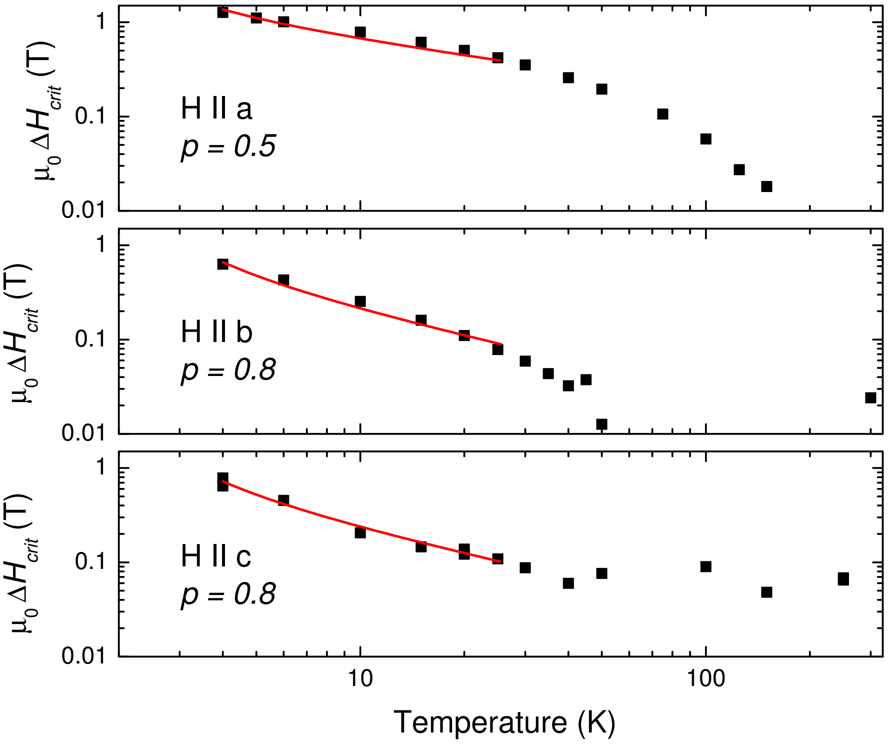

Figure 6.7: Double logarithmic plot of the critical linewidth part ΔH_{crit} as a function of temperature for the three crystallographic directions *a*, *b* and *c*. Fits to the data for temperatures up to 25 K are shown.

ferromagnetic coupling at high temperatures. However, there are significant deviations at low temperatures from the Curie-Weiss behavior. This denotes the increasing relevance of antiferromagnetic correlations.

The temperature dependence of the ESR resonance field $\mathrm{H}_{\mathrm{res}}$ and the ESR linewidth are plotted in Fig. 6.6.[1] In the high temperature regime (roughly above 100 K) resonance fields are temperature independent. From the absolute values of $\mathrm{H}_{\mathrm{res}}$ the effective g-factors can be determined as $g = h \cdot \nu / (\mu_B \mathrm{H}_{\mathrm{res}})$ along the crystallographic directions. For the high temperature regime the effective g-factors are found to be $g_a = 2.34$, $g_b = 2.10$, $g_c = 2.28$.

---

[1] Note that the resonance fields are as measured and not corrected by the temperature resonance frequency of the cavity, which can cause a shift of the order of 10 mT from 100 K to 300 K.

Based on the g-factors and the Curie-Weiss constants extensive calculations with local spin density approximation and other methods have been performed as will be published in [72]. The theoretical analysis of the experimental data gives exchange coupling constants $J_1 \approx -70\,\mathrm{K}$ and $J_2 \approx 27\,\mathrm{K}$ which were calculated with a one-dimensional and quasi one-dimensional approximation within linear spin wave theory [72]. These coupling constants are significantly higher than previously reported [68]. $\alpha = J_1/J_2 \approx -0.39$ indicates a strongly frustrated system close to the quantum critical point (see Section 5.3).

Having established the g-factors, we can analyze the magnetic anisotropy in the system. In Fig. 6.5 the magnetization curve $M(\mu_0 H)$ of $\mathrm{PbCuSO_4(OH)_2}$ as a function of field at 2.8 K for the three crystallographic main directions a, b, and c is presented. Comparing the magnetization along the different directions, it is seen that the saturation magnetization of $\mathrm{PbCuSO_4(OH)_2}$ is strongly anisotropic, with $M_{\mathrm{sat},a} \approx 1.175\,\mu_B/\mathrm{Cu}$ atom, $M_{\mathrm{sat},b} \approx 1.05\,\mu_B/\mathrm{Cu}$ atom and $M_{\mathrm{sat},c} \approx 1.15\,\mu_B/\mathrm{Cu}$ atom for the a, b and c directions, respectively. The saturation magnetization $M_{\mathrm{sat}} = gS$ is indicated as a dashed line in Fig. 6.5. In this temperature regime, the anisotropy of the saturation magnetization is well-explained by the anisotropy of the g-factor (see above). Note that there is a difference (from the g-factor) in calculated and directly measured saturation magnetization for $H \parallel a$. For the ESR experiment the magnetic field was aligned $H \parallel a$, while for the magnetization measurement the sample was intentionally aligned $H \perp bc$. For a perfect agreement in directions the saturation magnetization would be slightly larger and match the calculated value.

The inset in Fig. 6.5 shows the spin expectation value $< S_z >= M/g\ (\mu_B/\mathrm{Cu})$ of $\mathrm{PbCuSO_4(OH)_2}$ as function of the scaled field $g\mu_0 H$ at 2.8 K for the three crystallographic directions a, b, and c as derived from the experimentally determined magnetization data $M(H)$. The extracted spin expectation value corresponds to Cu spin $S = 1/2$. From the rescaled data it is seen that all curves clearly overlap and the saturation field is also explained by the anisotropy of the g-factor.

The exact assignment of the saturation field is difficult at $T = 2.8\,\mathrm{K}$, because temperature effects are still significant around the ordering temperature. Below the ordering temperature the saturation magnetic fields have been determined to be $H_{\mathrm{sat},a} \approx 7.6\,\mathrm{T}$, $H_{\mathrm{sat},b} \approx 10.5\,\mathrm{T}$ and $H_{\mathrm{sat},c} \approx 8.5\,\mathrm{T}$. These field values are significantly lower than in other cuprates, e.g. $LiCuVO_4$. In the system $LiCuVO_4$ the saturation fields were found between 40 - 50 T [73], with the exchange constants being $J_1 = -12$ K and $J_2 = 41$ K [74]. For this system the reported saturation fields are experimentally accessible with pulsed magnetic fields only. Linarite, however, can be investigated in a typical laboratory magnet up to the saturation fields. This offers possibilities to study effects close to the saturation field, such as a recently proposed multipolar phase [75] which might exist in Linarite [76].

As shown in Fig. 6.6 the ESR linewidth is strongly anisotropic. At a frequency of 93 GHz corresponding to a resonance field of about $H_{res} \approx 3$ T the linewidth $\Delta H_{H\|b} \approx 0.1$ T is much smaller than $\Delta H_{H\|a,c} \approx 0.7$ T. Furthermore, ΔH is almost constant or only weakly dependent on temperature above 50 K. At the X-band frequency of about 9.6 GHz – corresponding to a resonance field of $H_{res} \approx 0.3$ T – the temperature dependence of the ESR signal shows a similar behavior for the crystallographic axes *a*,*b* and *c* (blue squares in Fig. 6.6). The linewidth along *a* and *c* are, within the uncertainty of the measurement, identical to the linewidth at higher fields. The decreasing intensity of the ESR signal with increasing temperature makes it difficult to analyze the lines quantitatively along those directions up to room temperature, however the linewidth appears to stay constant as well. For the *b* direction the linewidth is constant in the high temperature regime and fairly narrow with $\Delta H \approx 0.25$ T. However, this is unexpected since it is broader than for the larger applied field of 3 T. This effect can be explained by the strongly anisotropic linewidth together with a slight misalignment of the sample of about 10° for this particular measurement.

As temperatures fall below 100 K a broadening of the lines for both fields is observed. The small resonance field of about 0.3 T limits the reliability of the measurements for directions *a* and *c* since the linewidth exceeds the resonance field and a fit to the data cannot be accurate anymore. However the values are close to the linewidth for the ten-times larger field of 3 T. At temperatures below 25 K the linewidth for $H \parallel b$ becomes almost identical for both applied fields. Towards lower temperatures the anisotropy in the linewidth becomes increasingly smaller and the effect of misalignment is reduced.

The overall broadening as a function of temperature is different for the individual crystallographic directions. The linewidth in ESR depends on (dipolar) spin-spin interactions, anisotropic exchange as well as on development of internal magnetic fields. The fact that the linewidth is the same for different applied fields indicates that inhomogeneous broadening effects are rather small. As we approach lower temperatures the spin-spin correlation length increases and short range magnetic correlations develop. The change of linewidth as a function of temperature can give information about the dimensionality and type of interactions in the system [77, 78]. The broadening as approaching the ordering temperature can be analyzed in terms of

$$\Delta H = \Delta H_0 + \Delta H_{\mathrm{crit}}((T - T_N)/T_N)^{-p} \tag{6.1}$$

The linewidth ΔH is divided into a non-critical part ΔH_0 and a temperature dependent critical part ΔH_{crit} [56]. The exponent p can give information about the dimensionality of a correlated spin system and its change by approaching a long-range ordered ground state. Fits to our data over the low temperature range with fixed $T_N = 2.0\,\mathrm{K}$ for $H_0 = 3\,\mathrm{T}$ give critical exponents from $p = 0.5-0.8$ (Fig. 6.7).[2] For one-dimensional Heisenberg antiferromagnets the critical exponent was found to be around a value of $p = 2.5$ [79]. In layered compounds with FM and AFM coupling comparable values have been reported. However, close to the ordering temperature a crossover to critical exponents of $p \approx 0.6$ is reported [80, 56]. This is interpreted as the appearance of three-dimensional antiferromagnetic fluctuations.

The broadening in our system can be described with critical exponents $p \approx 0.6$ up to $T \approx 30\,\mathrm{K}$, i.e. temperatures which are 15 times higher than the actual ordering temperature of 2.0 K (at 3 T). This indicates significant magnetic fluctuations at elevated temperatures, suggesting that appreciable interchain and interlayer correlations are present well above T_N. The three-dimensional ordering does not occur until much lower temperatures, which indicates a strongly frustrated system with competing interactions of the order of the energy scale of $\sim 50\,\mathrm{K}$.

When approaching the ordering temperature a shift in the resonance field $\mathrm{H}_{\mathrm{res}}$ is also observed. A shift of the resonance position of an ESR signal as a function of temperature is associated with the development of internal magnetic fields in the system. Along the b direction the shift is observed only at temperatures close to the ordering temperature T_N. This shows that an internal field develops along the chain direction only when the actual three-dimensional ordering occurs. Along a and c directions a shift in the resonance field is already observed at much higher temperatures starting around 50 K and developing smoothly with decreasing temperature. The developing static internal fields are much larger perpendicular to the one-dimensional chain direction, where an internal field builds only when the actual three-dimensional ordering occurs.

---

[2] Note that the ordering temperature T_N depends on the applied magnetic field. Several phase transitions have been observed as a function of magnetic field. At $H = 3\,\mathrm{T}$ the three-dimensional ordering is observed at $T = 2.0\,\mathrm{K}$.

6.3 NMR

NMR experiments were conducted by A. U. B. Wolter, M. Schäpers and R. Vogel at the IFW Dresden. The results for the paramagnetic regime of Linarite will be published in our joint publication [72]. Selected NMR results are discussed here to further support the ESR findings.

In Figs. 6.8 the linewidth of the ^{1}H-NMR spectra is shown as a function of temperature for all three crystallographic directions a, b and c. In the insets the ^{1}H NMR spectra are shown exemplarily for an applied magnetic field of 2 T, and for three different temperatures between 10 K and 150 K. There are two different hydrogen sites (H^1, H^2 in Fig. 6.1) which can be well distinguished as two lines in the NMR data along a and c. In the paramagnetic phase the spin-echo signal of all NMR spectra have rather isotropic Lorentzian lineshape. Since the linewidth at high temperatures is very small, i.e., about 10-25 kHz for all spectra and for all three crystallographic main directions, a very good quality of the single crystal $PbCuSO_4(OH)_2$ can be assumed. Note also that for the ^{1}H-NMR spectra for $H \parallel b$ two Lorentzian lines have been used to fit the data since the two NMR lines do not perfectly overlap at low temperatures. This can probably be ascribed to a non-perfect alignment of the sample $\parallel b$. A misalignment $< 5°$ can easily lead to a small resolved splitting of the NMR lines below ~ 50 K for this direction. In Fig. 6.8 the average of the obtained values for the linewidth of both ^{1}H-spectra has been plotted for $H \parallel b$.

Similar to the ESR linewidth, the temperature dependence of the full width at half maximum (FWHM) of the NMR spectra is expected to give access to the dynamics of the magnetic correlations and thus to the dynamical critical properties in the paramagnetic regime upon approaching T_N. The NMR

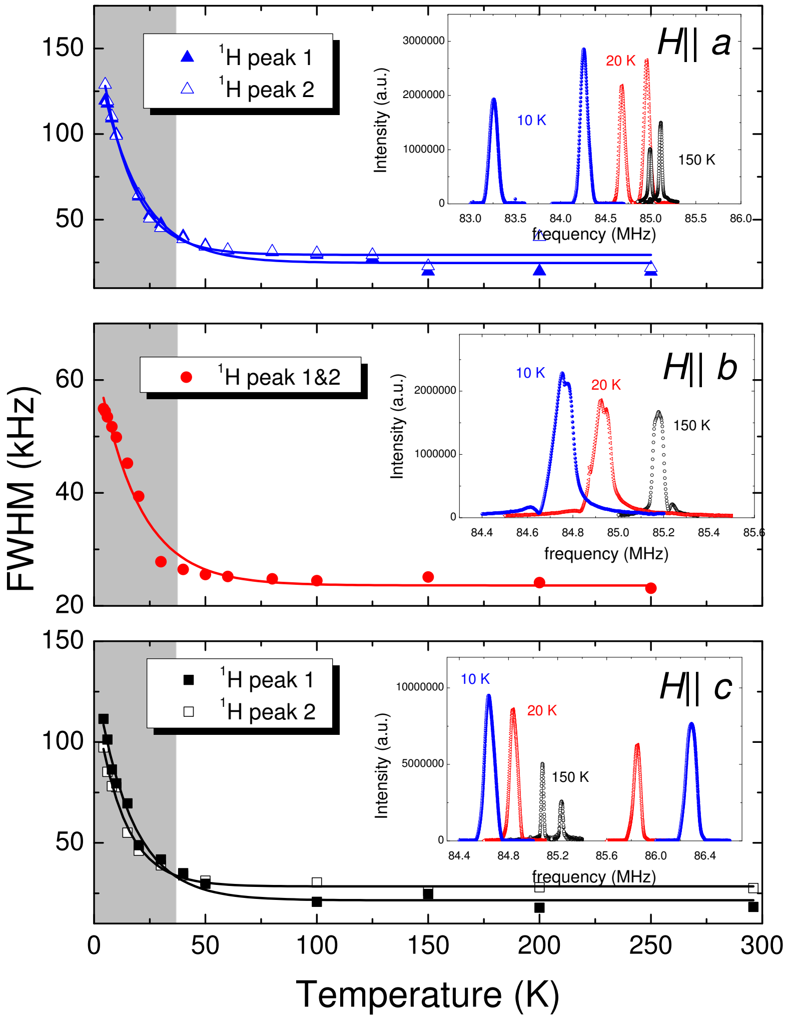

Figure 6.8: The ^{1}H-NMR linewidth of $PbCuSO_4(OH)_2$ as a function of temperature in an external magnetic field of $\mu_0 H = 2\,\mathrm{T}$ parallel to the three crystallographic main axes a, b and c. The lines represent guides-to-the-eyes. In the insets the ^{1}H-NMR spectra are shown for three different temperatures 10 K, 20 K and 150 K. The different intensities at different temperatures are not to scale. Note that the small resolved splitting of the line for $H \parallel b$ is probably associated with a small misalignment $< 5°$ of the crystal with respect to the b axis; for details see text. *Data and figure from* [72].

linewidth is related to the nuclear spin-spin relaxation time T_2 and thus probes the transverse component of the two-spin correlation function and the temporal spin fluctuations of the magnetic system near the critical temperature. In cuprate compounds anisotropic contributions to the magnetic exchange interactions are commonly present. Therefore it can be expected that also in Linarite the NMR linewidth is dominated by spin fluctuations along the magnetic easy-axis, with spin fluctuations perpendicular to the easy axis remaining constant and only contributing to the non-critical broadening. Henceforth, taking into account the linewidth probes transverse spin fluctuations, the broadening of the NMR line should be most prominent for magnetic fields perpendicular to this (easy)-axis, the b-axis in this system.

For all NMR spectra $\parallel a, b, c$ a pronounced broadening of the line has been observed below $\sim 50\,\mathrm{K}$ for the ^{1}H spectra. This pronounced broadening points to the short range order already present at temperatures $T \gg T_N$. Comparing the response for the three different crystallographic directions, one can easily see that the broadening is much more pronounced for the directions perpendicular to the Cu chain. The latter is in perfect agreement with the results obtained from the temperature dependence of the ESR linewidth and emphasizes the magnetic anisotropy in the system.

6.4 Summary and Conclusion

Linarite is a frustrated one-dimensional spin chain with ferromagnetic NN and antiferromagnetic NNN interaction. Based on the g-factors and the Curie-Weiss constants, exchange coupling constants $J_1 \approx -70\,\mathrm{K}$ and $J_2 \approx 27\,\mathrm{K}$ could be calculated with a one-dimensional and quasi one-dimensional approximation within linear spin wave theory as will be published in [72]. This is significantly higher than previously reported [68]. The exchange integrals indicate a strongly frustrated system with $\alpha = J_1/J_2 \approx -0.39$ close to the quantum critical point. In the paramagnetic regime the g-factor anisotropy can well-explain the saturation magnetization and the saturation magnetic field. A broadening of the ESR and NMR linewidths already occurs at temperatures much higher than the actual ordering temperature. The quantitative analysis of the critical part of the ESR linewidth yields critical exponents $p \approx 0.7$ typical for a (one-dimensional) Heisenberg system very close to the ordering temperature. However the fit can describe the data not only very close to T_N, but up to temperatures of more than $T \approx 10T_N$. This indicates the presence of significant interlayer and interchain correlations at higher temperatures. The fact that the ordering does not occur down to $T_N \approx 2.8\,\mathrm{K}$ points to a comparable energy scale of the frustration in agreement with the calculated exchange integrals.

6.5 Outlook

Magnetization, specific heat and NMR measurements have already been carried out below the ordering temperature [81]. Depending on the applied magnetic field multiple phase transitions have been revealed. Recently a ferroelectric transition has been reported in conjunction with the Néel-transition [82]. Further experiments are going to be conducted, or are already in progress, to identify the rich physics in the ordered state and around the ordering temperature of Linarite as a function of applied magnetic field.

CHAPTER 7

The Ni-hybrid $NiCl_3C_6H_5CH_2CH_2NH_3$

Organic compounds can arrange in polymer-like structures and exhibit unique features. Their functionality ranges from medical applications to organic opto-electronics [83] and solar cells [84, 85].

In hybrid materials organic structures are combined with inorganic metal ions. Usually these hybrid systems are grown in solution and arrange into self-assembled structures. The magnetism, originating from the transition metal ions, is often characterized as that of a low-dimensional spin system.

7.1 Structure

Samples of $NiCl_3C_6H_5CH_2CH_2NH_3$ were synthesized by A. Arkenbout at the Zernike Institute of Advanced Materials at the University of Groningen. The description of the general synthesis procedure and primary characterizations are described in [86].

The Ni-hybrid samples were grown in ethanol solution and consist of an anorganic backbone of Ni atoms in the octahedral environment of six chlorine atoms. The crystallographic structure is shown in Fig. 7.1. An almost perfectly symmetric octahedron is realized, with the angle between Cl-Ni-

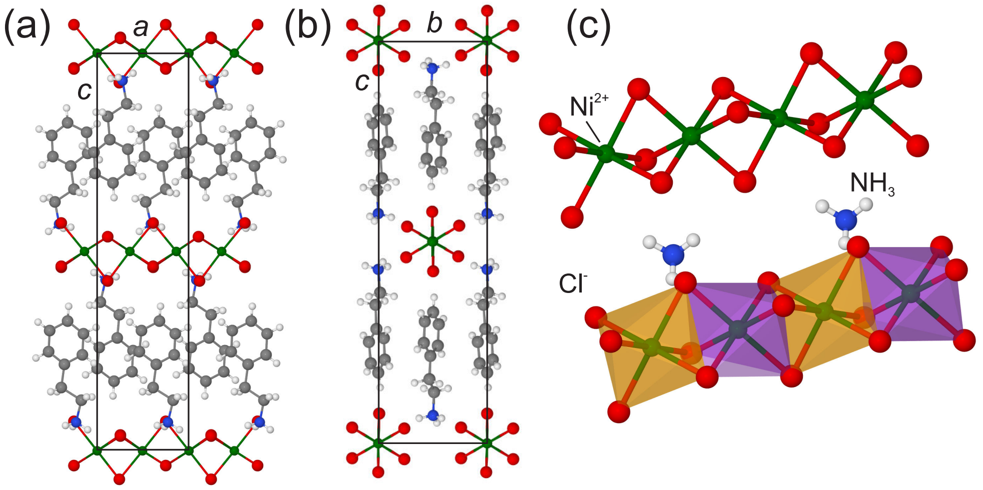

Figure 7.1: Crystallographic structure of the Ni-hybrid $NiCl_3C_6H_5CH_2CH_2NH_3$. Shown are the view on the *ac*-plane (a), *bc*-plane (b) and a close-up (c) of two chains where the face-sharing octahedra are highlighted.

Cl found to be $\beta_1 \approx 86°$ and $\beta_2 \approx 94°$. For Ni-Cl-Ni the angle is about $\gamma \approx 75°$. Along the *c*-direction the individual Ni-chains are separated by a large organic complex consisting of a benzene structure with an amino group connected to it by two carbon atoms. In the *b*-direction the NiCl-octahedra are separated directly through hydrogen bonds between chloride and the amino group.

Ni atoms enclosed in an octahedron of oxygen or chlorine are usually in the Ni^{2+} $3d^8$ configuration with an effective spin moment of S=1 [9]. The intra-chain coupling between Ni(II)-ions is mediated by the surrounding Cl atoms of the face sharing octahedra. The angle of $\gamma \approx 75°$ indicates an overlap of the Cl orbitals, thus an AFM super-exchange is expected for the Ni ions along the chain. From the structural information alone this system seems to be a promising candidate for a Haldane system based on the magnetism of Ni^{2+}.

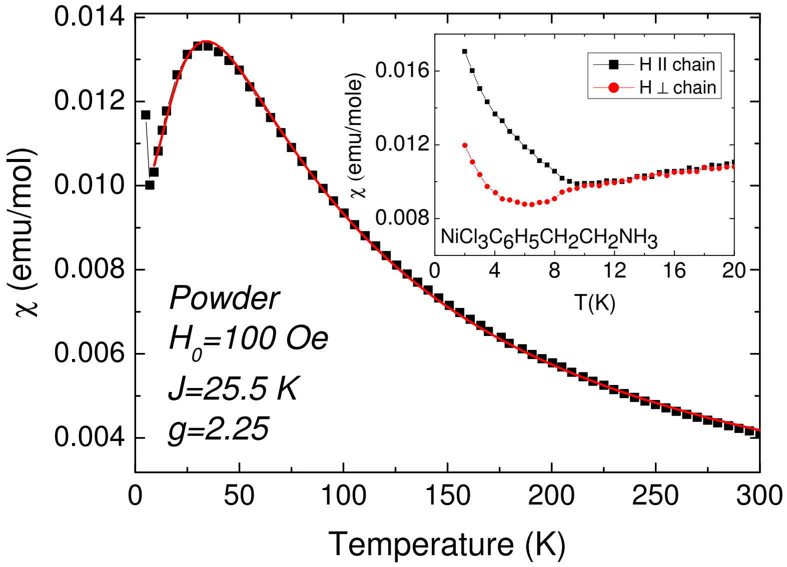

Figure 7.2: Static susceptibility as a function of temperature. A broad maximum around $T \approx 25\,\mathrm{K}$ is visible. Inset shows the low temperature susceptibility measured on single crystals with magnetic field parallel and perpendicular to the chain direction. *Measurements: A. Arkenbout*

7.2 Susceptibility and Magnetization

Static susceptibility was measured initially by A. Arkenbout at powder samples as a function of temperature at an external magnetic field of 0.01 T (Fig. 7.2). The static susceptibility increases with decreasing temperatures and shows a broad peak with a maximum around 30 K. The susceptibility then decreases down to about 10 K. This is the expected behavior for a one-dimensional spin system. For a magnetically isotropic one-dimensional system with antiferromagnetic coupling the Weng equation can be used to fit the temperature dependence of the static susceptibility [87]. Weng calculated the temperature dependence of the susceptibility for isotropic S = 1 ring systems [88].

$$\chi_{S=1} = \frac{N\beta^2 g^2}{k_B T} \cdot \frac{2 + 0.019\alpha + 0.777\alpha^2}{3 + 4.346\alpha + 3.232\alpha^2 + 5.834\alpha^3} \tag{7.1}$$

with $\alpha = J/(k_B T)$ and N the number of spins. For the fit (Fig. 7.2) to the static susceptibility data, the g-factor was kept fixed with $g = 2.25$ and no temperature independent offset χ_0 was assumed. The equation reproduces

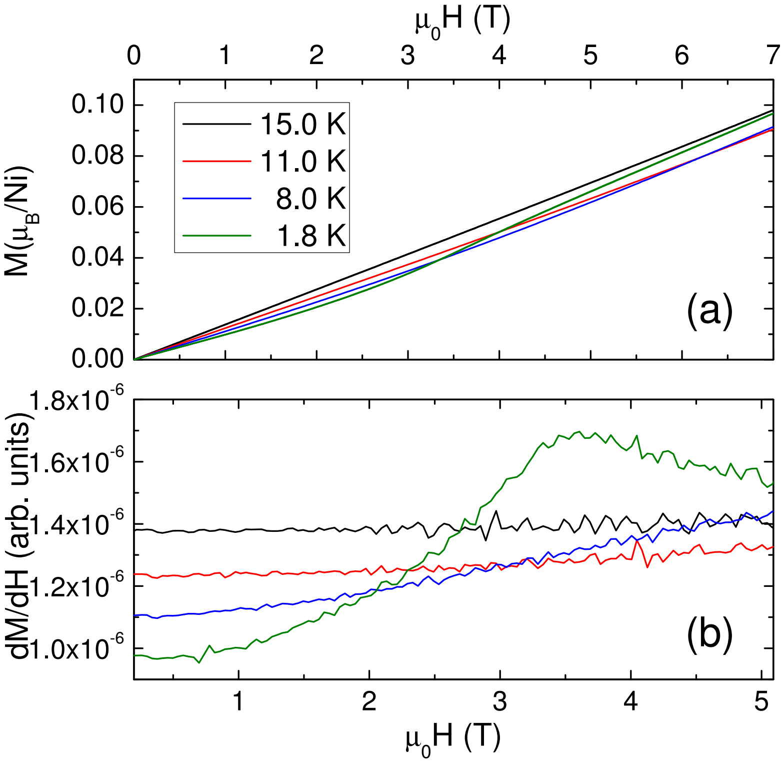

Figure 7.3: Magnetic field dependence of the magnetization (a) and its derivative dM/dH (b) on powder sample. For T = 15 K a linear increase in the magnetization with magnetic field is observed. At the lowest temperature a spin-reorientation is visible.

the static susceptibility. From the fit an exchange constant of $J = 25.5\,\text{K}$ is extracted. For a Heisenberg spin chain with integer spin moment $S = 1$ a Haldane gap system is predicted. In the absence of single ion anisotropy the Haldane gap is maximal and can be calculated from the exchange constant as $\Delta_H = 0.411 \cdot J$ (see Section 5.3) [58]. With $J = 25.5\,\text{K}$ a Haldane gap of $\Delta_H = 10.5\,\text{K}$ is expected.

In a Haldane system the ground state is a non-magnetic singlet state. Therefore the susceptibility should go to zero with decreasing temperature. The static susceptibility indeed decreases down to temperatures around 10 K, but below that temperature a minimum is visible followed by an increase in the static susceptibility with decreasing temperatures (Fig. 7.2).

Susceptibility measurements on powder samples at fields of up to 3 T were conducted at the IFW. The susceptibility does not depend on the applied magnetic field down to about 10 K. In the low temperature regime an increase of susceptibility is observed for all applied fields. Measurements on single crystals show that the static susceptibility is isotropic down to about 10 K. Below that temperature, the static susceptibility shows a minimum and an anisotropic increase, different for the magnetic field applied along the chain direction and perpendicular to it (Inset Fig. 7.2). A Curie-like increase in the susceptibility is often associated with paramagnetic impurities present in the sample. Susceptibility from impurities could dominate over the vanishing susceptibility of a Haldane system. However, this cannot explain the anisotropy observed.

The magnetization as a function of applied magnetic field was determined at temperatures of 1.8, 8, 11 and 15 K up to 7 T (Fig. 7.3). While at a temperature of 15 K the magnetization increases linearly with the applied field, at 1.8 K it shows a non-linear behavior with an inflection point at about 3.5 T. This is clearly visible in the derivative of the magnetization in Fig. 7.3(b). For the intermediate temperatures deviations from the linear increase can already be observed, but the effect is drastically reduced. Such an inflection is usually associated with a spin-flop transition of a magnetically ordered antiferromagnetic system, i.e. a reorientation of spins in the increasing external field. This points to an AFM ordering.

An AFM ordering is also consistent with the susceptibility data at low temperatures. For the easy axis of an antiferromagnet the susceptibility should go to zero, while for the easy plane it should stay constant with decreasing temperature. The susceptibility measured on the single crystals can be interpreted as a sum of that of an antiferromagnetic state and that of paramagnetic impurities. The direction perpendicular to the chain is the easy axis of the system. Note here that the Haldane system $PbNiMg_2V_2O_8$ orders antiferromagnetically, upon substitutional doping of Ni with Mg (S=0 impurities). In contrast to the investigations in this work, the Curie tail observed in the susceptibility of doped $PbNiMg_2V_2O_8$ is suppressed at the onset of AFM order [89]. This indicates that in the Ni-hybrid (not all) impurities are involved in the magnetic ordering.

The total magnetization is quite small with M $\approx 0.1\mu_B/$Ni at the maximum

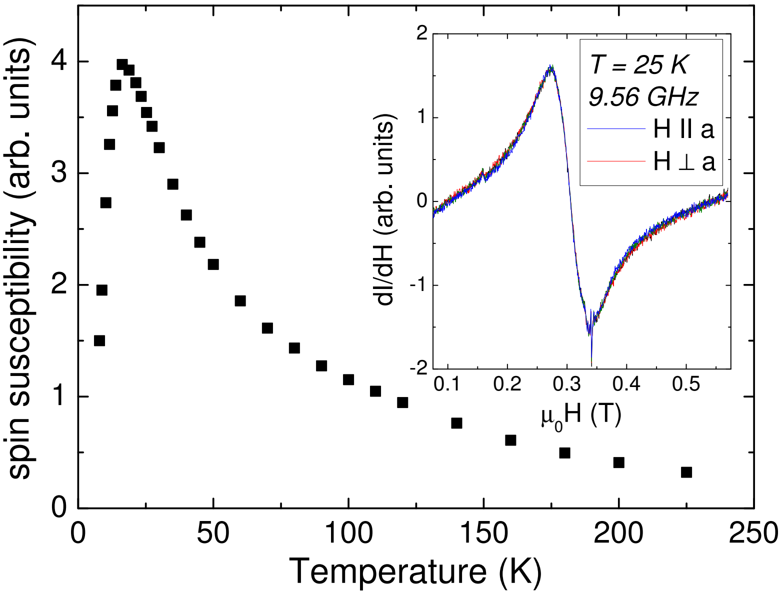

Figure 7.4: Temperature dependence of the spin susceptibility as determined from ESR measurements around 9.56 GHz. Inset shows the ESR-spectra at a temperature of $T = 25$ K for magnetic fields applied parallel and perpendicular to the chain direction.

field of 7 T. For the Ni^{2+} ions contributing to the magnetization a saturation field of $M_{sat} = gS = 2.25\,(\mu_B/\mathrm{Ni})$ is expected. This is consistent with one-dimensional Heisenberg AFM as well as Haldane systems, in which the saturation magnetization can often not be reached even in fields up to 40 T [89, 90].

In conclusion, the results of static susceptibility and magnetization indicate a one-dimensional spin chain which exhibits an antiferromagnetic ground state with the easy axis perpendicular to the chain direction and a spin-flop transition at 3.5 T. A certain amount of impurities is present in the sample.

7.3 ESR

To get a more detailed picture about the physics of this one-dimensional system ESR measurements were conducted. ESR is a very sensitive tool with which to investigate the magnetic properties in detail and give informa-

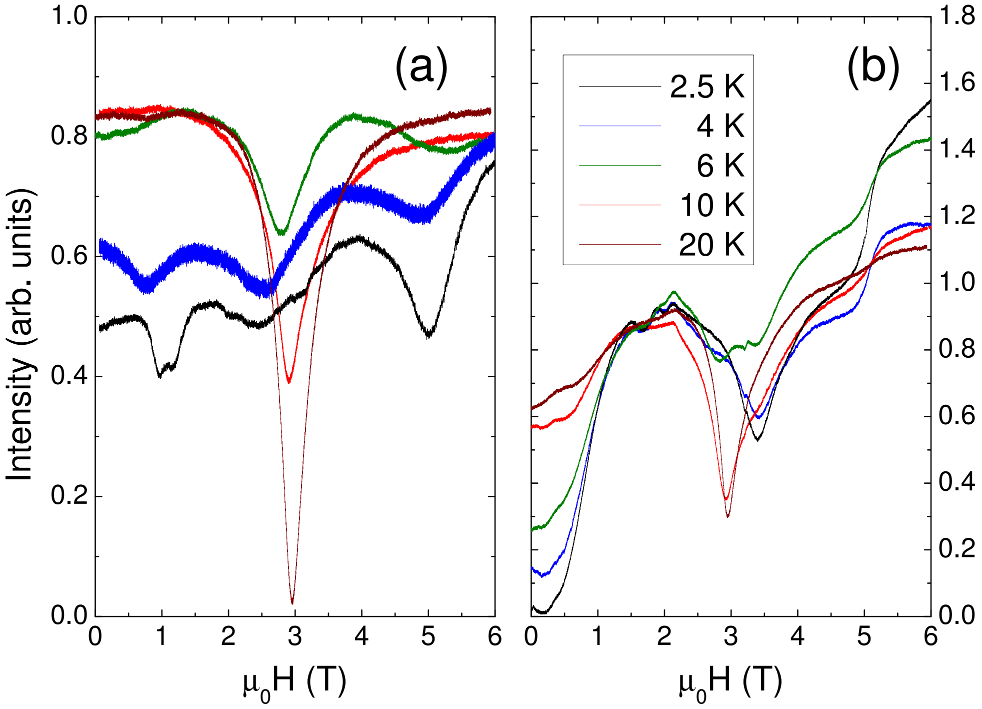

Figure 7.5: ESR spectra with magnetic field perpendicular to the chain (a) and along the chain (b) for temperatures from 20 K down to 2.5 K. While the central line decreases additional lines develop with decreasing temperature.

tion about the different energy states in one-dimensional Heisenberg antiferromagnets [66, 94, 95, 92, 96, 97]. ESR measurements were performed on single crystals of the Ni-hybrid with resonant cavities at frequencies of 9.6, 50, 83 and 93 GHz and with the quais-optical setup at frequencies of 249 and 330 GHz as well as on a powder sample at frequencies up to 360 GHz. For the measurements at 9.6 GHz, several single crystals were aligned on a teflon bar to increase the signal/noise ratio. A spectrum at $T = 25$ K is shown in Fig. 7.4 (inset) for external magnetic fields applied along the chain direction and perpendicular to it. The resonance signal exhibits a Lorentzian line around a resonance field of about 0.3 T corresponding to a g-factor of $g = 2.25$. This g-factor is typical for a Ni^{2+} ion in an octahedral crystal field [9]. The ESR signals are almost perfectly isotropic over the whole temperature range down to about 8 K. The almost fully isotropic ESR signal indicates the absence of single ion anisotropy ($D = 0$) in the present system. This means that an isotropic Heisenberg spin system is realized in the para-

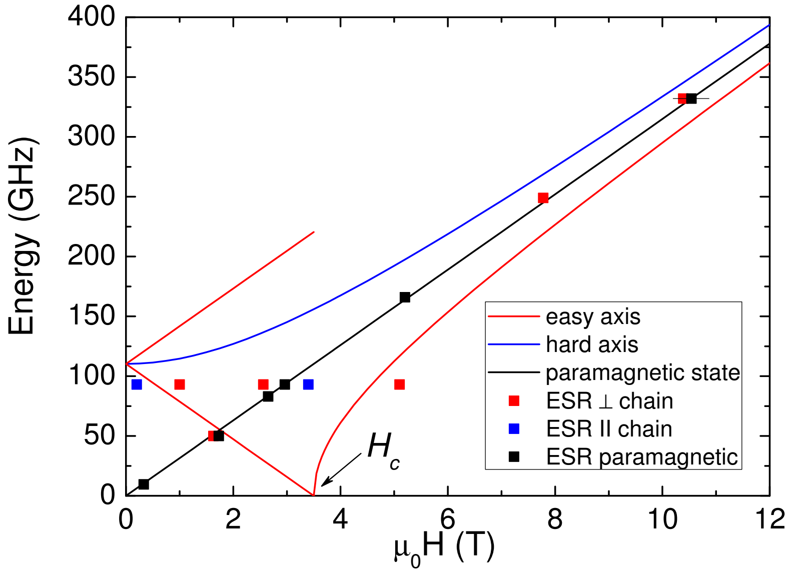

Figure 7.6: Frequency vs. magnetic field plot. Squares display the paramagnetic ESR signal for temperatures above 10 K. Circles indicate the ESR resonance field at a certain frequency from single crystals with magnetic field perpendicular to the chain at temperatures between 2.5-4 K and triangles parallel to the field. The behavior for AFM resonances are indicated along the easy axis and the easy plane. The critical field H_c corresponds to the spin-flop observed in the magnetization measurement.

magnetic state which is very favorable for the realization of a Haldane system. From Lorentzian fits to the data the intrinsic spin susceptibility can be calculated and its temperature dependence is plotted in Fig. 7.4. The spin susceptibility shows a maximum around 20 K with a sharp decrease at the low temperature side. This decrease reflects the broadening and the strong decrease in the amplitude of the resonance. It is clearly visible that, in comparison to the static susceptibility, the spin susceptibility exhibits an enhanced maximum and a steeper decrease when going to lower temperatures. From Fig. 7.4 it is visible that towards zero temperature the spin susceptibility would approach zero susceptibility. However, below 8 K the signal cannot be observed. The spin susceptibility is not subjected to temperature independent offsets as the static susceptibility. Therefore this clear tendency towards zero spin susceptibility indicates that the Ni spin system (giving rise to this spectrum) behaves as a Haldane system down to 8 K (com-

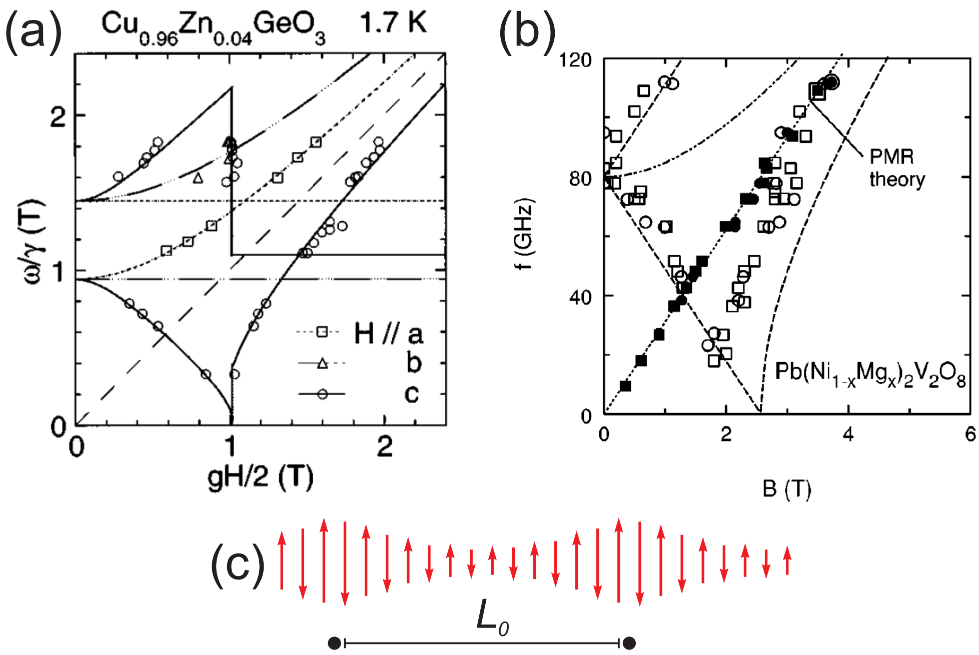

Figure 7.7: Frequency vs. magnetic field plot of doped (a) $CuGeO_3$ [91] and (b) $PbNiV_2O_8$ [92]. (c) Spatially varying antiferromagnetic order. The magnetic moments are maximal around the dopants with distance L_0. *Reproduced from* [93].

pare NMR shift in [98]). This is in contrast to the observed magnetic order in the static susceptibility and magnetization measurements.

However there can be other spin subsystems present which cannot be observed at frequencies around 10 GHz, especially as resonances attributed to the AFM ordering observed in susceptibility and magnetization are outside of the field range of the spectrometer. Thus, ESR experiments at higher frequencies and higher magnetic fields were performed.

In all ESR measurements from 10-360 GHz a single isotropic line is observed for temperatures above $T \approx 10\,K$. Fig. 7.5 shows the ESR spectra at a frequency of about 93 GHz for selected temperatures between 20 K and 2.5 K measured on one single crystal. ESR spectra with the magnetic field perpendicular to the chain direction are shown in Fig. 7.5(a). At 20 K only a single Lorentzian line is visible, in agreement with the experiments at 10 GHz. With decreasing temperature this line decreases in intensity and shifts to lower fields. Two additional lines appear and become stronger with decreasing temperatures at about 1 T and 5 T. This is a new feature not observed at lower frequencies.

For the magnetic field parallel to the chain [Fig. 7.5(b)], the central line also decreases, but shifts to higher fields. At almost zero magnetic field another feature appears. However it is not clear if the minimum of the spectrum is fully visible. That is why the absolute value of the resonance field extracted cannot be very accurate. At around 5 T another feature is observed which appears phase-shifted with respect to the central line. This probably does not originate from the main crystal and could be a spurious effect due to some fragment at another position in the resonator.

The observed peaks are plotted in a frequency vs. magnetic field chart in Fig. 7.6. The paramagnetic lines at temperatures above 10 K show a linear dependence with the slope $g = 2.25$. The theoretical equations [99, 100] for resonances of a collinear antiferromagnet are shown as red lines (along the easy axis) and a blue line (perpendicular to the easy axis):

$H \parallel$ easy axis, $H < H_c$:

$$\nu_{1,2} = \Delta \pm \frac{g\mu_B}{h} H \tag{7.2}$$

$H \parallel$ easy axis, $H > H_c$:

$$\nu_1 = 0 \qquad \nu_2 = \sqrt{\left(\frac{g\mu_B}{h} H\right)^2 - \Delta^2} \tag{7.3}$$

$H \perp$ easy axis:

$$\nu = \sqrt{\left(\tfrac{g\mu_B}{h} H\right)^2 + \Delta^2} \tag{7.4}$$

where $H_c = 3.5\,T$ is the spin-flop magnetic field value taken from the magnetization, $g = 2.25$ and the gap at zero field $\Delta = \frac{g\mu_B}{h} H_c$. As known from the susceptibility measurements on the single crystal the easy axis is perpendicular to the chain. The side peaks at 93 GHz for this direction roughly agree with the theoretical AFM resonance modes. Correspondingly, so does the in-chain direction to the easy-plane direction. At 50 GHz the AFM resonance modes coincides with the field of the paramagnetic behavior, so the observed spectrum cannot be attributed. One can see that the central lines observed at 93 GHz cannot be related to the AFM order directly. It seems that the initial paramagnetic line decreases as the state gets thermally less populated, but is still observable at 2.5 K. It is still subjected to the internal magnetic fields caused by the antiferromagnetic order in its vicinity. The presence of two signals of different origins point to a coexistence between Haldane and antiferromagnetically ordered state.

A coexistence between singlet quantum ground state and classically ordered state has been observed in Zn and Si doped $CuGeO_3$ [93]. Undoped $CuGeO_3$ is a Heisenberg antiferromagnetic spin chain with $S = 1/2$ which undergoes a spin-Peierls transition around 14 K [101]. The spin-Peierls transition is a transformation from a linear AF chain to an alternating AF or a dimerized chain, due to spin-phonon coupling [102, 11]. There exists an excitation gap between ground and excited states. When $CuGeO_3$ is doped with Si on the site of Ge, local strain deforms the lattice locally and prevents the dimerization [103]. A staggered magnetization is then found around the doping centers and an antiferromagnetic order is established. By doping with Zn at the Cu site an antiferromagnetic order is established [104], which is attributed to staggered moments around the chain end spins. Upon doping with Zn and Ge, spatially varying antiferromagnetic order has been observed [93]. The large spatial inhomogeneity is responsible for a coexistence of antiferromagnetic order and spin-Peierls state in the same sample. Spatially varying AFM order is visualized schematically in Fig. 7.7(c). Doping centers are present within the chain with distance L_0. A staggered magnetization is caused by the chain end spins and leads to an AFM order around the dopants. The magnetic moments are maximal around the doping sites and decay exponentially on the lengthscale of the correlation length.

In ESR experiments on pure $CuGeO_3$ a single resonance line is observed in the paramagnetic regime [105]. The line narrows as approaching the transition temperature. Below the transition temperature a single broad line is observed. Upon Zn doping magnetic order is established. Below the ordering temperature antiferromagnetic resonance modes are observed [cf. Fig. 7.7(a)] [91]. The ground state is magnetic but the spin-Peierls excitation remains [106]. Additionally, very complex ESR spectra were observed which were attributed to transitions originating from states within the gap [107]. For doping with magnetic Ni impurities, the AFM resonances are visible, but shifts of the ESR lines are observed which were attributed to a contribution from the single ion anisotropy of the Ni ions [108]. For Mg doping below 4% a coexistence of paramagnetic and antiferromagnetic phase could be measured directly with ESR [109].

The appearance of antiferromagnetic order upon doping was also reported for the Haldane system $PbNi_2V_2O_8$ [cf. Fig. 7.7(b)] [89, 92]. The AFM order is attributed to chain edge spin cutting the chains [90]. A coexistence of Haldane phase and AFM order has been observed with ESR for an intentional low doping with Mg in this compound [92]. Here the paramagnetic line prevails at low temperatures and additionally AFM resonance modes appear. Analogous to $CuGeO_3$, this is interpreted as a microscopic phase separation of antiferromagnetic order and spin-singlet state.

The presence of impurities as evidenced from the low temperature susceptibility and the observation of ESR signals attributed to different states supports a similar scenario in the system studied here. However, in contrast to these system the Ni-hybrid has not been doped intentionally. Eventually a disorder in the spin system originates from structural disorder in the crystal, resulting in chain lengths of different size and broken bonds giving rise to local magnetic states [cf. Fig. 7.7(c)].

ESR spectra were observed in Haldane systems, which were attributed to singlet-triplet transitions between the $S = 0$ ground state and the $S = 1$ triplet state in NENP [110, 95] and $PbNi_2V_2O_8$ [96]. These transitions are forbidden by the dipole selection rules as stated in equation (2.5) in Chapter 2. However, mixing between pure spin states is possible through exchange interactions or single ion anisotropy. Then the forbidden transitions can be observed in an ESR experiment. For the Ni-hybrid the absence of single ion anisotropy was found. Therefore it is likely that the mixing is too small to make an observation of the forbidden transitions possible. Indeed, no ESR lines were observed which could be attributed to singlet-triplet transitions.

Coming back to the frequency vs. magnetic field plot in Fig. 7.6: Resonances measured perpendicular to the chain above 249 GHz decrease in intensity but do not appear shifted from the paramagnetic line, when going to the low temperature regime. No additional peaks have been observed which can be attributed to the AFM resonances around these frequencies. The central line behaves as would be expected for a Haldane system. An impurity induced AFM order can be suppressed by the applied magnetic field [90], but no corresponding feature was observed in the magnetization measure-

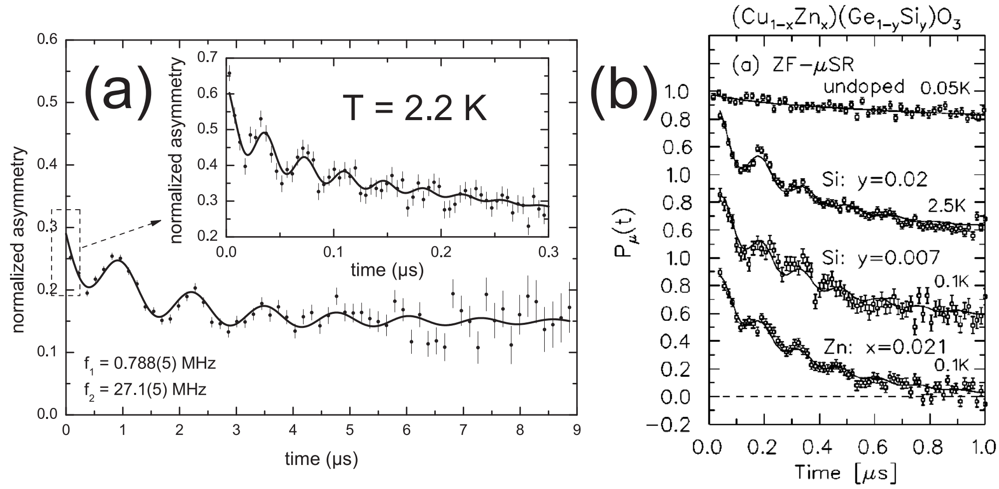

Figure 7.8: (a) Muon spin relaxation measurement at 2.2 K on powder sample of Ni-hybrid. Damped oscillation and additional damping is observed. (b) Muon spin relaxation of CuGeO$_3$ *from* [93].

ments on the Ni-hybrid. Since the single crystals used for this measurement are from a different batch than the other samples, the impurity concentration might be different in this individual sample.

7.4 Further Investigations

In order to further clarify the low temperature behavior, muon spin relaxation measurements [111] were conducted at the Paul-Scherrer-Institute (PSI), Switzerland by H. Maeter (TU Dresden) and H. Luetkens (PSI). In the measurement shown in Fig. 7.8(a) no external magnetic field was applied to the sample. Below temperatures of $T_N = 8$ K spontaneously a damped oscillation is observed. Such an oscillation results from the precession of the muon spins in static magnetic fields. Therefore this is a proof for the long range magnetic order at temperatures below $T_N = 8$ K. Two different oscillation frequencies are observed indicating at least two muon stopping sites. However the data cannot be well-described by considering only two static contributions to the muon spin relaxation. The damped oscillation is overlaid with another damping. The signal seen in μSR resembles that reported on Zn and Si doped spin-Peierls system CuGeO$_3$ [Fig. 7.8(b)]which was attributed to spatially varying magnetic order induced by impurities [93].

In conclusion, the μSR data observes long range magnetic order below 8 K with some unusual properties. Qualitatively it is in agreement with the ESR findings of the coexistence of long range antiferromagnetic order and the observation of a residual Haldane system.

7.5 Summary and Conclusion

The hybrid material $NiCl_3C_6H_5CH_2CH_2NH_3$ was studied with susceptibility, magnetization, ESR and μSR measurements. As evidenced by low temperature susceptibility measurements, impurities are present in the intentionally undoped Ni-hybrid. Magnetization shows a spin-flop transition around 3.5 T, pointing to an AFM order. This is supported by the susceptibility which becomes anisotropic below $T_N \approx 10$ K.

At low magnetic fields ESR measurements further support the antiferromagnetic order. Additionally, a paramagnetic line with decreasing intensity is still present below the ordering temperature, indicating a partly preserved low-dimensional spin system, eventually evolving to the Haldane ground state. This central line shifts in the internal field of the AFM. Above fields of about 7.5 T no signals corresponding to the AFM resonances are observed. The central line does not shift in field in agreement with the absence of significant internal fields. This possibly indicates the suppression of the AFM order by the magnetic field.

The scenario of coexistence between the two ground states is in agreement with muon-spin-relaxation measurements. An inter-chain coupling as the origin of the long-range magnetic ordering cannot be excluded from the data.

The Ni-hybrid is a promising material for studying competing interactions in a low-dimensional system. Although the coexistence of different states can be observed, its origin in the intentionally undoped sample remains unclear. Also, an eventual suppression of the AFM order by magnetic field remains an open question. This can be addressed by methods like NMR at different magnetic fields and nuclei at different sites in the structure. The excitation spectra for the Haldane gap and AFM excitations appear at different wave vectors. This can be investigated with inelastic neutron scattering

(INS). INS and NMR would therefore be powerful methods to obtain further insights into the magnetism of the Ni-hybrid.

CHAPTER 8

Summary

In this part, two one-dimensional spin chains with competing interactions were investigated with ESR and complimentary methods. The first material, Linarite, is a spin $S = 1/2$ chain based on Cu. A three-dimensional ordering takes place at around 2.8 K. In the system a significant magnetic anisotropy exists with the chain direction being the easy-axis. At temperatures above the ordering this is explained by the anisotropy of the g-factor alone. The static susceptibility is dominated by the spin susceptibility as determined by ESR and NMR shift. The extracted Curie-Weiss constant indicates a FM coupling, but significant AFM correlations become relevant at low temperatures. This is also seen in the broadening of the ESR linewidth with decreasing temperatures. A quantitative analysis of the ESR linewidth indicates the presence of interchain and interlayer correlations well above T_N. With the ordering taking place at 2.8 K the system is strongly frustrated on a temperature scale in agreement with the calculated coupling constants of FM NN $J_1 \approx -70\,\mathrm{K}$ and AFM NNN $J_2 \approx 27\,\mathrm{K}$.

The second material investigated is an anorganic-organic hybrid. It represents a spin $S = 1$ chain based on Ni. For such a system the ground state is proposed to be a non-magnetic singlet state with a Haldane gap to the excited triplet state. The ESR measurements in the paramagnetic regime show the absence of single-ion anisotropy, indicating an ideal realization of the Haldane scenario. In contrast to that, in susceptibility measurements an AFM magnetic ground state is observed for temperatures below $T \approx 8\,\mathrm{K}$.

Magnetization measurements reveal a spin-flop at magnetic fields around 3.5 T. Additionally, a low temperature Curie tail in the susceptibility proves the presence of impurities in the sample. At temperatures below 8 K ESR measurements at 93 GHz confirm the AFM order. Additionally, the paramagnetic line broadens, decreases in intensity, but persists down to very low temperatures. This indicates the coexistence of the Haldane behavior and antiferromagnetic order. The coexistence between singlet quantum ground state and ordered state has been shown before in the doped spin-Peierls $S = 1/2$ chain $CuGeO_3$ and in the doped Haldane $S = 1$ chain $PbNi_2V_2O_8$. It is attributed to spatially varying magnetic order due to impurities. μSR measurements confirm the long range magnetic order in the Ni-hybrid. An unusual relaxation behavior observed is similar to that of doped $CuGeO_3$, supporting the possible coexistence of both states. In agreement with the absence of single ion anisotropy no singlet triplet transitions are observed in the low temperature ESR measurements.

Both materials investigated show competing magnetic behavior. They are promising systems for the understanding of low-dimensional spin physics and for the realization of systems with externally tunable ground states.

Part III

SiGe Nanostructures

9 Motivation

10 SiGe Semiconductor Nanostructures

10.1 Background 107
10.2 Sample Structure and Characterization 114

11 Modelling of SiGe/Si Heterostructures

11.1 Program Structure 120
11.2 Implementation of Si/Ge System 121
11.3 Results 123
11.4 Discussion 130
11.5 Summary 132

12 ESR Experiments on Si/SiGe Quantum Dots

12.1 ESR on Si Structures 135
12.2 Experimental Results 137
12.3 Discussion 148
12.4 Summary 156

13 Summary and Outlook

CHAPTER 9

Motivation

The material systems based on Si are technologically well-established. In contrast to III-V materials the spin-orbit coupling in group IV semiconductors is fairly weak [112]. This enables long spin lifetimes and coherence times offering possibilities in spintronics applications and devices. Another limiting factor for relaxation and coherence times in III-V, namely GaAs, semiconductor structures is the hyperfine interaction with the nuclear spins [113]. In Si and Ge, this effect is much smaller and can be further reduced by isotopic purification, enabling even longer dephasing times [33, 114]. Si and Ge are indirect semiconductors, so optical methods are not best suited to study their spin states. Among other techniques, such as optical and electrical approaches, ESR has emerged as a reliable and well-suited method to investigate spin states in semiconductors. ESR provides direct access to static and dynamics of spin ensembles. In particular, information about the g-factor and the dephasing and relaxation times can be extracted from continuous wave ESR measurements.

Traditionally ESR on Si based systems is concerned with the physics of the localized electron spin on donor impurities and delocalized electrons in the conduction band. ESR of bulk Ge and especially Si have been studied extensively in the past [33, 115, 116, 117, 118, 119]. Electrons contributing to an ESR signal can be localized on donors (e.g. phosphorus) embedded in Si or Ge [33, 117]. In heavily n-doped bulk Si the g-factor is isotropic with $g = 1.99875$ [33] due to the singlet orbital ground state. In Ge an isotropic g-

factor of $g = 1.56$ is found [116]. However, if a uniaxial compressive strain is induced in the Si, higher states admix and the effective g-factor is described by an axial symmetry tensor [119]. Quantum operations involving electron and nuclear spins of donors in Si have been reported recently [120].

An alternative way to localize electrons within semiconductor heterostructures is the creation of SiGe/Si self-assembled quantum dots [121]. These quantum dots are self-assembling structures grown with molecular beam epitaxy. The spatial positioning of quantum dots can be controlled laterally and vertically [122]. With potentially different timescales for the spin states than those of donor electrons, quantum dots can facilitate new controllable building blocks for more diverse and complex spintronic devices. Different spintronic and quantum computational schemes have been proposed for SiGe quantum dots [123, 124]. Recent advances in strained layer epitaxial growth have allowed the fabrication of defect-free heterostructures, initiating novel investigations into low-dimensional physics. For instance it has been shown that in SiGe based heterostructures a two-dimensional electron gas (2DEG) can be formed in strained Si channels [125, 126]. ESR investigations pointed out that in these systems the g-factor and the linewidth is anisotropic as a result of the Bychkov-Rashba-effect [127].

More recently, it has been shown that for SiGe nanostructures coherently embedded in Si the band-edge alignment is a type II alignment [128]. This leads to localized confining potential for electrons in the Si matrix [129, 121]. As a consequence, self-assembled SiGe islands can assure precise control and an external addressability to the localized electron spin states. In addition, the introduction of spin-resonance transistors based on SiGe nanostructures into the main stream Si technology opens up new degrees of freedom via band structure and strain engineering. Despite the large interest SiGe nanostructures have attracted, ESR investigations on such a system are still scarce. To our knowledge there are only two experimental works reported in Refs. [130, 131], whose results and their fundamental interpretation differ significantly. This makes a detailed and systematic study necessary to understand the behavior of the electronic states of SiGe nanostructures.

In Chapter 10 the materials system Si/Ge is introduced. The characterization of the samples investigated is presented. Based on this, the electronic structure modeling is given in Chapter 11. In Chapter 12 the ESR results are presented and all results are discussed in context. This part of the thesis is based on the publications [132, 133, 134].

CHAPTER 10

SiGe Semiconductor Nanostructures

10.1 Background

10.1.1 Silicon and Germanium

Silicon and Germanium are group IV semiconductors. They are indirect gap semiconductors. The transition of an electron from the valence band to the conduction band requires not only additional energy but also a change in momentum of the electron. Fig. 10.1 shows a section of the energy bands $E(k)$ of Silicon. The valence band maximum consists of two degenerate bands at the Γ-point, the center of the Brillouin zone at [000]. They have small and large curvatures and are therefore referred to as heavy and light hole bands, respectively. A third band is separated from them by an energy of 44 meV due to spin-orbit coupling. The latter is called split-off-band. The conduction band minimum is located along [100] close to the Δ-point. The energy gap is about 1.11 eV between valence band and conduction band. Because of the symmetry of the fcc lattice there are six equivalent conduction band minima. Due to the relatively small number of electrons in the conduction band (and holes in the valence bands), the dispersion relation at the extrema can be approximated by a harmonic potential in the limit of the effective mass theory [13]. The diagonal form of the energy dispersion

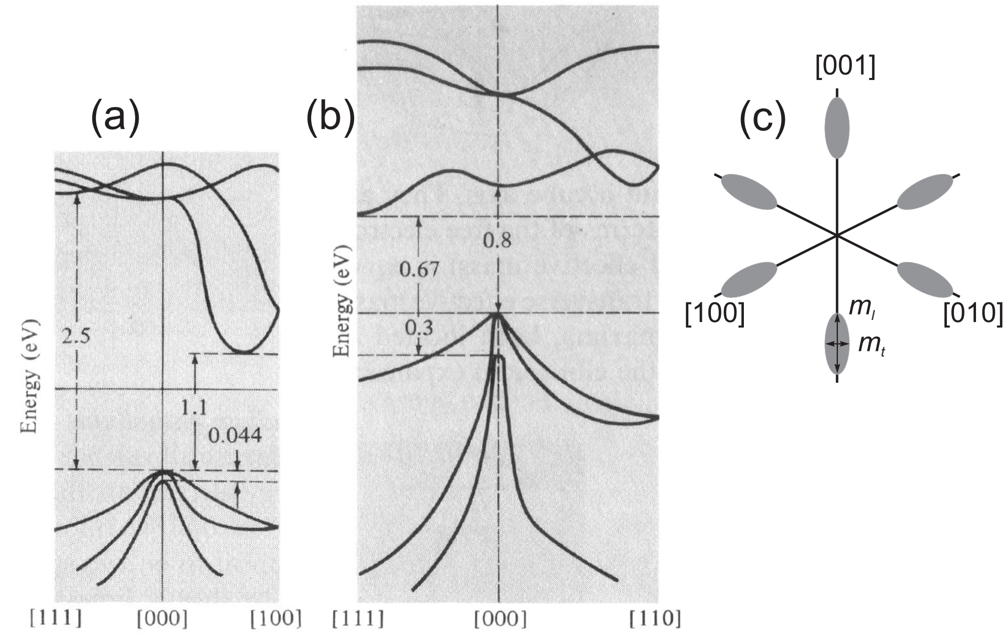

Figure 10.1: (a) Section of Si bandstructure. Valence band maximum is at the Γ-point [000]. Conduction band minimum along [100] close to the Δ-point. (b) Section of Ge bandstructure. Valence band maximum is found at the Γ-point as well. The conduction band minimum is located at [111]. *Figs. (a) (b) from* [13, 135] (c) Si Δ conduction band valleys.

for electrons is

$$\mathrm{E}(\mathbf{k}) = \mathrm{E}_c + \hbar^2\left(\frac{k_x^2 + k_y^2}{2m_t} + \frac{k_z^2}{2m_l}\right) \tag{10.1}$$

The surface of constant energy are six ellipsoids defined by the longitudinal effective mass $m_l = 0.98m_0$ along the (100), (010) and (001) directions and the transverse effective mass $m_t = 0.19m_0$ perpendicular to it [Fig. 10.1(c)]. m_0 denotes the free electron mass. Those ellipsoids of constant energy are often referred to in literature as "conduction band valleys". Correspondingly the term Δ-band is used.

For Ge the valence band maximum occurs at the Γ-point as well, where heavy and light hole bands are degenerate in energy while a third band is displaced in energy by about 290 meV. The conduction band minima occur along [111] at the L-point (Fig. 10.1). The indirect bandgap from Γ to L is with $\mathrm{E}_{\mathrm{Ge}} = 0.67$ eV smaller than in Si.

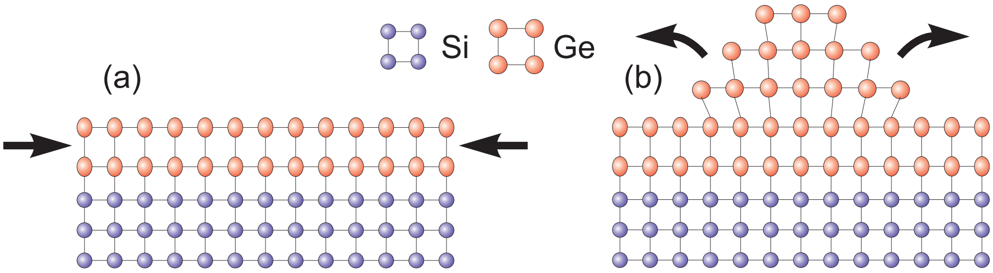

Figure 10.2: Schematic growth of Ge island on Si substrate. (a) Ge wetting layer is tetragonally deformed: It is compressed in the plane and expands perpendicular to it. (b) In Ge islands strain relaxation takes place.

Combining different semiconductor materials, single crystalline heterostructures can be realized which show diverse electronic, optical and magnetic properties.

10.1.2 Epitaxial Growth of SiGe Heterostructures

The technology of molecular beam epitaxy (MBE) is able to deposit materials with mono-atomic layer (monolayer - ML) precision. With this it is possible to combine different materials to assemble so-called epitaxial heterostructures. In the epitaxial structures the lattice structure is continued over the boundary of the different materials, effectively preserving the single crystallinity. Silicon crystallizes in the diamond structure with a lattice constant at room temperature of about 5.431 Å [136]. Germanium exhibits the same structure with a slightly larger lattice constant of 5.657 Å [136]. This small difference of about 4.2% in the lattice constants and the difference in the bandgap makes Si and Ge very good systems for the creation of heterostructures with the MBE technique.

The growth of epitaxial layers of different materials leads to the formation of self-assembled islands. Island formation is driven by the strain within the material system, but minimization of surface energy also plays a role [121]. Let us consider a simplified way for the growth of SiGe islands: A single layer of Ge is grown epitaxially on a atomically flat Si surface. Each Ge atom adapts to the Si atom below it to keep the bond structure [see Fig. 10.2(a)]. With that the lattice constant of Si is preserved in the Ge layer in-plane. This means that the Ge atoms are displaced laterally compared to their original position in a pure Ge crystal. This displacement corresponds to a biaxial compressive strain in the lateral direction of the epitaxial Ge layer. In order to conserve the volume of the Ge unit cell, the Ge layer has to expand in the direction perpendicular to the plane. Such a monolayer is called pseudomorphic layer.

The strain increases with the thickness of the pseudomorphic layer. There exists a critical thickness t_c, above which new monolayers do not grow pseudomorphically. During the MBE growth the system is not in thermal equilibrium. This way thicknesses larger than the critical thickness can eventually be realized. Then the critical thickness of the pseudomorphic layer depends on the growth parameters, e.g. growth temperature and Ge content x [137]. Above t_c a strain relaxation is realized through an increased roughness of the layer which leads to nucleation sites for island formation or a flat dislocated layer [138].

Ge islands can grow defect free on Si(001) in the so-called Stranski-Krastanow growth mode [139, 140]. This means the SiGe islands form on top of the pseudomorphic layer, not directly at the Si. For the Stranski-Krastanow growth the pseudomorphic layer is called wetting layer, indicating the very thin, complete coverage of the Si surface. In three-dimensional Ge islands the strain relaxation can be realized without creating dislocations. From layer to layer Ge atoms are slightly displaced laterally and an elastic strain relaxation takes place until the original lattice constant of Ge is reached [see Fig. 10.2(b)].

One important effect in the growth of self-assembled SiGe islands beyond the simple strain model, is the intermixing of Si into the Ge islands [141]. At typical growth temperatures of 500-850°C a significant solid state diffusion between Si and Ge can take place. So even though pure Ge is deposited on top of a Si substrate, the island is found to be an alloy of $Si_{(1-x)}Ge_x$. The Ge concentration x is not necessarily constant throughout the islands, but can have more complex profiles [141]. By changing the MBE growth parameters (e.g. growth temperature) the intermixing as well as the morphology of the islands can be changed significantly [142, 143]. Among the different forms of SiGe islands are those characterized as *hut clusters*, *pyramids*, *domes*, *barns* and *superdomes* [144, 145, 146, 147, 148]. Also, within these classes, there can be differences in the actual alloy composition, the strain and the corresponding electronic structure. Additionally, the overgrowth

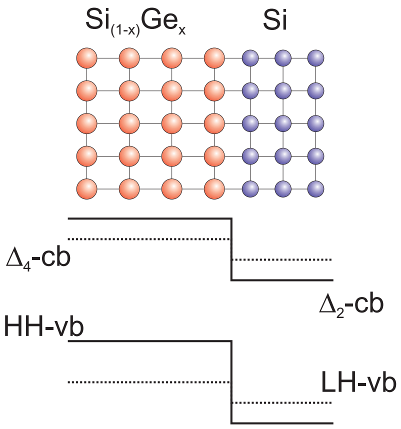

Figure 10.4: Type II band alignment between $Si_{(1-x)}Ge_x$ and Si. In Si the lowest conduction band is the Δ_2-band. The highest valence band is the light hole band (LH). In $Si_{(1-x)}Ge_x$ the heavy hole (HH) band becomes the highest in energy, while the Δ_4 is lowered. Electrons are confined in the Δ_2-band in Si, while holes are confined in the HH-band in SiGe. Confined hole and electron are spatially separated.

of the SiGe islands with Si can change the morphology of the islands significantly [149, 150]. The SiGe islands investigated in this work are domes overgrown with Si. The characterization will be discussed in Section 10.2.

For now let us consider only the idealized overgrowth of the SiGe islands with Si, neglecting intermixing. On top of the dot the $Si_{(1-x)}Ge_x$ is relaxed completely and its lattice constant is given in the first approximation by a linear interpolation between the lattice constants of Si and Ge as a function of alloy concentration x [151].

$$a_{Si_{(1-x)}Ge_{(x)}} = (1-x)\cdot a_{Si} + x\cdot a_{Ge} \tag{10.2}$$

Deviations from this behavior through non-linear bowing effects [152] can be considered in quantitative calculations.

When a SiGe island is overgrown with Si the strain process takes place in the Si matrix on top of the dot, meaning that now the Si adapts to the SiGe lattice constant. This results in a biaxially tensile strained Si region at the apex of the SiGe island. The island induces a biaxial tensile strain also below the island. At the base of the island the Si is subject to biaxial compressive strain.

10.1.3 Strain

Numerical calculations based on the envelope function approach or finite element calculations can be performed to gain quantitative analysis of the properties of SiGe heterostructures. For this quantitative models for the description of strain and bandstructures are necessary. The strain in a material due to external stress depends on the elastic constants of the material. For a cubic crystal the stress tensor is related to the strain tensor as:

$$\begin{pmatrix} \sigma_{xx} \\ \sigma_{yy} \\ \sigma_{zz} \\ \sigma_{xy} \\ \sigma_{xz} \\ \sigma_{yz} \end{pmatrix} = \begin{pmatrix} C_{11} & C_{12} & C_{12} & & & \\ C_{12} & C_{11} & C_{12} & & & \\ C_{12} & C_{12} & C_{11} & & & \\ & & & 2C_{44} & & \\ & & & & 2C_{44} & \\ & & & & & 2C_{44} \end{pmatrix} \cdot \begin{pmatrix} \epsilon_{xx} \\ \epsilon_{yy} \\ \epsilon_{zz} \\ \epsilon_{xy} \\ \epsilon_{xz} \\ \epsilon_{yz} \end{pmatrix} \tag{10.3}$$

where the σ_{ij} and ϵ_{ij} are the stress and strain components respectively and C_{ij} are the elasticity constants.

For the growth of a pseudomorphic layer on a substrate the strain parallel to the interface is biaxial and given by:

$$\epsilon_{\parallel} = \epsilon_{xx} = \epsilon_{yy} \tag{10.4}$$

Biaxial strain can be represented by a hydrostatic and an uniaxial strain component. Perpendicular to the interface along the (001)growth direction the uniaxial strain is:

$$\epsilon_{\perp} = -2C_{12}/C_{11}\epsilon_{\parallel} = -D\epsilon_{\parallel} = \epsilon_{zz} \tag{10.5}$$

The strain can also be defined in terms of the lattice constants as

$$\epsilon_{\parallel} = \frac{a_0}{a} - 1 \qquad \epsilon_{\perp} = D\left(1 - \frac{a_0}{a}\right) \tag{10.6}$$

where a_0 is the lattice constant of the substrate and a the equilibrium lattice constant of the layer material [128]. The quantitative modeling of the strain profiles for three-dimensional structures as performed with the program nextnano^3 is discussed in Chapter 11. By defining the strain in the dependence of the lattice constants, intermixing profiles can be included in calculations easily.

10.1.4 Band Deformation

The difference in the band structure between Si and Ge makes it possible to create heterostructures in which the electronic structure can be designed in such a way that quantum mechanical confinement is realized.

In addition to the band offsets due to the chemical potential, the strain between the different materials influences the band structure significantly. Imagine a Ge island embedded in Si: At the interface between Si and Ge band offsets for the conduction bands and the valence bands are present. On the absolute energy scale, the lowest conduction band is the Δ-band in Si, while the highest valence band is the heavy hole band in Ge. The strong misalignment between the energy bands creates a boundary at the interface. Because of that, holes are confined within the Ge island. Since the lowest electron states are in the Δ-band of Si, electrons are not confined within the Ge island, but are located in the Si. This band-alignment is called type II, in contrast to the type I alignment in many III-V semiconductors where electrons and holes can be localized within the island. The type II band alignment was experimentally confirmed in strained layers of Si/SiGe [125] and Ge islands embedded in Si [121]. The terms SiGe island and SiGe quantum dot refer to the same object.

The biaxial strain component can be decomposed into a hydrostatic and a uniaxial component. The hydrostatic strain shifts the average conduction and valence energy levels according to

$$\Delta E_h^{c/v} = a^{c/v}(2\epsilon_\parallel + \epsilon_\perp) \tag{10.7}$$

where a^c and a^v are the absolute deformation potentials for the conduction and valence band, respectively. Uniaxial strain splits the six equivalent Δ-valleys. For the (001) growth direction, the Δ-band splits into four in-plane valleys $\Delta_4 = \Delta_{xy}$ and the two valleys along the growth direction $\Delta_2 = \Delta_z$.

$$\Delta E_c^\Delta = \begin{cases} +\frac{2}{3}\Xi_u^\Delta(\epsilon_\perp - \epsilon_\parallel) & \text{for the } \Delta_2\text{−band} \\ \\ -\frac{1}{3}\Xi_u^\Delta(\epsilon_\perp - \epsilon_\parallel) & \text{for the } \Delta_4\text{−band} \end{cases} \tag{10.8}$$

where Ξ_u^Δ is the band deformation potential for the Δ-band. The initial deformation potentials were calculated by van de Walle [153]. For the modeling the deformation potentials can be implemented in a database and band offsets are calculated accordingly.

As mentioned earlier in real structures, one does not deal with pure Ge islands, but usually with island of a $\text{Si}_{(1-x)}\text{Ge}_x$ alloy on top of Si. For Ge fractions up to $x \approx 0.85$ the band-structure is Si-like with the lowest electron

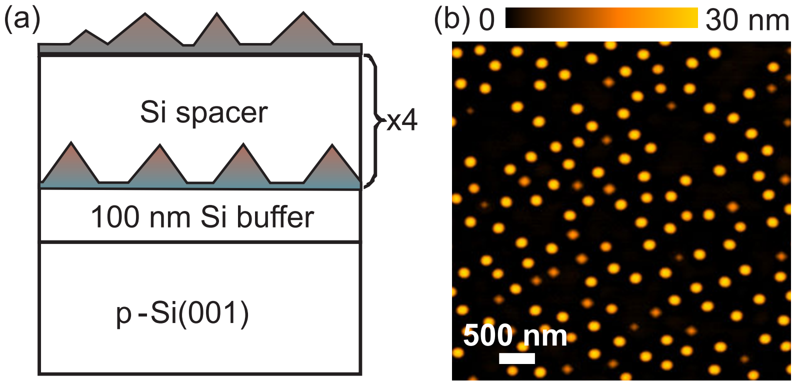

Figure 10.5: (a) Schematic sample structure. Si spacers are 20 nm, 70 nm and 100 nm for the individual samples. (b) AFM top view of sample with 70 nm spacer grown at 700°C. *AFM measurement: F. Pezzoli*

band being the Δ-band. Then a crossing of the L-band with the Δ-band occurs and for higher Ge content the L-band is lower in energy [154].

10.2 Sample Structure and Characterization

Two sets of SiGe/Si multilayers were grown by means of solid source molecular beam epitaxy (MBE). After the deposition of a 100 nm-thick Si buffer on p-Si(001) substrates, 4-fold stacks of 6.5 monolayers (ML) and 8.5 ML of Ge separated by Si spacers were deposited at 600 °C and 700 °C, respectively. For each sample the thickness of the Si spacers was constant and equal to 20, 70 or 100 nm. All the structures were capped with the same amount of Ge for further surface morphology investigations. A schematic for the sample structure is shown in Fig. 10.5(a). It should be noted that the samples are not intentionally doped, nevertheless we estimated a residual MBE background doping of about $2.3 \cdot 10^{16}\,\mathrm{cm}^{-3}$ (n-type). The most likely impurities present in the system are P donors since the MBE chamber is equipped with a phosphorus doping cell. As a consequence, to rule out spurious effects and to correctly assign the spectral ESR features the following reference structures were grown in addition to the aforementioned samples: (i) A p-doped Si(001) substrate overgrown with 100 nm of Si buffer. (ii) Substrate and buffer with Ge wetting layers (WL) grown at 600 °C, i.e. SiGe planar layers which form during the early stage of Ge deposition and always accompany the dots, separated by 20 nm of Si as in one of the multilayers.

Since no dots are present, the Si can be considered as unstrained. (iii) A Si substrate overgrown with Si where the Ge layers were replaced by growth interruptions with duration equal to the time required to deposit Ge in the samples with dots.

The samples were characterized with Atomic Force Microscopy (AFM) and Transmission Electron Microscopy (TEM). Based on the gained structural information, single-band calculations were implemented to study the electronic structure of the heterostructures, which will be discussed in detail in Chapter 11. Samples were grown at the MPI for Solid State Research Stuttgart by M. Stoffel and F. Pezzoli. AFM measurements were performed by F. Pezzoli. The TEM analysis was conducted by Ch. Deneke.

When islands are overgrown with Si their morphology can change significantly. However, the AFM analysis of the topmost layer can provide information of the vertical alignment between the different layers of SiGe islands. Figure 10.6 shows an AFM image and a statistical analysis of it for a sample grown at 600 °C with a 70 nm spacing. The size distribution of islands is fairly narrow and indicates a single type of island morphology (monomodal). By varying the spacing between quantum dot layers the elastic coupling between layers changes [155]. The monomodal distribution of islands indicates that no vertical alignment from one quantum dot layer to the next occurs. Therefore the quantum dots and the confining potential in the Si induced by them can be regarded as isolated. This also holds for the sample with a spacing of 100 nm grown at 600 °C and 700 °C. When decreasing the spacing between the dots, buried dots act, through the strain field, as favorable sites for the formation of dots in the higher layers [156, 157, 158]. Because of this there will be a change in intermixing and size between dots in different layers [155, 121]. In general, intermixing and sizes are larger for dots grown at higher temperatures. Fig. 10.5(b) shows an AFM image of a sample grown at 700°C with a spacing of 70 nm. Different sizes and shapes of dots are visible. This is in contrast to dots grown at 600 °C with 70 nm spacer which still show a monomodal distribution. Samples of both growth temperatures with 20 nm Si spacer show a widened distribution.

This analysis is confirmed by TEM. In Fig. 10.7 TEM pictures of samples with 70 nm Si spacer grown at (a) 600 °C and (b) 700 °C are shown. A complete vertical alignment of dots takes place only for the sample grown at 700 °C. In the sample grown at 600 °C vertical alignment can take place, but

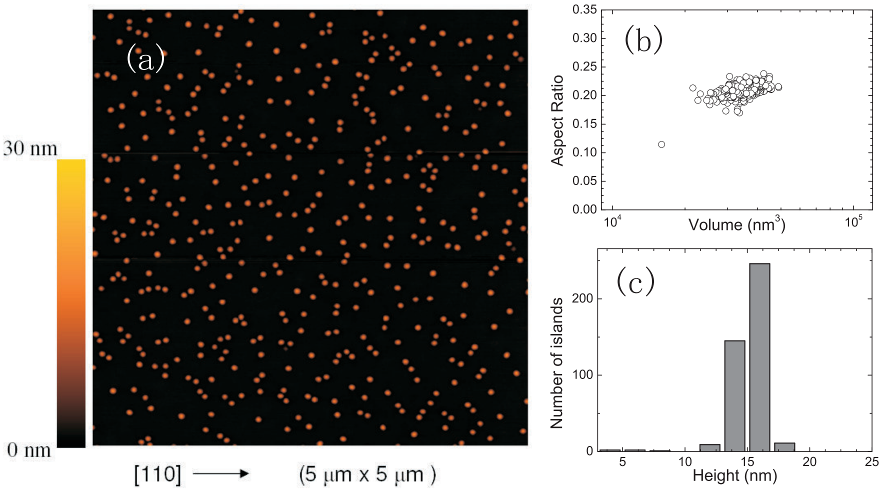

Figure 10.6: (a) AFM image of the top layer; (b) aspect ratio (defined as height to base ratio) as a function of island volume; (c) Histogram of the island heights *AFM measurement: F. Pezzoli*

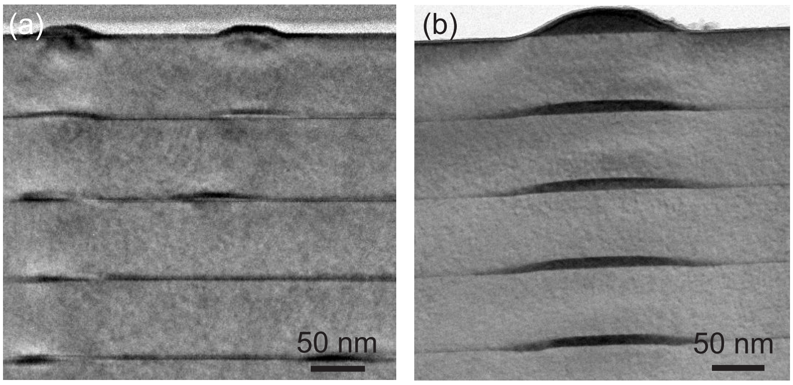

Figure 10.7: TEM of sample with 70 nm spacer grown at (a) 600°C and (b) 700°C. Dots are much smaller in samples grown at lower temperatures. *TEM measurement: Ch. Deneke*

dot formation also occurs spontaneously in higher layers. The distance between the quantum dots in the vertical direction of more than 50 nm is still too large for an electronic coupling to occur (see next chapter). The buried dots in the individual samples are similar in size and shape. The size difference for the different growth temperatures is evident from the TEM images (Fig. 10.7). When comparing buried dots with dots of the topmost layer the modified shape is clearly visible. This is more so in the structures grown at 700 °C [Fig. 10.7(b)]. The overgrown dots are much shallower and wider. The Si overgrowth flattens and compresses the dots. This effect is reduced in the samples grown at 600 °C. This results in a difference in size of about 200 nm base diameter for dots in the 700 °C samples, as compared to 80 nm base diameters for dots in the 600 °C samples.

CHAPTER 11

Modelling of SiGe/Si Heterostructures

The experimentally investigated Si/Ge heterostructures consist of multiple layers of SiGe/Si quantum dots with about 10^9 dots cm^{-2}. Quantum dots have heights of up to 20 nm and base diameters of up to 200 nm. To perform ab-initio calculations on strain and electronic structure of even a single quantum dot of that size would require an extensive computational effort. Because of this the program nextnano^3 [159] was chosen to perform simulations of the heterostructure systems. The program is based on the envelope function approach and allows the definition of a device or heterostructure geometry consisting of multiple materials [160]. Strain and electronic structure can be calculated. Self-consistent solutions of single band Schrödinger-equations allow to investigate the quantum mechanical effects. The numerical calculations are run on a desktop PC.

In this chapter an overview of the program nextnano^3 is given. The program structure is described. Computational methods themselves are not discussed, but the reader is pointed to the more detailed documentation reported in [159, 160, 161, 162, 163, 164] and references therein. Material parameters as well as computational parameters chosen for the calculations of Si/Ge heterostructures are discussed. Finally the results for single dots and multiple SiGe/Si quantum dots are presented and discussed in the context of the experimental data.

11.1 Program Structure

The program nextnano^3 uses an input file in which the user can define the system of interest and the calculation parameters. For this the geometry of the heterostructure has to be specified. The geometry consists of several *regions*, which are characterized by their coordinates and their geometric shape. By combining different geometric forms realistic structures can be implemented in the calculations. The basic forms well-suited to describe the experimentally investigated structures are dome-like (*semiellipsoid*) or *pyramid* shapes for the SiGe islands and rectangular (*cuboid*) shapes, mainly for the regions around them. When building the structure an overlap between consecutive regions can sometimes not be avoided. By assigning different *priorities* the region with lower priority is suppressed only in the overlap. With this a consistent structure is created.

Every region is assigned a *material*. The parameters for any specific material include structural parameters like lattice constants and elastic constants as well as electronic parameters like band energies and effective masses. The band energies are given with respect to a reference energy in order to compensate for band offsets of different material systems [162]. In addition to the bulk materials alloys like $\mathrm{Si}_{(1-x)}\mathrm{Ge}_x$ are also implemented. The Ge content x can be constant or have a linear or Gaussian distribution within an assigned region. The material parameters are read-in from a separate database. The material parameters used for the calculations of the SiGe heterostructures correspond to the nextano^3 database as of [165].

In order to perform the different calculations the real space geometry, in which the heterostructure is built is overlaid with a grid. The grid point positions are defined in the input file along the three cartesian coordinates (x, y, z) of the structure. To every physical grid point physical parameters are allocated and the actual calculations are peformed. On intersections between different regions physical grid points have to be present. In order to deal with discontinuities (e.g. in the density) on interfaces multiple points are created at the same position, but their allocated values depend on the direction from which the point is approached. In addition to the physical grid there is also the material grid. The material grid points are placed in between the physical grid points and are assigned the material information.

In a similar way to material regions, doping regions can be implemented.

The type of dopant as n- or p-type is defined, their ionization energies, the dopant concentration and the doping profile can be given for any specific region.

Contact regions can also be specified. This allows a voltage to be applied to the structure through ohmic or Schottky contacts. Additionally, von-Neumann or Dirichlet boundary conditions for the electric potential can be applied.

For regions of the structure where quantum mechanical effects become important *quantum regions* can be defined. In those regions different models can be applied to calculate the electronic structure, electronic densities as well as eigenvalues and eigenstates of bound states. Quantum regions must not overlap but can extend over different materials. Therefore it is possible to calculate properties on the interface of the SiGe/Si quantum dots quantum mechanically.

11.2 Implementation of Si/Ge System

For any calculation a consistent heterostructure has to be created. As initially the different materials are combined only as geometric forms, discontinuities of strain, charge densities and mismatch in the electronic structure are present at the interfaces between them. At first the strain of the heterostructure is calculated. For this a reference material is specified in the input file. This usually corresponds to the unstrained substrate material, which is Si for all structures modeled in this work. The growth direction of the structure is defined as the z-axis. Upon consideration of the alloy concentration and profile, the displacement for each material point is then calculated with respect to the unstrained Si.

The effect of strain on the bandstructure was discussed in more detail in Section 10.1.2 for the SiGe system. The calculations in nextnano^3 are based on the calculations by van de Walle who developed the well-established model for the shift of energies and splitting of bands due to the strain [128, 153]. The lowest lying band edges are the Δ-bands, which shift and are split in energy in the presence of biaxial strain into the two-fold degenerate Δ_2- and the four-fold degenerate Δ_4-bands.

Calculations of the electronic structure of SiGe systems with the 8x8 k.p. method are limited to electrons at the Γ-point [161]. Since the relevant (lowest lying) states are in the Δ-band, the calculations were carried out with the effective mass method. In the *quantum regions* the quantum mechanical electronic density is calculated by solving single-band Schrödinger equations, one for the Δ_2- and two for the Δ_4-bands.

All calculations were performed for a system in three dimensions. The z-direction corresponds to the (001) growth direction. Most calculations were performed on a cube with 300 nm edge length, but simulation spaces with up to 500 nm edge length were implemented. Periodic boundary conditions for the strain calculations were chosen. For arrangements of single dots and vertically stacked dots parameters along x- and y-direction were chosen centro symmetrically from the simulation midpoint, in contrast to the situation where dots are arranged laterally.

For solving the eigenvalue problem of the Schrödinger equation different numerical methods based on packages implemented in nextnano^3 can be specified. For the calculations reported here the *ARPACK* package was used [166]. Most of the time the calculation of five additional eigenvalues was requested to improve convergence.

Most calculations were performed with isotropic effective masses. Only when calculating eigenstates and wave functions in magnetic fields are anisotropic effective masses relevant and were included. Strain changes the electron effective masses slightly as described in [167]. This cannot be considered in the program, but in the investigated structures the effect is less than 10% for m_l and less than 5% for m_t.

For the calculations usually a homogenous doping with $n = 2.3 \cdot 10^{16}\,\mathrm{cm}^{-3}$ and $E = -45\,\mathrm{meV}$ was defined. This concentration corresponds to the measured residual doping as described in Section 10.2 with the most likely impurities present being phosphorus donors. The P donor ionization energy in unstrained Si is $E = -45\,\mathrm{meV}$.

ESR experiments were performed mainly at temperatures around 4 K. A temperature of 4 K was specified in the calculations. This has an effect on the bandgap through defined Varshni parameters [168]. In the calculations the valence band is kept constant and the absolute energy of the conduction band is changed. The lattice constants are dependent of temperature as well. The change of the lattice parameters with temperature is defined by temperature coefficients Δa (nm/K). For Si and Ge these are different by about $\Delta a(Si)/\Delta a(Ge) \approx 0.3$. This results in an effective decreasing of the strain at the (Si)Ge/Si interface with decreasing temperature. However, the effect on the strain for 4 K as compared to room temperature is only about 0.2% for a pure Ge/Si interface. For the $\mathrm{Si}_{(1-x)}\mathrm{Ge}_x$ alloy the parameters are approximated linear according to x.

11.3 Results

The SiGe/Si heterostructures investigated experimentally consist of four layers of SiGe/Si quantum dots. On top there is another layer of SiGe islands. For the calculations, the dot shapes extracted from TEM analysis and AFM measurements are approximated by semiparabola. Islands for structures grown at different temperatures differ significantly in size. For the dots grown at 600°C an average base diameters around 80 nm was estimated. Dots grown at 700°C are typically around 200 nm. Heights for both are about 10 nm. At higher temperatures the upper part of a SiGe dome can get cut by the overgrowth of Si. The dots appear flattened. By placing an additional Si block with a higher priority, this shape can be implemented. However, since the large semiparabola are very flat already, the influence on band and confining energies is negligible. Therefore all calculations reported here are on semiparabolic quantum dots between 200 nm and 80 nm base diameter.

Before presenting calculations on multiple stacked quantum dots let us discuss the strain, conduction band potential and energy states of single quantum dots.

11.3.1 Single Quantum Dot

The uniaxial strain ($\epsilon_{zz}-\epsilon_{xx}$) is shown in Fig. 11.2 exemplarily for a $\mathrm{Si}_{(1-x)}\mathrm{Ge}_x$ semiparabolic quantum dot with a Ge content of $x = 0.36$. This contour plot shows the strain in the xz-plane as a cut through the center of the dot at $y_0 = 150$ nm. The quantum dot is placed on a Ge wetting layer, which is clearly visible in the figure as a horizontal line along x. At the base side around the island, the uniaxial strain is positive, corresponding to a compressively strained region. On top of the dot, as well as at the bottom, the uniaxial

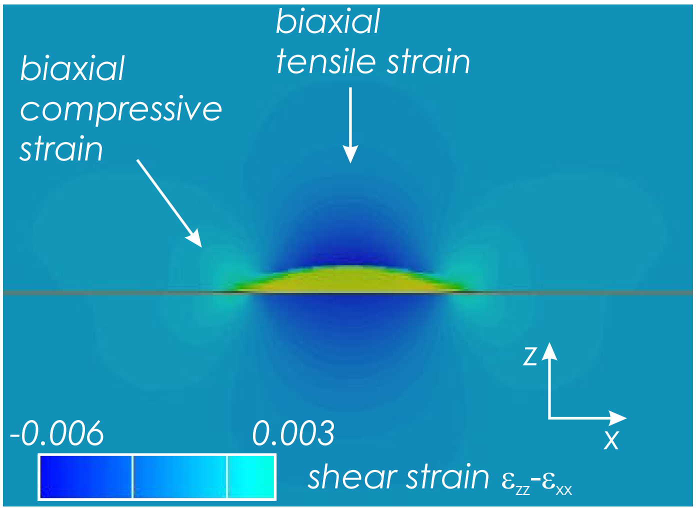

Figure 11.2: Uniaxial strain profile $\epsilon_{zz} - \epsilon_{xx}$ of $\mathrm{Si}_{(1-x)}\mathrm{Ge}_x$ semiparabolic quantum dot with a base diameter of 80 nm, height 10 nm and constant Ge content $x = 0.36$. The biaxial compressive strained region in Si around the base and the tensile strained region above and below the islands are visible.

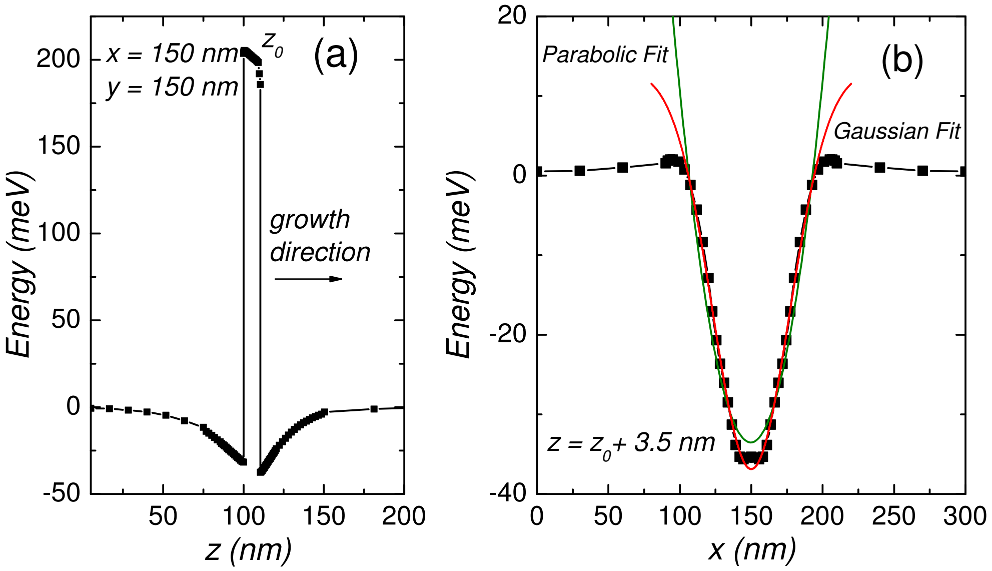

Figure 11.3: Δ_2 conduction band profile for a semiparabolic quantum dot with height $h = 10$ nm, base diameter $d = 80$ nm and Ge content of 36 %. $E = 0$ corresponds to the unstrained conduction band in Si. (a) In z-direction the conduction band potential shows a sharp barrier for the penetration of the electron wave functions at the SiGe/Si interface at z_0 and a smooth increase away from it. (b) In the xy-plane the confining potential can be approximated by a parabolic or Gaussian form.

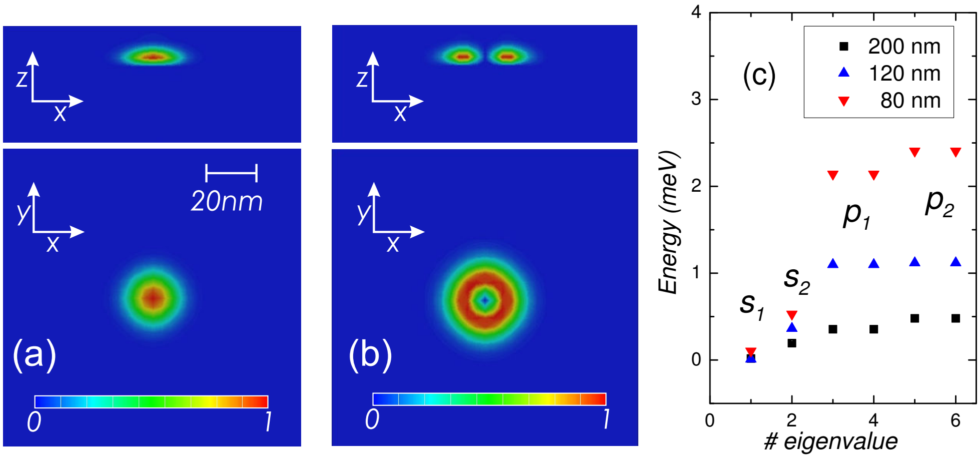

Figure 11.4: (a) s-like-state and (b) p-like-state normalized probability wave functions for a magnetic field $H = 3400$ Oe along z-direction. (c) Eigenvalues for dots of different base diameters relative to the eigenvalue s_1 close to $E = 0$. s_1 corresponds to the s-like state on top of the SiGe island, s_2 to the one below. The same applies to the p_1- and p_2-states.

strain is negative which corresponds to tensile strained regions. The tensile strain is maximal at the apex of the dot. The effect of strain on the bandstructure is given by equation (10.8). Fig. 11.3 shows a Δ_2-conduction band profile of the same semiparabolic quantum dot with 80 nm base diameter. In order to better see the potential variations the two subfigures represent cuts at (a) $x = y = 150$ nm and (b) $y = 150$ nm, $z = 113.5$ nm, with the SiGe/Si top boundary located at $x_0 = y_0 = 150$ nm, $z = z_0 = 110$ nm. Looking at the single dot structure the potential in z-direction (growth direction) shows a sharp edge at the boundary between SiGe and Si. From there it increases smoothly until the conduction band energy reaches that of the unstrained Si. At the boundary the potential is similar to a single interface of a modulation doped quantum well. In the perpendicular plane (b) the confining potential is close to a Gaussian or parabolic form. This behavior is the same below the SiGe islands, but the potential is not as deep.

The aspect ratio of a quantum dot defined as height/base diameter is relevant for the strain and with that the band deformation. Since the height is roughly the same for all dots with $h \approx 10$ nm, the aspect ratio is determined primarily by the size of the base and dots are classified according to their base diameters. The base diameters are around 80 nm and 200 nm for samples grown at 600°C and 700°C, respectively. For larger quantum dots the band potential becomes shallower. That results in eigenstate energies closer to the conduction band. In addition to the absolute energy, the energy difference between s- and p-like-states ΔE_{sp}, as well as between higher states decreases with increasing size. While for small dots $\Delta E_{\mathrm{sp}} \approx 2\,\mathrm{meV}$, for large dots $\Delta E_{\mathrm{sp}} \approx 0.4\,\mathrm{meV}$.

The wave functions calculated in the effective-mass approximation for discrete states have a pancake-like form and extend over more than 20 nm in-plane, but less than 10 nm in z-direction for a dot of 80 nm size. s- and p-like-state wave functions are shown in Fig. 11.4 for a magnetic field H of 3400 Oe applied along the growth direction z. With a shallower potential the size of the wave functions increases: Fig. 11.5(a) shows the ground state wave function for dots of base diameters (i)/(ii) 80 nm and (iii)/(iv) 120 nm. The s-like wave function is extending, but the symmetry is preserved. The same applies to larger dots up to 200 nm base diameter. Correspondingly, the excited states increase in size. A magnetic field has no visible effect on the s-like wave function, but the p-like wave function is influenced. In Fig. 11.5(b) the p-like wave function is shown for a magnetic field applied in the (i)/(ii) xy-plane and (iii)/(iv) along z-direction.

The electron s-like wave function is centered in the silicon on top of the dot, directly at the SiGe/Si interface z_0. With the spatial extensions of the wave functions significantly larger than the Bohr-radius in Si the dot might act as a single heterointerface. The barrier effect depends on the intermixing as can be seen by comparing Figs. 11.4(a) and 11.5(a) where dots of 80 nm base diameter are shown with different Ge content. The wave function in the xz-plane appears more flattened for larger Ge content. This barrier effect will be somewhat different for the p-states, which have a node at the apex of the dot and extends larger in-plane. In addition to the states at the apex of the dot, there are confined states below the SiGe island. Since the conduction band potential is slightly shallower, the confined energy states are also slightly higher in energy. Nevertheless the symmetry of the individual wave functions is the same mirrored at the SiGe barrier.

The alloy distribution within the $\mathrm{Si}_{(1-x)}\mathrm{Ge}_x$ islands and the Ge content influences the strain profile. Ge content can be estimated from the AFM and TEM analysis. For dots grown at 600°C the average Ge content $x \approx 0.5$. Dots grown at 700°C have $x \approx 0.4$. The Ge content at the apex of the dot can be

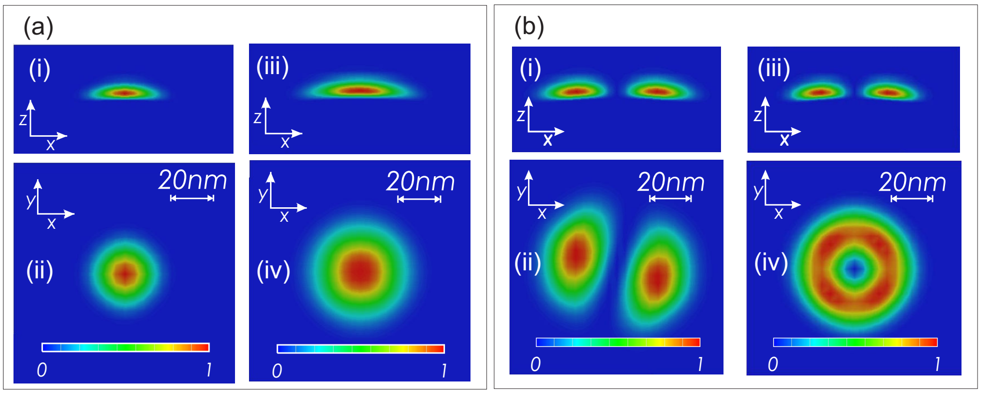

Figure 11.5: (a) s-like state wave function for dots with $x = 0.5$ and with base diameter of (i)/(ii) 80 nm and (iii)/(iv) 120 nm. (b) p-like state wave function for a magnetic field of 3400 Oe in xy-plane (i)/(ii) and along z-direction (iii)/(iv) for a dot of 120 nm base diameter.

higher than the average value. For small dots the Ge content has a relatively large effect on the conduction band profile and the ground state energy. For a 80 nm dot with $x = 0.5$ the minimum of the confining potential is $\Delta E \approx -53$ meV below the Δ conduction band of unstrained Si. For $x = 0.4$ it is just slightly below 40 meV. The energy difference between the corresponding s-states is $\Delta E_s \approx 10$ meV. For the large dots, variations from $0.35 \leq x \leq 0.45$ result in a change of ground state energies within $\Delta E_s \approx 3$ meV. For both types of dots, the relative energy difference between s- and p-states changes within 20% of ΔE_{sp} for alloy concentrations from $x = 0.36 - 0.52$.

11.3.2 Multiple Quantum Dots

Several calculations were performed where two dots were placed laterally or multiple dots were arranged laterally and vertically. For the lateral spacing dot densities were estimated from the AFM pictures. Even for small dot spacings of 20 nm base edge to base edge, the influence on the Δ_2 state at the apex is negligible. Also, no electronic coupling occurs between the Δ_4-states at the base. The Δ_4-band edge at the base of the dot is still higher in energy then the Δ_2-band edge at the apex. Therefore the ground state is still to be expected at the apex of the dot. This is in agreement with simulations for patterned samples where SiGe quantum dots are regularly spaced [122].

The strain fields around a SiGe island can extend quite far into the Si ma-

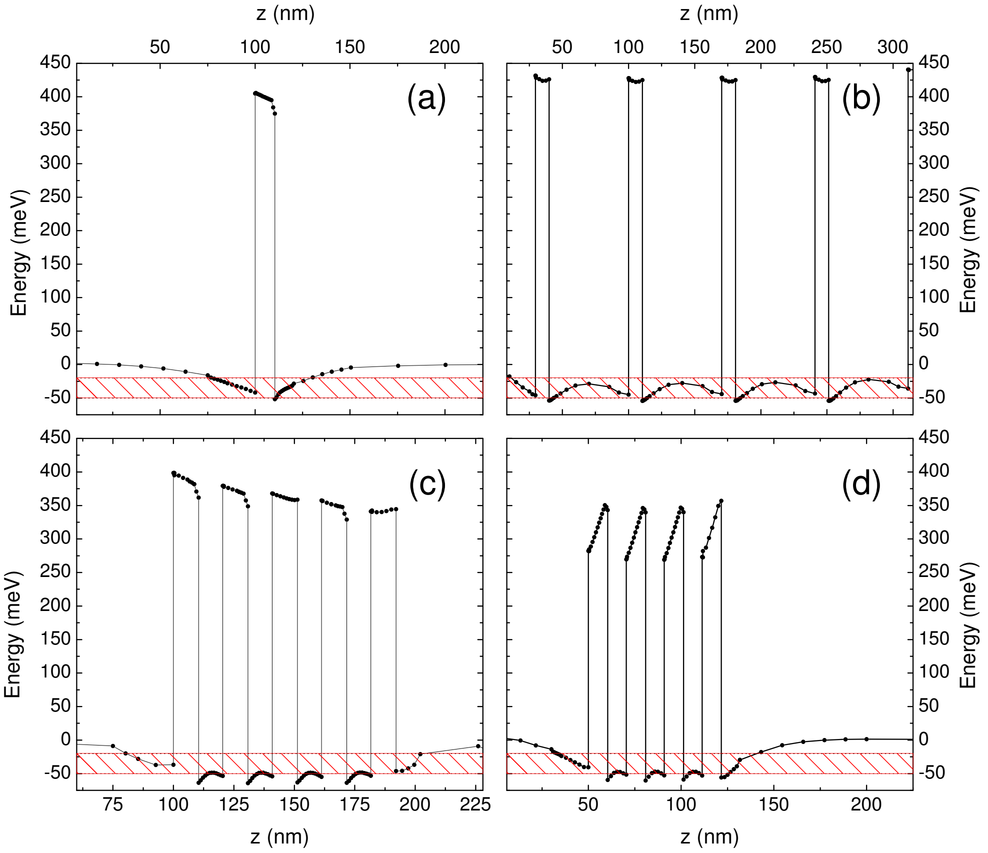

Figure 11.6: Δ_2 conduction band profile along z-direction, centered in the middle of the xy-plane. (a) A single dot, (b) stacked dots with 70 nm Si spacer and stacked dots spaced 20 nm apart with varying Ge content from dot to dot (c) and linear Ge variation within the dots (d) are shown. Shaded areas indicate range of donor ionization energies. For details see text.

trix. From the AFM analysis it is visible that an alignment of dots does not take place anymore for a vertical spacing of 100 nm. The dots can be regarded as isolated. At the smallest spacers of 20 nm islands are vertically aligned. This results in a variation of the dot sizes within and from layer to layer. For a spacer of 70 nm dots are aligned for the 200 nm dots, while the 80 nm dots are also randomly distributed in every layer. Simulations were performed on three to five vertically stacked dots. For simplicity the shape of dots in the top layer were assumed to be identical in shape and the simulation space was closed by a Si region as the top region.

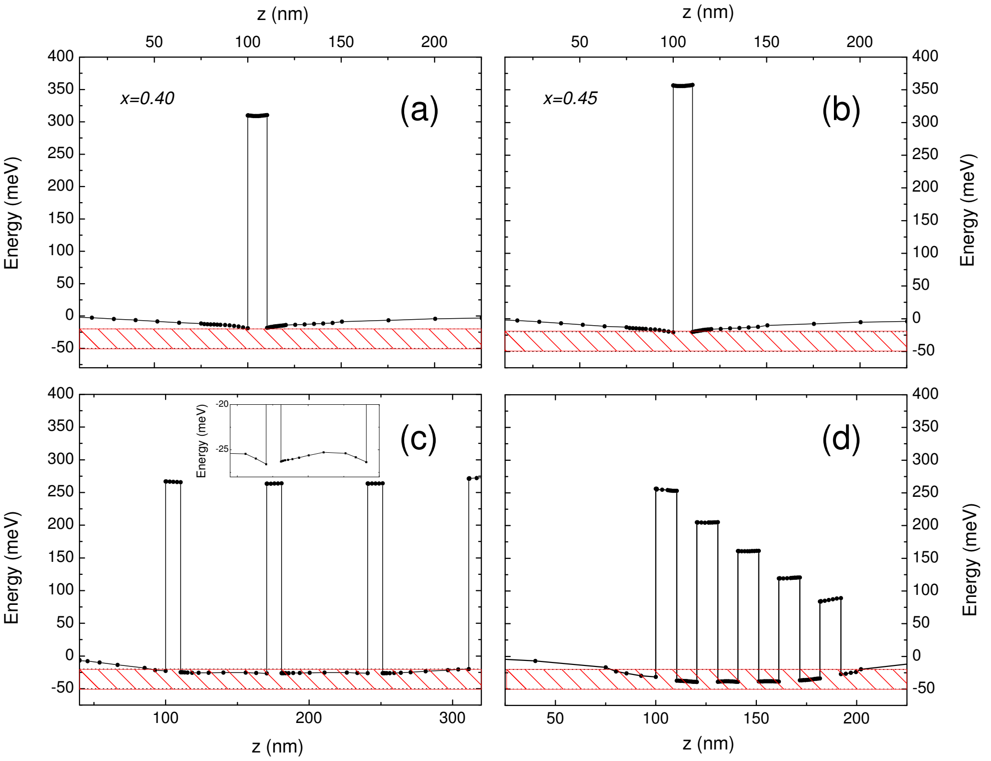

Figure 11.7: Δ_2 conduction band profile along z-direction, centered in the middle of the xy-plane. (a) A single dot with constant $x = 0.4$ and (b) $x = 0.45$; (c) stacked dots with 70 nm Si spacer and (d) stacked dots spaced 20 nm apart with varying Ge content from dot to dot. Dashed lines indicate range of donor ionization energies. For details see text.

The conduction band profiles for these different cases are shown in Fig. 11.6 for the small dots and Fig. 11.7 for the large dots. In Fig. 11.6(a) an isolated single dot is shown with a constant $x = 0.5$. In agreement with the AFM analysis, at distances of about 100 nm away from the dot, the conduction band energy is that of unstrained Si. This dot is representative for isolated dots in the structures with 100 nm vertical spacing. In Fig. 11.6(b) there are five dots spaced 70 nm apart. Their Ge content is constant as well. One can see that the conduction band does not recover completely to the unstrained band edge in between the quantum dots. Nevertheless the potentials above and below the dots are still fairly steep and electronically isolated. For the fifth (top) dot only the lower barrier is shown in correspondence to the real structure. In Fig. 11.6(c) dots with a spacing of only 20 nm are plotted. Here the Ge content in each dot is kept constant, but it is changing linearly from the bottom (0.52) to the top dot (0.47). The fifth dot and the Si on top is shown completely. The abrupt changes in the band energy above and below the dots are due to the reduced number of grid points and the way the quantum region is defined for this simulation. The four dots in Fig. 11.6(d) have a linearly increasing Ge content from the bottom (0.25) to the top (0.52) of each dot. The last two subfigures are representations of Vegard dependencies, in order to test the higher disorder expected in the aligned samples. For both scenarios there is no significant difference in the confining potentials and the energy states. From (c) and (d) it can be seen that at a distance of 20 nm in between quantum dots there is a joint electronic state possible. Overall, the confining potentials are deeper for the dots with 20 nm spacing compared to the isolated dot. This results in a first confined state of -46 meV at the stacked dots as compared to -34 meV at the isolated dot. Confining potentials for aligned dots with 70 nm spacing and isolated dots are almost identical.

In Fig. 11.7 the limiting cases for the 200 nm dots are shown: Isolated dot with different Ge contents as compared to the stacked dots spaced 70 nm and 20 nm apart. For the single dots in Fig. 11.7(a) and (b) the potentials are very shallow with conduction band minima found close to 25 meV. This is significantly smaller than in the smaller dots. The dots with 70 nm spacing are slightly lower in energy. Although their potential is very shallow and the conduction band is lowered in between the dots, the confined states are still located at the individual dots. The lowest energy state is found at $E_{\mathrm{s/p}} \approx 26$ meV below the conduction band edge. Note that for the conduction band profile shown in Fig. 11.7(c), due to computational reasons, the spacing of grid points had to be reduced. Therefore the profiles below the dots and at the boundaries of the structure are not very accurate. Five dots spaced 20 nm apart are shown in Fig. 11.7(d). The conduction band minima is close to 39 meV. Similarly for the smaller dots, there is a joint confining potential in between the dots.

11.4 Discussion

One important consequence of temperature is the carrier concentration in a semiconductor. At temperatures where thermal activation of electrons from the valence band to the conduction band is not possible anymore the carrier concentration is dominated by the doping profiles. Donors and acceptors are treated in nextnano^3 as additional charges in defined regions. Due to this, the quasi-Fermi levels are changing and with that the electronic potential. Donor concentrations and their ionization energies can be defined within the regions. Although discrete energy levels can be specified the effect of impurity bands at high impurity concentrations and, more importantly, strain and alloy effects on the energy levels cannot be implemented.

As described in Section 10.2 background doping is present with the phosphorus donor the most likely one present in the investigated heterostructures. The ionization energy for the shallow donor P in Si is 45 meV. Under the influence of strain doublet and triplet states become populated. Their energy is found around 30 meV below the conduction band edge. In Ge the ionization energy for P is with 13 meV significantly smaller than in Si. The ionization energy for P donors in $\mathrm{Si}_{(1-x)}\mathrm{Ge}_x$ was experimentally determined to decrease with increasing Ge content [169]. For the highest Ge content $x = 0.27$ investigated in [169], an ionization energy of $E_i \approx 26$ meV was reported. Considering that the SiGe structures investigated in this thesis can have Ge contents of $x \approx 0.5$, $E_i \approx 20$ meV and even smaller seem likely. Since there are quasi continuous strain fields around the quantum dots in Si, as well as changing alloy profiles (and strain effects) within the SiGe islands, a broad distribution of energy levels between 45 meV and 20 meV can be expected.

The energy range between 50 meV and 20 meV is indicated as shaded area in Figs. 11.6 and 11.7. If the energy states at the quantum dots are lower or within this range electrons can be trapped at the quantum dots instead of the donors. For the smaller quantum dots the conduction band is lowered to 50 meV or even below. Potentially, almost all electrons can be trapped at the quantum dots in the heterostructures for all three spacings.

For the large dots confining energies are smaller. The conduction band minima for the isolated dots are just around 25 meV and the confined states are slightly higher in energy. That means that the dots can only be populated by few electrons, namely those which originate from donors with smaller ionization energy. Eventually some dots are not populated at all. At the dots with 70 nm spacing the lowest confined state is with 26 meV still higher in energy than the donor states in pure Si. Therefore a low population of quantum dots is expected as well. Differently, the confined states for the 20 nm spaced quantum dots are with 35 meV in the range of donor states in strained Si. A higher population is expected, but still not all donors can contribute electrons to the quantum dots.

The estimated impurity concentration is $2.3 \cdot 10^{16}\,\mathrm{cm}^{-3}$. This corresponds to a single donor in a volume of $V_d \approx (34\,\mathrm{nm})^3 \approx (4\,\mathrm{nm}\cdot 100\,\mathrm{nm}\cdot 100\,\mathrm{nm})$, approximately the size of a SiGe island. That means there are only few donors present inside SiGe islands, in the strained Si regions around it and few more which are not subjected to strain at all. Therefore the electronic population of quantum dots should be small.

In this discussion a potential interplay between the two confining states, namely the donor state and the quantum dot potential is not considered. In principle, since the states are close in energy, there could be more complex interactions present. This is certainly a point worth looking into, but which is beyond this qualitative model.

11.5 Summary

The influence of different parameters, as alloy contribution, size, shape and magnetic field, on the Δ conduction band profile and confined states was studied for single SiGe islands embedded in Si.

The lowering of the conduction band depends primarily on the aspect ratio of the semiparabolic quantum dots. Secondarily the Ge content influences the conduction band energy. The relative energy difference between confined states decreases significantly with increasing base size of the quantum dot. The size of the wave functions increases, but its symmetry is preserved.

Calculations for the experimentally investigated structures show that SiGe quantum dots grown at 600°C have confining states on the order of donor states in Si. Quantum dots grown at 700°C have a shallower potential with confining states on the order of donor states in SiGe and strained Si. The latter dots are expected to be populated by a few electrons only.

While electronic states for 70 nm and 100 nm spacing are only seeing one

SiGe/Si barrier the electronic states for 20 nm spacing are expected to be confined in between two barriers. The effect on the shape of the wave functions is small.

CHAPTER 12

ESR Experiments on Si/SiGe Quantum Dots

In this chapter the experimental results of ESR on the SiGe quantum dot structures are reported. Two ESR peaks with different g-factor tensors were found around $g = 1.999$ in some structures, while in others only a single peak was observed. These spectral features are only observed in samples with quantum dots. Their spin dephasing time T_2^* is estimated to be on the order of 0.2-0.5 μs, whereas the spin lifetime T_1 is on the order of 10 μs. The relative intensity of the ESR signals can be changed by illumination with infrared light, with energy below the gap of bulk Si and of the wetting layer. A qualitative model of the electronic structure of the heterostructures based on calculations with nextnano^3, derived in the last chapter, enables us to attribute the observed ESR signals to confined electronic states at the quantum dots.

12.1 ESR on Si Structures

Semiconductors can be doped with impurity atoms. If a Si atom is replaced by an atom from group V of the periodic table an unsaturated bond remains. The additional electron is only weakly bound to this donor atom. Typical donor atoms in Si and Ge are the group V elements P, As, Sb. They are shallow donors with ionization energies of 54 meV, 45 meV and 39 meV respectively

[170]. The ionization energies are small compared to the bandgap energy of 1.11 eV of Si. At negligible impurity concentrations the semiconductor is called an intrinsic semiconductor and the carrier concentration is given by the thermal activation of carriers from the valence to the conduction band. In the case of strong doping (usually $n > 10^{18}\,\mathrm{cm}^{-3}$) the electron wave functions of the donor atoms overlap and form impurity bands. Those bands are located at energies just below the conduction band energy, as seen from the ionization energy compared to the bandgap energy. In the intermediate doping regime, donors are regarded as isolated impurities.

This simple description of donors in a semiconductor can be similarly applied to acceptors, dealing with holes instead of electrons and the valence band instead of the conduction band. Beyond this very basic description the multi-valley structure of the valence band has to be considered, which is specific for the individual semiconductor and usually more complicated than for the conduction band [170].

A multitude of ESR experiments have been performed on Si-based systems. ESR signals in bulk Si can originate from impurities which are shallow and deep donors (or acceptors). When an electron is bound to a donor it acts as a paramagnetic defect and can be detected with ESR. Although already widely investigated in the 1960s today it is a highly active field due to the need to understand the physics of donor states in Si structures for photovoltaic applications [35] as well as having the possibility to perform quantum computational operations in those systems [120].

Thinking of an electron bound to a donor we are dealing with an electron-hole system, where the electron is spatially confined in the Coulomb potential of the donor. In contrast to the donor electrons, conduction band electrons in Si can be regarded as free in the three spatial dimensions. At low temperatures the conduction band electron can be generated by illuminating the Si sample. An ESR signal of the three-dimensional impurity band electrons is found with a g-factor $g = 1.99875$ [33]. Their ESR signal is isotropic and its linewidth at about 10 GHz is about 1 G [33].

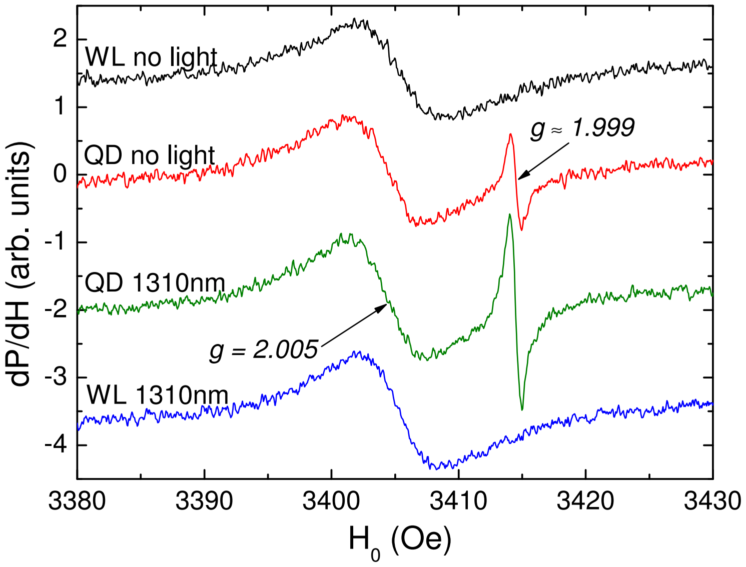

Figure 12.1: ESR spectra of a sample with only wetting layers and a sample with quantum dots; A narrow ESR peak is observed in the quantum dot samples (QD) which is amplified under sub-bandgap light $\lambda = 1310\,\mathrm{nm}$ illumination; reference structures - here a sample with only wetting layers (WL) - do not show the signal

12.2 Experimental Results

In an electron spin resonance experiment the overall response of the sample is measured. Therefore great care has to be taken to separate an ESR signal attributed to SiGe nanostructures from signals originating from donors or impurities in the bulk substrate or in the deposited material, as well as effects caused by the boundaries between different materials [171]. As a consequence the reference structures were measured to ensure that the observed signals are only due to the presence of the SiGe dots.

Experiments were performed at $T \lesssim 4\,\mathrm{K}$. Surprisingly, in all our structures the well known signal of electrons on donors [33] in Si is not observed. This might be due to the fact that the absolute number of donors is on the order of the number of quantum dots, but their ESR-linewidth is about one order of magnitude broader than the ESR linewidth of quantum dots. This results in weaker intensity of the line. Furthermore, for the samples with quantum dots the inhomogeneity of the sample may contribute to an additional broadening: Donors are distributed throughout the whole structure

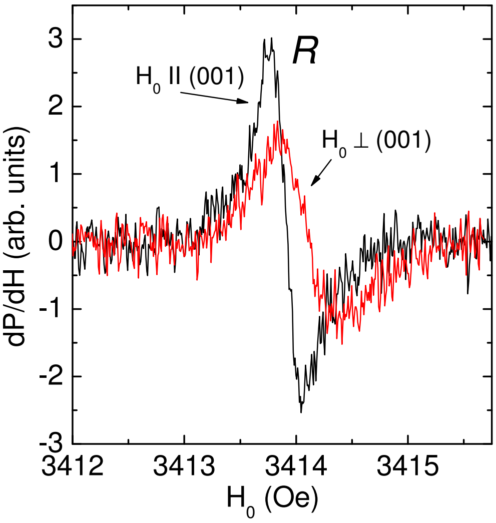

Figure 12.3: ESR signal (single peak) associated with dots in the sample grown at 600°C with a spacer of 100 nm. The two spectra were taken with magnetic field oriented parallel and perpendicular to the growth direction (001).

randomly. Thus, electrons on donors experience different strain. Since the repopulation effect between the donor states results in a reduction of hyperfine splitting with increasing strain [119], their ESR signal is expected to broaden even more. A quantitative description is given in Section 12.3.

Fig. 12.1 shows ESR spectra of a WL and a quantum dot sample in the region around a g-factor value of 2. The spectrum of the WL sample is representative for all reference structures which show only a single peak with a linewidth $\Delta H_{pp} \approx 5\,Oe$ centered at $g \approx 2.005$. This signal is attributed to the oxidized sample surface, since it is in good agreement with previous reports on ESR of dangling bonds of Si at the Si/SiO$_2$ interface[172]. In all quantum dot samples we observe an additional narrow peak, showing quantitative differences for the individual multilayer samples. This feature is absent in all reference structures. Therefore these signals are analyzed in more detail for the different quantum dot structures.

12.2.1 Samples grown at 600°C

All samples grown at 600°C - with a silicon spacer thickness of 20 nm, 70 nm and 100 nm - give an ESR signal showing only a single Lorentzian line (R) (see Fig. 12.3). For an incident microwave power P$_{\mathrm{mw}}$ of 1 mW the line for the 100 nm sample (Fig. 12.3) shows a small anisotropy in g-factor of $\Delta g = g_\parallel - g_\perp = 1.1(2)\cdot 10^{-4}$ with the g-factor being axially symmetric and an anisotropy in the linewidth ranging from $\Delta H_{pp\parallel} \approx 0.25$ Oe to $\Delta H_{pp\perp} \approx 0.45$ Oe. At higher powers the line broadens and the signal starts to saturate.

The g-anisotropy for all samples grown at 600°C is the same within the experimental error [see later Fig. 12.5 (a)] ranging from $\Delta g = 1.1(2) \cdot 10^{-4}$ to $1.3(2) \cdot 10^{-4}$. However, the absolute values of the g-factors are slightly higher for the 20 nm sample than for 70 nm and 100 nm spacing. g-factors are listed in Tab. 12.1. Control measurements carried out at another time show slightly different values of the g-factor. This reproducibility is within an error of about $\delta g_{\parallel} = 3 \cdot 10^{-5}$ and $\delta g_{\perp} = 4 \cdot 10^{-5}$, but does not affect the anisotropy Δg.

Sample	$g_{\parallel}$	$g_{\perp}$	Δg	g_0
600°C, R				
20 nm	1.99925(2)	1.99912(2)	0.00013	1.99916
70 nm	1.99919(2)	1.99906(2)	0.00013	1.99910
100 nm	1.99917(2)	1.99906(2)	0.00011	1.99910
700°C, R				
20 nm	1.99925(2)	1.99912*	0.00013	1.99916
70 nm	1.99926(2)	1.99914(2)	0.00012	1.99918
100 nm	1.99923(2)	1.99907(2)	0.00016	1.99912
700°C, L				
20 nm	1.99941(2)	1.99923*	0.00018	1.99929
70 nm	1.99945(2)	1.99909*	0.00036	1.99921
100 nm	1.99943(2)	1.99892*	0.00051	1.99909

Table 12.1: g-factors measured at $P_{mw} = 1$ mW; the reproducibility is $3 \cdot 10^{-5}$ for $g_{\parallel}$ and $4 \cdot 10^{-5}$ for $g_{\perp}$; values marked with * are extrapolated from the fit around $g_{\parallel}$ shown in Fig. 12.5. For this an axial symmetry of the g-factor is assumed.

12.2.2 Samples grown at 700°C

All samples grown at 700 °C show a remarkable difference with respect to samples grown at 600°C: the observation of two ESR peaks [see Fig. 12.4(a)]. This double peak spectrum is a new feature which has not been reported before for ESR studies of SiGe islands [130, 131]. The peaks are sharper than the single peak observed in samples grown at 600 °C. The relative intensity between the two peaks is the same for samples with 100 nm and 70 nm spacer. Exemplarily, let us focus on the latter.

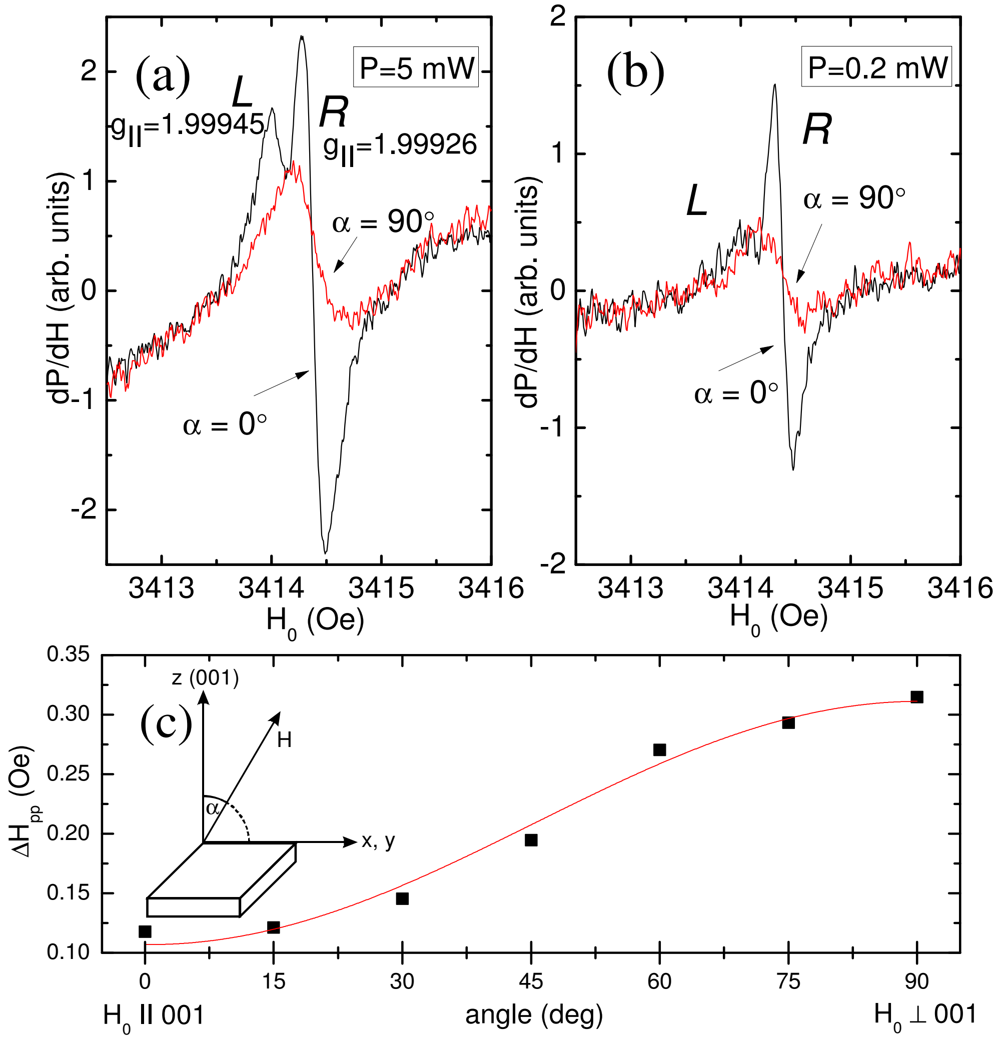

Figure 12.4: Spectra of the sample grown at 700 °C with 70 nm spacer (a) $g_{\|}(R) = 1.99926$ and $g_{\|}(L) = 1.99945$ at $P_{mw} = 5\,\mathrm{mW}$ and (b) $P_{mw} = 0.2\,\mathrm{mW}$; (c) linewidth of the peak with lower g-factor (R) and schematic of sample orientation. Angle α indicates the direction of the external magnetic field from the (001) direction ($\alpha = 0°$) to the perpendicular direction ($\alpha = 90°$).

The two ESR peaks shown in Fig. 12.4 are characterized by g-factors of about 1.9992 (R) and 1.9994 (L) (with the magnetic field in growth direction) and by different intensities. The stronger peak R is the one with the lower g-factor. When the magnetic field is turned towards the in-plane direction of the quantum dots the signals broaden and cannot be resolved [Fig. 12.4(a),

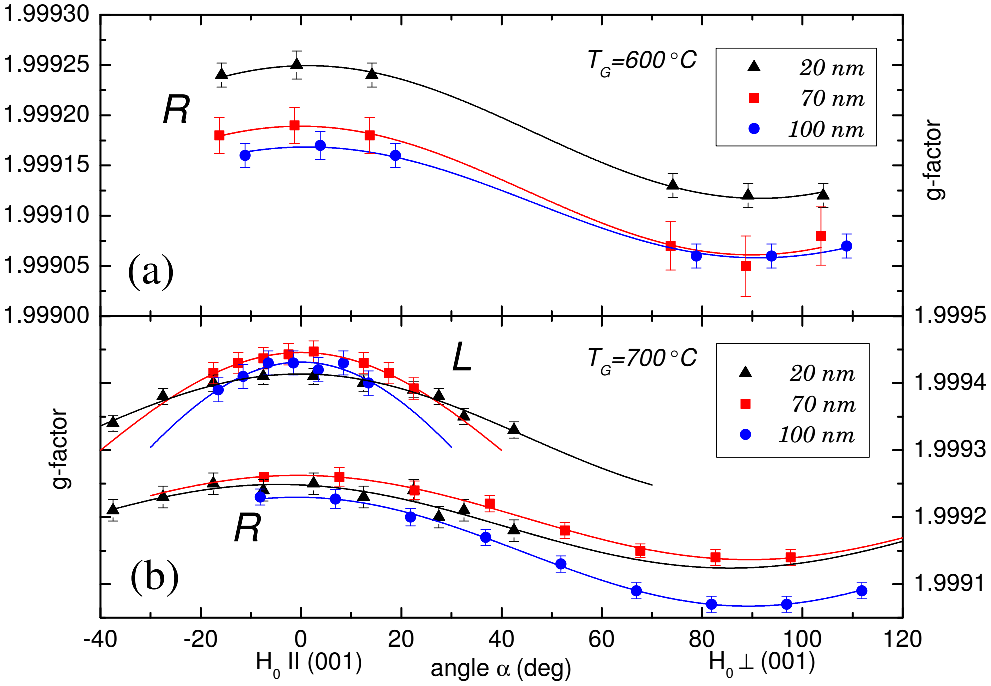

Figure 12.5: Angular dependence of the g-factor determined at $P_{mw} = 1\,\text{mW}$; (a) samples grown at 600°C, (b) samples grown at 700°C. The spacer thickness is indicated.

(b)]. By varying the microwave power the relative intensity of the two peaks changes. At low powers L is almost not visible which makes further characterization of R possible [Fig. 12.4(b)]. By changing the orientation of the sample with respect to the external magnetic field again an anisotropy in the linewidth [Fig. 12.4(c)] and of the g-factor of peak R becomes apparent [Fig. 12.5(b)]. The linewidth broadens from $\Delta H_{pp} \approx 0.12\,\text{Oe}$ to $\Delta H_{pp} \approx 0.32\,\text{Oe}$. From the linewidth below saturation the dephasing time T_2^* can be calculated as[10]:

$$T_2^* = \frac{1.3131 \cdot 10^{-7}}{g \Delta H_{pp}\,[\text{Oe}]}\,[\text{s}] \tag{12.1}$$

Linewidths correspond to T_2^*-times ranging from $T_2^* \approx 0.5\,\mu\text{s}$ to $\approx 0.2\,\mu\text{s}$. This provides a lower limit for the T_2 spin coherence time, which is usually longer than T_2^*. The g-factor of R shows an axial symmetric anisotropy with $g_{\parallel}(R) = 1.99926(2)$, $g_{\perp}(R) = 1.99914(2)$ and $\Delta g = 1.2 \cdot 10^{-4}$.

Unfortunately a complete characterization of L is not possible for this sample, since even for the highest microwave power below saturation the contribution from R cannot be separated completely from L as the sample is turned towards the in-plane direction. Because of this, L is only characterized in an angle of $\pm 20°$ around $\alpha = 0°$, $H_0 \parallel (001)$ for which the lines are still resolved yielding $g_{\parallel}(L) = 1.99945(2)$. When assuming the same axial symmetry derived for $g(R)$, the value for $g_{\perp}(L)$ can be extrapolated to $g_{\perp}(L) = 1.99909$ (Fig. 12.5).

For the sample with the smallest spacing of 20 nm silicon the spectrum looks quite different (see later Fig. 12.8). Still two peaks are observed, but with L having higher intensity. Nevertheless, the g-factor corresponding to L and R for different samples is almost identical regardless of the change in relative intensity. This indicates that L and R originate from individual spin states which are present in all samples.

The integrated intensity of the ESR signal below saturation is proportional to the number of resonating spins contributing to the signal. Thus, in a non-saturated regime for both signals their relative intensity gives information about the relative population of those two states. For the 100 nm and 70 nm samples the integrated intensity ratio is about $L/R \simeq 1/5$, while for the 20 nm sample it is about $L/R \simeq 1/1$. Thus, a drastic change in the relative population of the two states takes place as the distance between the dots is decreased. Due to this transfer of the spectral weight, both peaks can only be determined in an angle of $\pm 40°$ around $g_{\parallel}$. The g-values for R are the same as for the 20 nm spaced dots grown at 600°C. Since the g-factor anisotropy of L is stronger the two lines merge upon rotation of the field towards the sample plane and are not resolved anymore. For R alone a broadening is observed as well.

The linewidth in cw-ESR is connected to the dephasing time T_2^* of a spin ensemble. The additional broadening as well as the anisotropic g-factor indicates a change in the spin-orbit coupling as the magnetic field is turned in-plane.

Considering inhomogeneities of the magnetic field throughout the sample as well as dipole-dipole interactions, the ESR signal of an ensemble of identical spins should show a Gaussian line. Since all lines observed are of a Lorentzian form, there has to be a mechanism present that narrows the line again. Since the distance between the dots is substantially longer than the

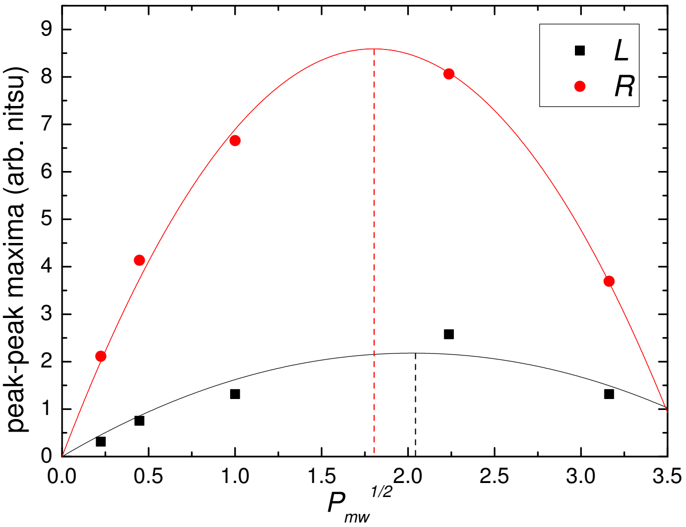

Figure 12.7: Relative power dependence of ESR peaks L and R as a function of microwave power for the sample with 70 nm spacer. Saturation power is indicated as a dashed line for both spectra.

size of the confining potential, the isotropic exchange interaction between the spins at the same quantum dot seems to be a primary source of the line narrowing.

12.2.3 T_1-Relaxation Time

The saturation of a signal in continuous wave ESR is related to the T_1-relaxation time, which is the time for a single spin to reverse its orientation. By applying high microwave radiation powers the thermal equilibrium between the split spin orientations in magnetic field can be disturbed yielding equalization of the population of both spin states. Thus, the ESR signal saturates and eventually decreases in intensity.

By determining the saturation power the relaxation time can be calculated. For the power resulting in the maximal derivative amplitude of the ESR signal T_1 is given by [10]:

$$T_1 = \frac{0.49 \cdot 10^{-7} \Delta H_{pp}\,[\mathrm{Oe}]}{g H_1^2\,[\mathrm{Oe}^2]}\,[\mathrm{s}] \tag{12.2}$$

It has to be noted that the microwave magnetic field H_1 at the sample is calculated from the known calibration of the resonator without quartz cryostat. The real H_1 might be different due to the quartz cryostat and the microwave conductivity of the sample itself. Therefore values obtained for T_1 cannot be very precise. In addition, the weak intensity makes it difficult to find the

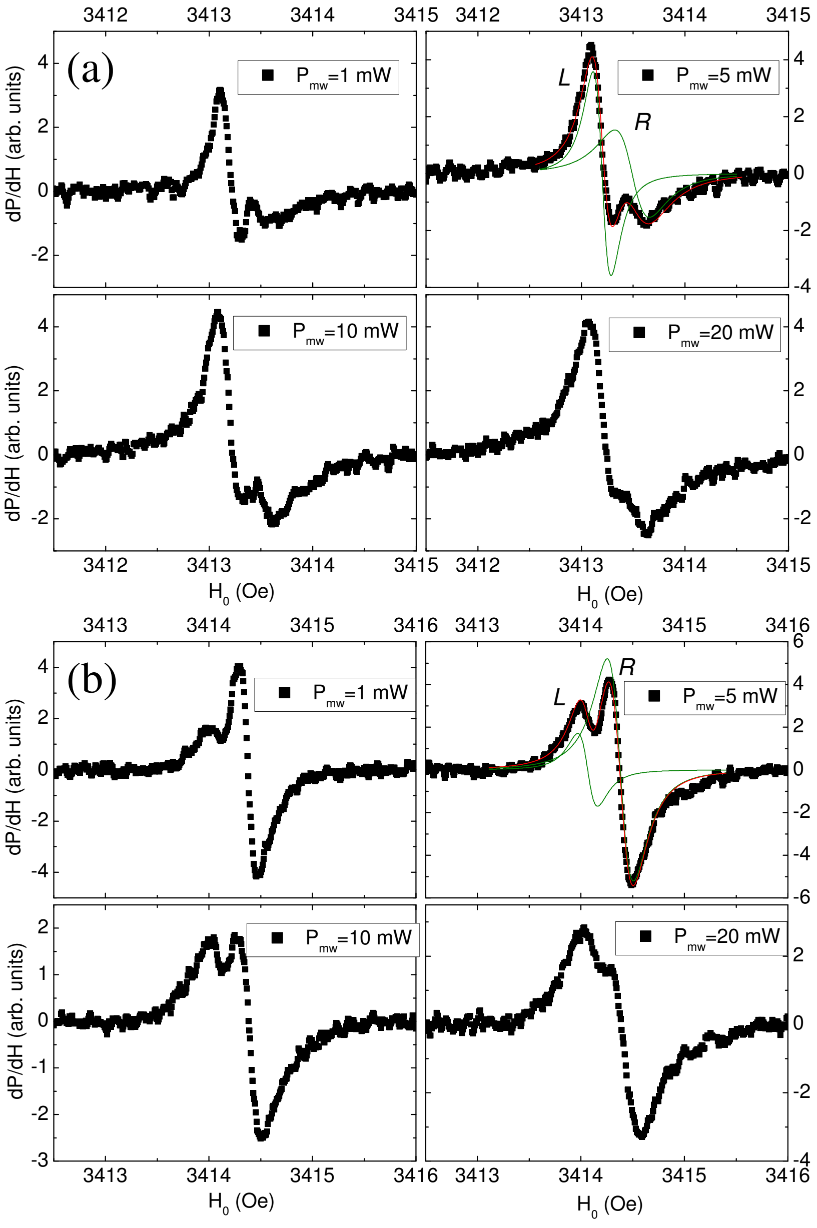

Figure 12.8: ESR spectra for selected P_{mw} from 1 mW to 20 mW for (a) 20 nm and (b) 70 nm Si spacer; graphs at 5 mW show data with double Lorentzian fit and the single Lorentzian lines extracted. The external magnetic field is along the growth direction (001).

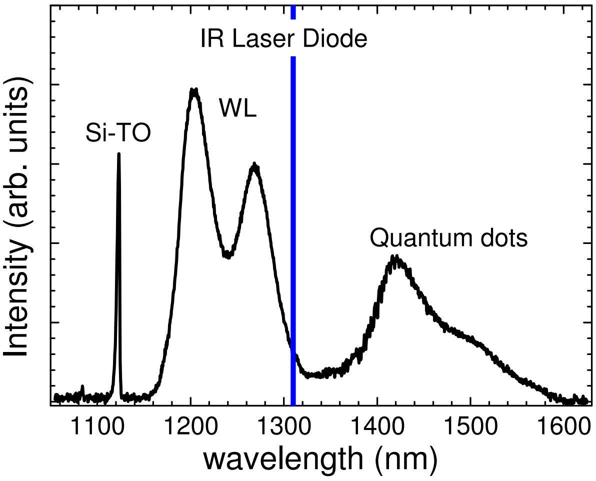

Figure 12.10: Low temperature (about 8 K) photoluminescence of the SiGe quantum dot multilayer grown at 700°C with 100 nm spacing. Si peak, wetting layer and SiGe quantum dot emissions are indicated as Si-TO, WL and quantum dots, respectively. The blue line marks the laser excitation wavelength $\lambda = 1310\,\mathrm{nm}$ used in ESR measurements. *Measurement: F. Pezzoli*

exact saturation point. Nevertheless, an order of magnitude estimate of T_1 yields a value of the order of $T_1 \lesssim 10\,\mu s$ for both peaks. Typically relaxation times of L are just slightly longer than those of R.

12.2.4 Effect of Illumination

Samples were illuminated with light at wavelengths of $\lambda_1 = 655\,\mathrm{nm}$ (red) or $\lambda_2 = 1310\,\mathrm{nm}$ (infra-red - IR). This corresponds to energies $E_1 = 1.5\,\mathrm{eV}$ and $E_2 = 0.95\,\mathrm{eV}$ respectively. With the Si bandgap being at $E_g = 1.1\,\mathrm{eV}$ electron hole pairs in Si can be generated with the red laser. Ionization of the shallow donors and acceptors in Si (for instance: phosphorus and boron $E_P \simeq E_B \simeq 45\,\mathrm{meV}$) also takes place. Looking at photoluminescence measurements of the samples [1] (see Fig. 12.10) it is evident that the excitation wavelength of the IR-laser is below the Si bandgap and even partially below the wetting layer. On the other hand, the quantum dot emission is well below the IR excitation energy.

While no ESR signal could be found in any reference sample without light,

---

[1] Micro-Photoluminescence (μPL) investigations have been performed at about 8 K, using a cold-finger helium flow cryostat and a 532 nm frequency doubled Nd:YVO4 laser. The laser spot diameter on the sample surface was of about 1.5 μm with a power of about 1 mW. The same μPL microscope was then used to collect the PL emission, which is dispersed by a 500 mm focal length spectrometer, equipped with a liquid nitrogen cooled InGaAs array detector. *Measurements: F. Pezzoli*

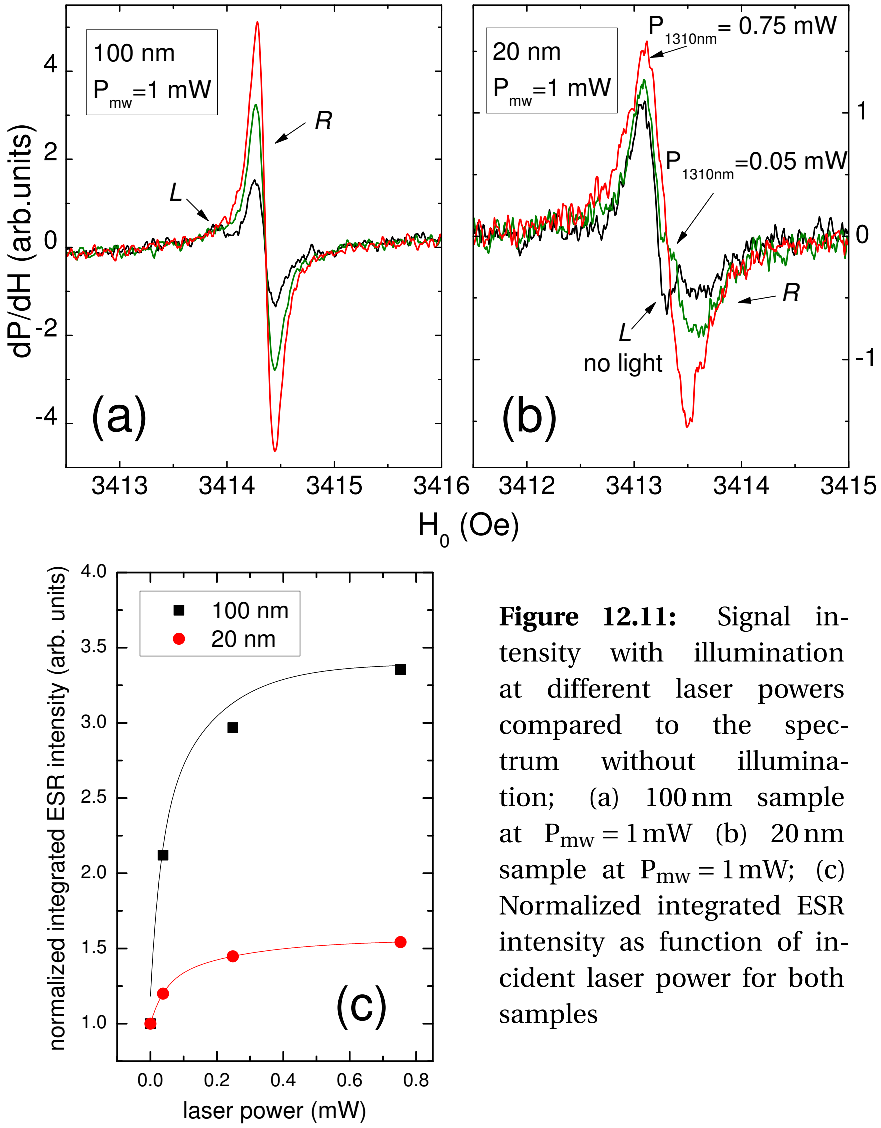

Figure 12.11: Signal intensity with illumination at different laser powers compared to the spectrum without illumination; (a) 100 nm sample at $P_{mw} = 1\,mW$ (b) 20 nm sample at $P_{mw} = 1\,mW$; (c) Normalized integrated ESR intensity as function of incident laser power for both samples

an ESR signal around $g = 1.9995$ was observed on those samples under illumination with the red laser light ($\lambda_1 = 655\,nm$). This g-factor is identical with the g-factor of conduction band electrons in Si. The linewidth is similar to the one reported previously for bulk silicon [173] $\Delta H \approx 1\,Oe$. Since the g-factors of conduction band electrons and electrons on quantum dots are very close, so that their ESR signals might overlap, the experiments focussed on illumination with sub-bandgap light.

For the sub-bandgap IR-laser no additional signal in all reference structures can be seen. In contrast to that, in the quantum dot structures the already visible signal increases significantly (Fig. 12.1).

By illuminating the quantum dot samples grown at 600°C the intensity of the single ESR peak increases strongly. The increase does not go along with a change of the linewidth which would indicate a faster relaxation. Thus, it can be interpreted as a pure increase of the number of spins giving rise to the ESR signal.

More interesting is the behavior of the double peak spectra: The two signals are amplified differently under illumination with sub-bandgap light. For the 100 nm sample at a microwave power of 1mW [Fig. 12.11(a)] the two peaks are well separated for the spectrum without illumination and only R is increasing in intensity upon illumination. From the data it is not clear if L is simply masked by R or if it is even decreasing in intensity. Thus, the electronic state corresponding to R gets populated under illumination, revealing a non-linear dependence on the laser power for the integrated ESR intensity [Fig. 12.11(a), inset].

For the 20 nm sample the two peaks are also clearly visible at a microwave power of 1mW in the spectrum without illumination [Fig. 12.11(b)]. Upon illumination with only a small laser power L decreases while R increases. By increasing the laser power R increases further and L is not visible anymore. This indicates a shift in population from L (or the electronic state giving rise to L) to R at first, and, with higher light intensity, a continuous increase of the population of the R-state.

We rationalize the above observations as follows: In silicon at temperatures around 4 K most of the electrons are localized at shallow donors and the electron concentration in the conduction band is small. Upon illumination with above bandgap light electrons are excited from the valence to the conduction band. This increase in the electron concentration makes observation of the conduction band electrons with ESR possible even at low temperatures in the reference structures (cf. [173]). Besides the direct generation of carriers from the valence band, ionization of donors takes place as well. Illuminating at a wavelength of $\lambda_2 = 1310$ nm, with an energy well below the bandgap of silicon and below the wetting layer emission energy, the ionization of donors is the major process providing conduction band electrons in the reference structures. The concentration in the conduction band is increasing, but is much lower than for the electron-hole generation from the valence band with above bandgap light. The ionization of donor electrons alone does not provide a sufficient amount of conduction band electrons that could be detected by continuous-wave (cw) ESR.

In the samples where quantum dots are present, ionization of donors takes place under illumination with sub-bandgap light. Furthermore, electrons may also be generated by direct absorption of photons on the quantum dots. Consequently, for both scenarios electrons are trapped on the quantum dots, resulting in an increase of the signal.

12.3 Discussion

ESR signals were observed in samples containing quantum dots only, not in any of the reference structures. The spectra differ quantitatively for the individual samples. For samples containing small dots a single peak is observed, while for large dots an additional peak is found. The double peak spectrum originates from two spin sites. The microwave power dependence, the behavior under illumination with sub-bandgap light as well as the anisotropy Δg are different for the individual peaks L and R. This behavior for the individual peaks is consistent throughout all samples investigated.

There are two well-studied scenarios which can serve as limiting cases to the discussion of spin states on SiGe islands. (i) Electrons can be confined at donor atoms in Si, due to the Coulomb potential of the nucleus. (ii) Electrons can be confined in strained Si between SiGe barriers forming a two-dimensional electron gas.

(i) Donor states

The first well accepted theory for donor states in Si was developed by Kohn and Luttinger [174]. The Kohn-Luttinger theory describes the additional charge from the donor as being localized due to the Coulomb potential of the donor nucleus. In unstrained Si the six Δ conduction band valleys are degenerate and the ground state is a singlet state where all valleys are populated equally. Due to the finite probability for an electron to be found at the nucleus a hyperfine splitting is observed for the ground state [175]. Under the application of uniform applied stress along (001) the valley degeneracy is lifted and electrons populate the Δ_2 valleys. The hyperfine splitting vanishes [119]. Electrons of a single valley (two equivalent Δ_2-valleys), can be characterized with ESR. It turns out that the g-factor for an electron in a single valley is anisotropic with an axial symmetry coinciding with the effective mass tensor.

$$g = g_{\parallel}\mathbf{e}_{001} + g_{\perp}\mathbf{e}_{010} + g_{\perp}\mathbf{e}_{100} \tag{12.3}$$

with $\mathbf{e}_i$ the unit vectors along the crystallographic directions i, $g_{\parallel} = 1.9995$ and $g_{\perp} = 1.9984$ for P and the resulting $\Delta g = 1.1 \cdot 10^{-3}$ with $g_0 = 1.99875$.

(ii) 2DEG

It is possible to confine conduction band electrons in a two-dimensional electron gas (2DEG). For this a Si channel is grown in between two relaxed $\text{Si}_{(1-x)}\text{Ge}_x$ layers with a one-sided modulation doping. The Si-channel is strained due to the lattice mismatch between $\text{Si}_x\text{Ge}_{(1-x)}$ and the Si. Therefore the conduction band electrons are confined to the Δ_2-band [125]. The ESR signal of such conduction band electrons exhibits an anisotropy in the g-factor and the linewidth. The g-factor and its anisotropy, with respect to a magnetic field applied in the plane of the 2DEG and perpendicular to it, depend linearly on the electron concentration. The mean g-factor is $g_0 = 2.0007$ with an anisotropy of $\Delta g \approx 10^{-4}$ [127]. The anisotropy was attributed to the Byshkov-Rashba-effect [176]: The one-sided modulation doping results in an effective electrical field which is perpendicular to the $\mathbf{p}$-vector of the electrons. This leads to an effective magnetic field causing a spin splitting already at zero magnetic field. However, on similar quantum well samples other effects seem to be dominating over the Byshkov-Rashba-effect [177].

12.3.1 Quantum Dots

In the samples investigated in the present work the situation is somewhere in between the two scenarios described above: The conduction band is subject to strain around the SiGe islands. Δ_2 and Δ_4 bands are well separated in energy. Electrons are localized in the Δ_2 band and discrete electronic states are formed. However the strain is not homogenous as in the case of an uniaxial applied stress, but decreases continuously with the distance from the island. In fact the Δ_2 conduction band profile is similar to that of a modulation doped quantum well along the z-direction. In the xy-plane a harmonic-like potential is formed, limiting the extension of the wave function.

The electron wave functions have a pancake like form (Fig. 11.4) which is due to the anisotropy of the effective mass tensor and the asymmetric potential. Additionally the wave function is flattened at the SiGe/Si interface, since it acts as a strong barrier for the wave function. The s-like-state wave function is larger than that of the singlet ground state in Si, which is on the size of the Bohr radius in Si $a_0 \approx 3\,\mathrm{nm}$. The wave functions for the p-states (and for higher states) extend even further. For the large quantum dots the potentials are shallower and wave functions are even larger. Primarily the wave function extends in the xy-plane.

It is not possible to treat extended electron wave functions as conduction electrons. Nevertheless a spin-orbit coupling could be present due to the primary motion in the plane. The breaking of structural inversion symmetry (SIA) [16] along (001) indicates a Byshkov-Rashba-like spin-orbit coupling for the wave functions. g-factor and the anisotropy Δg are then different as compared to those of electrons in a homogenously strained Si region.

The g-factors observed for both peaks are in between the values for electrons localized on donors and Δ conduction band electrons in a 2DEG. Donor electrons under strain and 2DEG electrons have the form of an axial symmetry of g as observed in the quantum dots. The anisotropy Δg found is generally smaller than that expected for donor states, but in the range of Δg observed for electrons in 2DEGs [127]. For peak L the g-factor anisotropy is larger than for R. The largest anisotropy is observed for the spectrum of isolated dots where Δg_L is almost half of the anisotropy of localized donor states. The broadening of the lines is consistent with a Bychkov-Rashba-like spin-orbit coupling.

12.3.2 Assignment of ESR Lines

The calculations on large quantum dots described in Section 11.3.2 show that they can only be populated by a few electrons. On those dots two ESR lines can be distinguished experimentally. Since we are dealing with an ensemble of dots, their confining energies differ throughout an individual sample. Calculations for large quantum dots show that the energy difference $\Delta \mathrm{E}_{\mathrm{sp}}$ between s- and p-states is only about 0.4 meV. The variations in confining energies of the quantum dots within the samples allow for dots to be populated differently. This can result in individual dots where the dots are only populated by single electrons, i.e. the quantum dot is in the s-state. For other dots p-states and eventually higher states can become populated.

The left peak L observed in the doublet spectra (Fig. 12.8) shows a stronger g-factor anisotropy. This is associated with a stronger localization and is therefore attributed to electrons in the s-states. The right peak R has a smaller anisotropy. It can therefore be identified as originating from a more extended, a p-like-states. When regarding the top of the dot as a single heterointerface, an anisotropic g-factor is expected since the discrete states at the quantum dots are not spherically symmetric. The s-state is expected to have the strongest anisotropy following more closely the confining potential. Note that such an effect (much stronger in magnitude) was already observed in InGaAs quantum dots for s- and p-states [178].

Dots spaced 100 nm apart can surely be regarded as isolated. But let us consider the situation when the dots are brought closer together: With a smaller vertical spacing between the quantum dot layers and a height of the quantum dots of roughly about 10 nm, quantum dots are aligned vertically. This results in an accumulation of strain in between the quantum dots, leading to a deeper potential. Their size is not significantly different for aligned dots in different layers. However, the overall size distribution becomes wider. From the simulations in Chapter 11 it can be seen that the energy states are still on the level of donors in SiGe and the electronic states at the quantum dots are still isolated. In agreement with this, no change in the relative population of the two peaks is observed changing the spacer from 100 nm to 70 nm, but the absolute intensity of the ESR signal is increasing. This indicates more dots are being populated.

The shift in the spectral weight, as the spacing between quantum dot layers is decreased to 20 nm, reflects a change from favored p-state to s-state population [compare Fig. 12.8 (a), (b)]. In general more donor electrons can be transferred to the quantum dots because of the lowered energy for confined quantum dot states. This would result in a higher population. Still no donors in unstrained Si can contribute electrons. Additionally, the number of dots in this particular structure is higher by a factor of two which results in a smaller donor/dot ratio equivalent to a lower occupation of a single dot on average. Also, the higher disorder in the structure results in a spread of confining energies and with that quantum dots differently populated.

In general dots grown at 600°C are smaller in size with an average Ge content of about 50%. For those dots the areal coverage is higher and thus the average number of donors per dot is lower. But with larger confining energies more donors can contribute electrons to the quantum dots. This is sufficient for s-states to be filled completely and higher states to be partly populated. An ESR signal can only be observed from unpaired electrons. This means completely filled levels – up and down spin – are ESR silent. Therefore, the single peak observed, which shows very small anisotropy in g-factor, can be attributed to extended electron wave functions in p-like states.

The ESR experiments with sub-Si-bandgap light illumination further support the above assignment of the signals. Under illumination with light the electron concentration is increased by ionization of donors. By illuminating over the time of the measurement an increased equilibrium Fermi level is established. Alternatively a generation of electron-hole pairs from the quantum dots is possible as well. However, dots are not excited resonantly, so that electrons are pumped (direct transition) in higher states and then relax back to the lowest unoccupied state.

In both possible scenarios, electrons from the conduction band are trapped in the potentials around the nanostructures populating additional dots and higher states in the individual potentials. Confined levels are filled from the lowest unoccupied state first. As more levels are filled the s-state ESR signal decreases. At the same time p-states are getting more and more populated. Therefore the increase of the intensity of the ESR signal R under illumination with sub-bandgap light means a further population of the p-states (and eventually higher states) and a filling of the s-state [Fig. 12.11 (b)]. The quantitative analysis, showing a stronger increase for the isolated dots, indeed indicates that initially (without illumination) not all quantum dots were populated in this sample.

The occupation of quantum dots is certainly not limited to s- and p-states. It is possible that peak R is a convolution of p-states and higher states, but the spectral resolution to resolve the g-factors is too low for ESR experiment at X-band frequencies and the corresponding magnetic fields. Also their energy difference ΔE_{pd} cannot be resolved at temperatures around 4 K.

12.3.3 Relaxation Times

Due to the small size and shape variation of the ensemble of quantum dots it is not expected that g-factors are identical. This causes a broadening of the ESR line. However, the spread in g-factors is obviously smaller than the difference in g-factors between the two resolved lines observed ($\Delta g \simeq 2 \cdot 10^{-4}$). Considering the abovementioned mechanisms of the inhomogeneous broadening, the ESR signal of the ensemble of spins should show a Gaussian line. Because all lines observed are of a Lorentzian form, there has to be a mechanism present that narrows the line again. Since the quantum dots are occupied by several electrons the isotropic exchange interaction between the spins at the same quantum dot seems to be the primary source of the line narrowing. Such interaction is within the spin ensemble and therefore can significantly enlarge the T_2^* time, whereby it does not affect the T_1 time directly. A secondary narrowing effect could be due to the inter-dot exchange interaction. However, we did not find a direct correlation between average inter-dot distance and the linewidth. Eventually, the extended wave functions can already cause a motional narrowing effect.

The estimated T_1-times $T_1 \approx 10\,\mu$s are longer than what was observed in Si/SiGe quantum well structures for which $T_1 \approx 1\,\mu$s [126], but significantly shorter than that of donor states in silicon [115]. Since the electrons on the quantum dots are spatially not as strongly confined as on the donors this value seems reasonable. The T_1 time is larger than the T_2^* time suggesting that the spin lattice relaxation does not contribute substantially to the spin dephasing at low temperatures. However, as the spin coherence time T_2 could be longer than T_2^* the spin lifetime T_1 could be a limiting factor for spin coherence on SiGe quantum dots.

Recently a pulsed ESR study on SiGe quantum dots was published [179]. The reported relaxation and coherence times T_2 are in good agreement with the relaxation and dephasing times T_2^* found in the structures investigated in this work [132].

12.3.4 Donors in Heterostructures

As mentioned earlier, electrons bound to donors constitute paramagnetic defects which are ESR active. Since the confinement on donors and quantum dots takes place on the same energy scale the questions arises if the

ESR signals observed can be explained by the presence of donor electrons.

In the investigated samples a n-type background doping of $2.3 \cdot 10^{16}\text{cm}^{-3}$ is present. The typical donors in Si are Sb, As and P. Sb and As can safely be excluded as dopants, since they were never present in the MBE chamber used for the sample growth. It is plausible that the background doping is partly due to phosphorus, since the chamber is equipped with a P doping chamber. Even in the reference structures the typical hyperfine splitting of P donors in Si was not observed. Thus, it is likely that the donor concentration is in fact lower than the background doping which was determined in another set of samples.

In the presence of quantum dots electrons from donors are partly transferred to the quantum dots. Nevertheless, in some of the structures investigated this should not be the case for all donor electrons. One can rationalize what a signal originating from the donor states in the heterostructure should look like: Electrons bound to donors in the vicinity of quantum dots are subject to strain, which influences the g-factor. The calculations for the g-factor dependence under strain [119] can be correlated with the calculated strain profiles of the heterostructures. In the limits of maximum biaxial tensile strain at the apex of the dot and maximal compressive strain at the base of the dots the full g-factor anisotropy $\Delta g = 1.1 \cdot 10^{-3}$ can be reached. The g-factor anisotropy of an initial donor at the apex of the dot is larger than the one observed in the quantum dot structures and the average g-factor is lower. The question of distributions of donors in the heterostructures arises. An enhanced incorporation of Sb donors in biaxially tensile strained Si was suggested, causing increased conductivity [180]. It was attributed to the relative large difference in size between Si and Sb atoms. This effect is drastically reduced for As [181]. Being of similar size than Si, it is not expected that P donors show an increased incorporation in biaxial strained Si (The covalent radii are: $r_{Si} = 111\,\text{pm}$, $r_P = 106\,\text{pm}$, $r_{As} = 119\,\text{pm}$, $r_{Sb} = 138\,\text{pm}$). Thus, a homogenous distribution of donors in Si is likely. The anisotropy of an observed g-factor can indeed be reduced by assuming a distribution of donors. However, the average g-factor g_0 is clearly smaller than the one observed in experiment. Donors can be incorporated in SiGe islands as well. Since the lowest conduction band in Ge is the L-band, only g-factors for this band were experimentally determined [116]. The g-factors for Δ-electrons in Ge can be calculated as $g_\parallel = 2.0412$ and $g_\perp = 1.8873$ [131] after [182]. A linear change between Si and Ge g-

factors according to the Ge fraction $0 < x < 0.55$ is assumed. For this g_0 shifts to even lower values, while Δg becomes larger with increasing Ge fraction. Also this scenario cannot explain the ESR spectra observed.

As discussed, a distribution of donors under the strain profile of the SiGe islands translates into different g-factors for the individual donors. This means that the ESR resonance occurs under slightly different external magnetic fields. This translates into a broadening of the ESR spectrum and a decrease in the weighted intensity. The experimentally observed donor linewidths are $2.4\,\mathrm{Oe} \leq \Delta H \leq 3.2\,\mathrm{Oe}$ [33]. This is already much larger than the linewidth observed on the heterostructures. The additional broadening due to the strain profile amounts to

$$\delta H \approx \frac{h}{\mu_B}\left(\frac{\nu}{g_{\parallel}} - \frac{\nu}{g_{\perp}}\right) \approx 2\,\mathrm{Oe} \tag{12.4}$$

with $g_{\parallel}$ and $g_{\perp}$ values according to [119] for P donors. Accordingly, the g-factor distribution inside the SiGe islands with inhomogeneous alloy distributions causes an additional broadening with a decrease in ESR intensity.

Much more significant for the broadening is the influence of the strain on the hyperfine interaction. For the P donor in unstrained Si two hyperfine split lines are observed with a distance of 42 G [33]. Under increasing biaxial strain this hyperfine splitting decreases, due to the increasing population of the doublet and eventually the triplet state. When assuming a distribution of donors under strain, the donor spectrum is broadened over the range of 42 G. The expected linewidth would then be two orders of magnitude larger than the one observed in heterostructures. The line broadening is connected to a decrease in intensity (since the integrated intensity remains constant). Therefore it is unlikely that an ESR line can be observed in the investigated system.

One other important point is that relaxation times for donor states in Si are orders of magnitude larger than the ones observed in this work [33, 115].

To summarize, the g-factor anisotropy observed cannot be explained by single donors in the strain field of SiGe islands. The considerations of distributions of donors in the material results in a spread of g-factors and distributed hyperfine splitting, consequently in a broadening of the linewidth and a decrease in intensity. From these considerations it can be concluded that the observed signals cannot be associated with electrons localized on donors.

12.4 Summary

A systematic study on SiGe heterostructures was presented. Two sets of samples, grown at different temperatures, were investigated. ESR investigations were carried out on samples with quantum dots and different reference structures. ESR investigations reveal narrow spectra only observed on samples containing quantum dots. Their g-factor $g \approx 1.999$ are close to the free electron g-factor. An axial symmetry is found with a small anisotropy of $\Delta g \approx 10^{-4}$. The behavior of g and Δg is consistent with the limiting scenarios of electrons localized on donor states and that of conduction band electrons confined to a 2DEG. The linewidth broadening observed can be explained by a Bychkov-Rashba-like spin-orbit coupling.

While on the small dots a single ESR line is found, two ESR lines are observed at the large dots. The relative population between the two lines can be changed by illumination with sub-bandgap light. The anisotropy Δg is slightly different for the two states. The ESR spectrum with larger anisotropy is attributed to quantum dots in the s-like-state, while the other spectrum corresponds to p-like-states with eventual contributions from higher populated states.

For the spin states on quantum dots the spin dephasing times T_2^* are estimated to be on the order of 0.2-0.5 μs, whereas the spin lifetimes T_1 are just below 10 μs.

CHAPTER 13

Summary and Outlook

In this part a systematic study on SiGe/Si quantum dots was presented. Two sets of SiGe heterostructures were grown at different growth temperatures. In the intentionally undoped heterostructures residual background doping is present which most likely originates from P impurities. The structures consist of four capped layers of SiGe islands. The vertical spacing between the layers was varied in individual samples. There is a significant difference in size of the quantum dots for the two growth temperatures. The base diameters are about 80 nm for dots grown at 600°C and about 200 nm for dots grown at 700°C.

Based on TEM analysis and AFM images, calculations with the program nextnano^3 were performed. Strain, electronic structure and quantum mechanical energy states were modeled. Electrons are confined in the Si on top or below the SiGe island. The confining potentially is spatially anisotropic. It exhibits a sharp boundary at the SiGe/Si interface and a smooth increase in growth direction, while it has the form of a quasi-harmonic potential for the perpendicular directions. It was found that dots with a vertical spacing of 100 nm can be regarded as completely isolated structurally and electronically. Dots spaced 70 nm apart are (partly) arranged vertically but their electronic confining potentials are still isolated. On dots with spacings of 20 nm the confined ground state is that of a joint potential of two vertically-aligned quantum dots. The energy difference between quantum dot states decreases with the increasing size of the quantum dot. It is found that the confining potential in the small dots is on the order of donor ionization energies in strained and unstrained Si. For the larger dots the energy states are on the order of donor ionization energies in SiGe and strained Si. Therefore the electron occupation of the quantum dots is low with only a few electrons per dot on average.

ESR was used to study in detail electrons confined by SiGe nanostructures. Based on electronic structure simulations the observed ESR spectra were assigned to electronic states on SiGe quantum dots. Two resonances were detected which were attributed to s- and p-like states of confined electrons on the quantum dots. By applying sub-bandgap illumination the relative population between the states can be changed. Structural differences determine the confinement of electrons and with that the population of dots under constant doping. g-factors are close to the free electron g-factor, showing only a small anisotropy with an axial symmetry. The anisotropy is stronger for the s-like state. The linewidth broadening is consistent with a Bychkov-Rashba-like spin-orbit coupling. Relaxation and dephasing times are in the range of μs.

The presented study reveals new possibilities for spintronic applications and possibilities for spintronic devices based on SiGe quantum dots. The relaxation and dephasing times determined enable spin manipulation on experimentally accessible timescales. The separation and characterization of the two states on quantum dots might even enable selective spin control with established ESR techniques on the quantum dot states themselves. The fact that both lines can be observed even for broad ensembles is synonymic to fairly low requirements on sample quality, which is advantageous for development of devices. However, structures still have to be optimized in order to increase the signal/noise ratio.

The simulations carried out for this work lay a good foundation for the design of strain engineered heterostructures and devices. The interplay between quantum dots and donor states can be influenced by varying the shape of dots and consequently their confining potentials, as well as by modifying the donor doping profiles. It is interesting to explore possibilities to facilitate the significantly different relaxation and dephasing times of donor and quantum dot states and the interactions between those states. Probing and manipulation of spin states is possible with ESR and possibly Electrical Detected Magnetic Resonance (EDMR). The proven manipulation with sub-bandgap light proves that the spin states can be manipulated simultaneously by optical means. By probing and manipulating spin states on quantum dots embedded in capacitance structures [183] electric manipulation is possible as well. The combination of these different manipulation methods allows for complex control of spintronic devices based on self-assembled SiGe quantum dots.

The interaction between different SiGe quantum dots is important, since it critically influences the coherence times on the quantum dots. The conditions under which (hopping) transport can occur laterally between dot potentials can be addressed. For this SiGe quantum dots on patterned substrates with varying distances between dots are necessary. A first study on this kind of structures did not result in an observable signal due to a low number of quantum dots and thus a low signal/ noise ratio and a significant As background doping present in these structures grown with a different MBE machine. Here the application of EDMR might also yield new insights. With EDMR the question of vertical transport in three-dimensional quantum dot crystals [122] can also be targeted.

The observation and characterization of electron states on SiGe quantum dots presented in this work, paves the way to address spin states on self-assembled SiGe quantum dots and offers new possibilities for spintronic applications and devices.

Bibliography

[1] S. A. Wolf, D. D. Awschalom, R. A. Buhrman, J. M. Daughton, S. von Molnár, M. L. Roukes, A. Y. Chtchelkanova, and D. M. Treger. *Science* **294**, 1488, 2001.

[2] H. Munekata, H. Ohno, S. von Molnar, Armin Segmüller, L. L. Chang, and L. Esaki. *Phys. Rev. Lett.* **63**, 1849, 1989.

[3] X. Jiang, R. Wang, R. M. Shelby, R. M. Macfarlane, S. R. Bank, J. S. Harris, and S. S. P. Parkin. *Phys. Rev. Lett.* **94**, 056601, 2005.

[4] Y. Kajiwara, K. Harii, S. Takahashi, J. Ohe, K. Uchida, M. Mizuguchi, H. Umezawa, H. Kawai, K. Ando, K. Takanashi, S. Maekawa, and E. Saitoh. *Nature* **464**, 262, 2010.

[5] D. Chiba, M. Sawicki, Y. Nishitani, Y. Nakatani, F. Matsukura, and H. Ohno. *Nature* **455**, 515, 2008.

[6] T. Kimura, T. Goto, H. Shintani, K. Ishizaka, T. Arima, and Y. Tokura. *Nature* **426**, 55, 2003.

[7] B. E. Kane. *Nature* **393**, 133, 1998.

[8] T. Schneider, A. A. Serga, B. Leven, B. Hillebrands, R. L. Stamps, and M. P. Kostylev. *Appl. Phys. Lett.* **92**, 022505, 2008.

[9] A. Abragam and B. Bleaney. *Electron Paramagnetic Resonance of Transition Ions.* Oxford University Press, 1970.

[10] C. P. Poole Jr. *Electron Spin Resonance: A Comprehensive Treatise on Experimental Techniques.* Dover Publications, Inc., 2nd edition, 1996.

[11] S. Blundell. *Magnetism in Condensed Matter.* Oxford Master Series in Condensed Matter Physics. Oxford University Press, 2001.

[12] C. Kittel. *Introduction to Solid State Physics.* Wiley, 7th edition, 1995.

[13] N. W. Ashcroft and N. D. Mermin. *Solid State Physics.* Thomson Learning Inc., 1976.

[14] W. Heisenberg. *Zeitschrift für Physik A Hadrons and Nuclei* **43**, 172, 1927.

[15] F. Bloch. *Phys. Rev.* **70**, 460, 1946.

[16] M. E. Flatté, J. M. Byers, and W. H. Lau. *Spin Dynamics in Semiconductors in Semiconductor Spintronics and Quantum Computation.* Nanoscience and Technology. Springer, 2002.

[17] C. P. Slichter. *Principles of Magnetic Resonance.* Springer Series in Solid State Science. Springer, 1990.

[18] H. N. Russell and F. A. Saunders. *Astrophysical Journal* **61**, 38, 1925.

[19] Y. A. Bychkov and E. I. Rashba. *Journal of Physics C: Solid State Physics* **17**, 6039, 1984.

[20] Y. A. Bychkov and E. I. Rashba. *JETP Lett.* **39**, 78, 1984.

[21] O. Kahn. *Molecular Magnetism.* John Wiley & Sons, 1993.

[22] C. Golze. PhD thesis, TU Dresden, 2007.

[23] W. Heisenberg. *Zeitschrift für Physik A Hadrons and Nuclei* **49**, 619, 1928.

[24] P. A. M. Dirac. *Proceedings of the Royal Society of London. Series A* **123**, 714, 1929.

[25] F. Ishii. *Electronic Structure of Transition Metal Oxides in Spintronics - From GMR to Quantum Information*, **40** of *Lecture Notes IFF Springschool.* Forschungszentrum Jülich GmbH Institute of Solid State Research, 2009.

[26] J. B. Goodenough. *Phys. Rev.* **100**, 564, 1955.

[27] J. B. Goodenough. *Journal of Physics and Chemistry of Solids* **6**, 287, 1958.

[28] J. Kanamori. *Journal of Physics and Chemistry of Solids* **10**, 87, 1959.

[29] P. W. Anderson. *Magnetism.* Academic Press, New York, 1963.

[30] I. Dzyaloshinsky. *Journal of Physics and Chemistry of Solids* **4**, 241, 1958.

[31] T. Moriya. *Phys. Rev.* **120**, 91, 1960.

[32] D. R. McCamey, H. Huebl, M. S. Brandt, W. D. Hutchison, J. C. McCallum, R. G. Clark, and A. R. Hamilton. *Appl. Phys. Lett.* **89**, 182115, 2006.

[33] G. Feher. *Phys. Rev.* **114**, 1219, 1959.

[34] T. Gregorkiewicz, H. H. P. Th. Bekman, and C. A. J. Ammerlaan. *Phys. Rev. B* **41**, 12628, 1990.

[35] K. Lips, P. Kanschat, and W. Fuhs. *Solar Energy Materials and Solar Cells* **78**, 513, 2003.

[36] A. R. Stegner, C. Boehme, H. Huebl, M. Stutzmann, K. Lips, and M. S. Brandt. *Nature Physics* **2**, 835, 2006.

[37] F. Bridges, G. Davies, J. Robertson, and A. M. Stoneham. *Journal of Physics: Condensed Matter* **2**, 2875, 1990.

[38] Springer Materials - The Landolt-Börnstein Database
Subvolume a2a - Group IV Elements - Impurities and Defects in Group IV Elements, IV-IV and III-V Compounds.

[39] J. Behrends, A. Schnegg, M. Fehr, A. Lambertz, S. Haas, F. Finger, B. Rech, and K. Lips. *Philosophical Magazine* **89**, 2655, 2009.

[40] D. J. Lepine. *Phys. Rev. B* **6**, 436, 1972.

[41] I. Solomon. *Solid State Communications* **20**, 215, 1976.

[42] R. Zahn. Master's thesis, IFW Dresden/ TU Dresden, 2011.

[43] B. Johansson, S. Haraldson, L. Pettersson, and O. Beckman. *Review of Scientific Instruments* **45**, 1445, 1974.

[44] W. J. Wallace and R. H. Silsbee. *Review of Scientific Instruments* **62**, 1754, 1991.

[45] G. Boero, M. Bouterfas, C. Massin, F. Vincent, P.-A. Besse, R. S. Popovic, and A. Schweiger. *Review of Scientific Instruments* **74**, 4794, 2003.

[46] R. Narkowicz, D. Suter, and R. Stonies. *Journal of Magnetic Resonance* **175**, 275, 2005.

[47] M. Rohrer, J. Krzystek, V. Williams, and L.-C. Brunel. *Measurement Science and Technology* **10**, 275, 1999.

[48] G. Annino, M. Cassettari, I. Longo, M. Martinelli, P. J. M. Van Bentum, and E. Van der Horst. *Review of Scientific Instruments* **70**, 1787, 1999.

[49] G. Annino, M. Cassettari, M. Fittipaldi, I. Longo, M. Martinelli, C. A. Massa, and L. A. Pardi. *Journal of Magnetic Resonance* **143**, 88, 2000.

[50] M. Mola, S. Hill, P. Goy, and M. Gross. *Review of Scientific Instruments* **71**, 186, 2000.

[51] T. H. Oosterkamp, T. Fujisawa, W. G. van der Wiel, K. Ishibashi, R. V. Hijman, S. Tarucha, and L. P. Kouwenhoven. *Nature* **395**, 873, 1998.

[52] Waveguide loss - microwaves101.com
http://www.microwaves101.com/encyclopedia/waveguideloss.cfm
(as of 06/2011).

[53] J. D. Jackson. *Electrodynamics.* John Wiley & Sons, 1998.

[54] Skindepth calculator - microwaves101.com
http://www.microwaves101.com/encyclopedia/calsdepth.cfm
(as of 06/2011).

[55] T. Kimura. *Annual Review of Materials Research* **37**, 387, 2007.

[56] L. J. De Jongh, editor. *Magnetic properties of Layered Transition Metal Compounds.* Kluwer Academic Publishers, 1990.

[57] E. Ising. *Zeitschrift für Physik A Hadrons and Nuclei* **31**, 253, 1925.

[58] M. Verdaguer J. P. Renard, L. P. Regnault. *Magnetism: Molecules to Materials - Models and Experiments.* Wiley-VCH, 2001.

[59] A. Einstein and O. Stern. *Annalen der Physik* **40**, 551, 1913.

[60] N. D. Mermin and H. Wagner. *Phys. Rev. Lett.* **17**, 1133, 1966.

[61] V. L. Berezinskii. *Sov. Phys. JETP* **32**, 493, 1971.

[62] H. Manaka, I. Yamada, and K. Yamaguchi. *Journal of the Physical Society of Japan* **66**, 564, 1997.

[63] F. D. M. Haldane. *Phys. Rev. Lett.* **50**, 1153, 1983.

[64] I. Affleck, T. Kennedy, E. H. Lieb, and H. Tasaki. *Phys. Rev. Lett.* **59**, 799, 1987.

[65] J. P. Renard, M. Verdaguer, L. P. Regnault, W. A. C. Erkelens, J. Rossat-Mignod, and W. G. Stirling. *Europhysics Lett.* **3**, 945, 1987.

[66] M. Sieling, W. Palme, and B. Lüthi. *Zeitschrift für Physik B Condensed Matter* **96**, 297, 1995.

[67] G. Kamieniarz, M. Bieliński, G. Szukowski, R. Szymczak, S. Dyeyev, and J.-P. Renard. *Computer Physics Communications* **147**, 716, 2002.

[68] M. Baran, A. Jedrzejczak, H. Szymczak, V. Maltsev, G. Kamieniarz, G. Szukowski, C. Loison, A. Ormeci, S.-L. Drechsler, and H. Rosner. *physica status solidi (c)* **3**, 220, 2006.

[69] R. Szymczak, H. Szymczak, G. Kamieniarz, G. Szukowski, K. J. Pacer, W. Florek, V. Maltsev, and G.-J. Babonas. *Acta Physica Polonica A* **115**, 925, 2009.

[70] B. M. Sudhana, B. J. Reddy, S. Vedanand, Y. P. Reddy, and P. S. Rao. *Radiation Effects and Defects in Solids: Incorporating Plasma Science and Plasma Technology* **133**, 217, 1995.

[71] P. F. Schofield, C. C. Wilson, K. S. Knight, and C. A. Kirk. *The Canadian Mineralogist* **47**, 649, 2009.

[72] A. U. B. Wolter, F. Lipps, M. Schäpers, S.-L. Drechsler, S. Nishimoto, R. Vogel, M. Uhlarz, Y. Skourski, M. Schmitt, H. Rosner, K. C. Rule, S. Süllow, G. Heide, V. Kataev, and B. Büchner. *submitted to PRB*, 2011.

[73] M. Enderle, C. Mukherjee, B. Fåk, R. K. Kremer, J.-M. Broto, H. Rosner, S.-L. Drechsler, J. Richter, J. Malek, A. Prokofiev, W. Assmus, S. Pujol, J.-L. Raggazzoni, H. Rakoto, M. Rheinstädter, and H. M. Rønnow. *Europhys. Lett.* **70**, 237, 2005.

[74] M. G. Banks, F. Heidrich-Meisner, A. Honecker, H. Rakoto, J.-M. Broto, and R. K. Kremer. *Journal of Physics: Condensed Matter* **19**, 145227, 2007.

[75] M. Sato, T. Momoi, and A. Furusaki. *Phys. Rev. B*, **79**, 060406, 2009.

[76] S. Nishimoto, S.-L. Drechsler, R. Kuzian, J. Richter, and J. van den Brink. *submitted to PRL*, 2010.

[77] D. L. Huber. *Phys. Rev. B* **6**, 3180, 1972.

[78] P. M. Richards. *Solid State Communications* **13**, 253, 1973.

[79] Y. Tazuke and K. Nagata. *Journal of the Physical Society of Japan* **38**, 1003–1010, 1975.

[80] A. F. M. Arts, H. van der Vlist, J.G.M. van Miltenburg, C.M.J. van Uijen, and H.W. de Wijn. *Journal of Magnetism and Magnetic Materials* **31-34**, 1181, 1983.

[81] A. U. B. Wolter and et al. *to be published*, 2011.

[82] Y. Yasui, M. Sato, and I. Terasaki. *Journal of the Physical Society of Japan* **80**, 033707, 2011.

[83] H. Sirringhaus, N. Tessler, and R. H. Friend. *Science* **280**, 1741, 1998.

[84] J. J. M. Halls, C. A. Walsh, N. Greenham, E. A. Marseglia, R. Friend, S. C. Moratti, and A. Holmes. *Nature* **376**, 498, 1995.

[85] G. Yu, J. Gao, J. C. Hummelen, F. Wudl, and A. J. Heeger. *Science* **270**, 1789, 1995.

[86] A. Arkenbout. PhD thesis, University of Groningen Zernike Institute for Advanced Materials, 2010.

[87] J. Ribas, M. Monfort, C. Diaz, C. Bastos, C. Mer, and X. Solans. *Inorganic Chemistry* **34**, 4986, 1995.

[88] C. Y. Weng. PhD thesis, Carnegie Institute of Technology, 1968.

[89] Y. Uchiyama, Y. Sasago, I. Tsukada, K. Uchinokura, A. Zheludev, T. Hayashi, N. Miura, and P. Böni. *Phys. Rev. Lett.* **83**, 632, 1999.

[90] T. Masuda, K. Uchinokura, T. Hayashi, and N. Miura. *Phys. Rev. B* **66**, 174416, 2002.

[91] M. Hase, M. Hagiwara, and K. Katsumata. *Phys. Rev. B* **54**, R3722, 1996.

[92] A. I. Smirnov, V. N. Glazkov, H.-A. Krug von Nidda, A. Loidl, L. N. Demianets, and A. Ya. Shapiro. *Phys. Rev. B* **65**, 174422, 2002.

[93] K. M. Kojima, Y. Fudamoto, M. Larkin, G. M. Luke, J. Merrin, B. Nachumi, Y. J. Uemura, M. Hase, Y. Sasago, K. Uchinokura, Y. Ajiro, A. Revcolevschi, and J.-P. Renard. *Phys. Rev. Lett.* **79**, 503, 1997.

[94] M. Hagiwara, K. Katsumata, I. Affleck, B. I. Halperin, and J. P. Renard. *Phys. Rev. Lett.* **65**, 3181, 1990.

[95] I. Affleck. *Phys. Rev. B* **46**, 9002, 1992.

[96] A. I. Smirnov, V. N. Glazkov, T. Kashiwagi, S. Kimura, M. Hagiwara, K. Kindo, A. Ya. Shapiro, and L. N. Demianets. *Phys. Rev. B* **77**, 100401, 2008.

[97] H.-A. Krug von Nidda, N. Böttgen, and A. Loidl. *The European Physical Journal - Special Topics* **180**, 161, 2009.

[98] B. Pahari, K. Ghoshray, R. Sarkar, and A. Ghoshray. *Phys. Rev. B* **77**, 224429, 2008.

[99] E. A. Turov. *Physical Properties of Magnetically Ordered Crystals.* Academic Press, New York and London, 1965.

[100] S. Foner. *Magnetism.* Academic, New York, 1963.

[101] M. Hase, I. Terasaki, and K. Uchinokura. *Phys. Rev. Lett.* **70**, 3651, 1993.

[102] I. S. Jacobs, J. W. Bray, H. R. Hart, L. V. Interrante, J. S. Kasper, G. D. Watkins, D. E. Prober, and J. C. Bonner. *Phys. Rev. B* **14**, 3036, 1976.

[103] H. Fukuyama, N. Nagaosa, M. Saito, and T. Tanimoto. *Journal of the Physical Society of Japan* **65**, 2377, 1996.

[104] S. B. Oseroff, S-W. Cheong, B. Aktas, M. F. Hundley, Z. Fisk, and L. W. Rupp Jr. *Phys. Rev. Lett.* **74**, 1450, 1995.

[105] M. Honda, T. Shibata, K. Kindo, S. Sugai, T. Takeuchi, and H. Hori. *Journal of the Physical Society of Japan* **65**, 691, 1996.

[106] M. Hase. *Journal of Magnetism and Magnetic Materials* **177-181** 611, 1998.

[107] A. K. Hassan, L. A. Pardi, G. B. Martins, G. Cao, and L-C. Brunel. *Phys. Rev. Lett.* **80**, 1984, 1998.

[108] B. Grenier, P. Monod, M. Hagiwara, M. Matsuda, K. Katsumata, S. Clément, J.-P. Renard, A. L. Barra, G. Dhalenne, and A. Revcolevschi. *Phys. Rev. B* **65**, 094425, 2002.

[109] V. N. Glazkov, A. I. Smirnov, K. Uchinokura, and T. Masuda. *Phys. Rev. B* **65**, 144427, 2002.

[110] M. Date and K. Kindo. *Phys. Rev. Lett.* **65**, 1659, 1990.

[111] S. J. Blundell. *Contemporary Physics* **40**, 175, 1999.

[112] M. I. Dyakonov, editor. *Spin Physics in Semiconductors.* Number 157 in Springer Series in Solid-State Sciences. Springer, 2008.

[113] A. V. Khaetskii, D. Loss, and L. Glazman. *Phys. Rev. Lett.* **88**, 186802, 2002.

[114] A. Ferretti, M. Fanciulli, A. Ponti, and A. Schweiger. *Phys. Rev. B* **72**, 235201, 2005.

[115] G. Feher and E. A. Gere. *Phys. Rev.* **114**, 1245, 1959.

[116] G. Feher, D. K. Wilson, and E. A. Gere. *Phys. Rev. Lett.* **3**, 25, 1959.

[117] L. M. Roth and B. Lax. *Phys. Rev. Lett.* **3**, 217, 1959.

[118] L. M. Roth. *Phys. Rev.* **118**, 1534, 1960.

[119] D. K. Wilson and G. Feher. *Phys. Rev.* **124**, 1068, 1961.

[120] J. J. L. Morton, A.M. Tyryshkin, R. M. Brown, S. Shankar, B. W. Lovett, A. Ardavan, T. Schenkel, E. E. Haller, J. W. Ager, and S. A. Lyon. *Nature* **455**, 1085, 2008.

[121] K. Brunner. *Rep. Prog. Phys.* **65**, 27, 2002.

[122] D. Grützmacher, T. Fromherz, C. Dais, J. Stangl, E. Müller, Y. Ekinci, H. H. Solak, H. Sigg, R. T. Lechner, E. Wintersberger, S. Birner, V. Holác, and G. Bauer. *Nano Letters* **7**, 3150, 2007.

[123] M. Friesen, P. Rugheimer, D. E. Savage, M. G. Lagally, D. W. van der Weide, R. Joynt, and M. A. Eriksson. *Phys. Rev. B* **67**, 121301, 2003.

[124] P. S. Fodor and J. Levy. *Journal of Physics: Condensed Matter* **18** S745, 2006.

[125] G. Abstreiter, H. Brugger, T. Wolf, H. Jorke, and H. J. Herzog. *Phys. Rev. Lett.* **54**, 2441, 1985.

[126] A. M. Tyryshkin, S. A. Lyon, W. Jantsch, and F. Schaffler. *Phys. Rev. Lett.* **94**, 126802, 2005.

[127] Z. Wilamowski, W. Jantsch, H. Malissa, and U. Rossler. *Phys. Rev. B* **66**, 195315, 2002.

[128] C. G. Van de Walle and R. M. Martin. *Phys. Rev. B* **34**, 5621, 1986.

[129] O. G. Schmidt, K. Eberl, and Y. Rau. *Phys. Rev. B* **62**, 16715, 2000.

[130] H. Malissa, W. Jantsch, G. Chen, D. Gruber, H. Lichtenberger, F. Schäffler, Z. Wilamowski, A. Tyryshkin, and S. Lyon. *Materials Science and Engineering: B* **126**, 172, 2006.

[131] A. F. Zinovieva, A. V. Dvurechenskii, N. P. Stepina, A. S. Deryabin, A. I. Nikiforov, R. M. Rubinger, N. A. Sobolev, J. P. Leitao, and M. C. Carmo. *Phys. Rev. B* **77**, 115319, 2008.

[132] F. Lipps, F. Pezzoli, M. Stoffel, C. Deneke, J. Thomas, A. Rastelli, V. Kataev, O. G. Schmidt, and B. Büchner. *Phys. Rev. B* **81**, 125312, 2010.

[133] F. Lipps, F. Pezzoli, M. Stoffel, A. Rastelli, V. Kataev, O. G. Schmidt, and B. Büchner. *Journal of Physics: Conference Series* **200**, 062010, 2010.

[134] F. Lipps, F. Pezzoli, M. Stoffel, Ch. Deneke, J. Thomas, A. Rastelli, V. Kataev, O. G. Schmidt, and B. Büchner. *Journal of Physics: Conference Series* **245**, 012026, 2010.

[135] C. A. Hogarth, editor. *Materials used in Semiconductor Devices.* Interscience, 1965.

[136] Collaboration: Authors and editors of the volumes III/17A-22A-41A1a. *Si/Ge Lattice Parameters.* SpringerMaterials - The Landolt-Börnstein Database
http://www.springermaterials.com.

[137] J. W. Matthews and A. E. Blakeslee. *Journal of Crystal Growth* **27**, 118, 1974.

[138] J. Tersoff and F. K. LeGoues. *Phys. Rev. Lett.* **72**, 3570, 1994.

[139] I. N. Stranski and L. Krastanov. *Akad.Wiss. Lit. Mainz Math.-Natur. Kl. IIb* **146**, 797, 1939.

[140] D. J. Eaglesham and M. Cerullo. *Phys. Rev. Lett.* **64**, 1943, 1990.

[141] U. Denker, M. Stoffel, and O. G. Schmidt. *Phys. Rev. Lett.* **90**, 196102, 2003.

[142] U. Denker. PhD thesis, Universität Hannover, 2003.

[143] T. U. Schülli, M. Stoffel, A. Hesse, J. Stangl, R. T. Lechner, E. Wintersberger, M. Sztucki, T. H. Metzger, O. G. Schmidt, and G. Bauer. *Phys. Rev. B* **71**, 035326, 2005.

[144] F. K. LeGoues, M. C. Reuter, J. Tersoff, M. Hammar, and R. M. Tromp. *Phys. Rev. Lett.* **73**, 300, 1994.

[145] M. Hammar, F. K. LeGoues, J. Tersoff, M. C. Reuter, and R. M. Tromp. *Surface Science* **349**, 129, 1996.

[146] X. H. Liu, F. M. Ross, and K. W. Schwarz. *Phys. Rev. Lett.* **85**, 4088, 2000.

[147] J. Stangl, V. Holý, and G. Bauer. *Rev. Mod. Phys.* **76**, 725, 2004.

[148] A. Rastelli, M. Stoffel, U. Denker, T. Merdzhanova, and O. G. Schmidt. *physica status solidi (a)* **203**, 3506, 2006.

[149] O. G. Schmidt, U. Denker, S. Christiansen, and F. Ernst. *Appl. Phys. Lett.* **81**, 2614, 2002.

[150] G. Katsaros, M. Stoffel, A. Rastelli, O. G. Schmidt, K. Kern, and J. Tersoff. *Appl. Phys. Lett.* **91**, 013112, 2007.

[151] L. Vegard. *Zeitschrift für Physik A Hadrons and Nuclei* **5**, 17, 1921.

[152] J. P. Dismukes, L. Ekstrom, and R. J. Paff. *The Journal of Physical Chemistry* **68** 3021, 1964.

[153] C. G. Van de Walle. *Phys. Rev. B* **39**, 1871, 1989.

[154] R. People. *Phys. Rev. B* **32**, 1405, 1985.

[155] J. Stangl, T. Roch, G. Bauer, I. Kegel, T. H. Metzger, O. G. Schmidt, K. Eberl, O. Kienzle, and F. Ernst. *Appl. Phys. Lett.* **77**, 3953, 2000.

[156] Qianghua Xie, Anupam Madhukar, Ping Chen, and Nobuhiko P. Kobayashi. *Phys. Rev. Lett.* **75**, 2542, 1995.

[157] A. A. Darhuber, P. Schittenhelm, V. Holý, J. Stangl, G. Bauer, and G. Abstreiter. *Phys. Rev. B* **55**, 15652, 1997.

[158] O. Kienzle, F. Ernst, M. Rühle, O. G. Schmidt, and K. Eberl. *Appl. Phys. Lett.* **74**, 269, 1999.

[159] S. Birner, T. Zibold, T. Andlauer, T. Kubis, M. Sabathil, A. Trellakis, and P. Vogl. *IEEE Trans. Electron Devices* **54**, 2137, 2007.

[160] J. A. Majewski, S. Birner, A. Trellakis, M. Sabathil, and P. Vogl. *physica status solidi (c)* **1**, 2003, 2004.

[161] S. Hackenbuchner. PhD thesis, TU München, 2002.

[162] M. Sabathil. PhD thesis, TU München, 2004.

[163] T. Zibold. PhD thesis, TU München, 2007.

[164] Online documentation nextnano
http://www.nextnano.de/nextnano3/, .

[165] Source code as of 2004/08/24
http://www.nextnano.de/nextnano3/, .

[166] Arpack software
http://www.caam.rice.edu/software/arpack/
as of 06/2011.

[167] M. M. Rieger and P. Vogl. *Phys. Rev. B* **48**, 14276, 1993.

[168] Y. P. Varshni. Temperature dependence of the energy gap in semiconductors. *Physica* **34**, 149, 1967.

[169] R. Krüssmann, H. Vollmer, and R. Labusch. *physica status solidi (b)* **118**, 275, 1983.

[170] S. M. Sze. *Physics of Semiconductor Devices.* John Wiley & Sons, 2nd edition, 1981.

[171] S. Lebib, M. Schoisswohl, J. L. Cantin, and H. J. von Bardeleben. *Thin Solid Films* **294**, 242, 1997.

[172] J. L. Cantin and H. J. von Bardeleben. *Journal of Non-Crystalline Solids* **303**, 175, 2002.

[173] C. F. Young, E. H. Poindexter, G. J. Gerardi, W. L. Warren, and D. J. Keeble. *Phys. Rev. B* **55**, 16245, 1997.

[174] W. Kohn and J. M. Luttinger. *Phys. Rev.* **98**, 915, 1955.

[175] R. C. Fletcher, W. A. Yager, G. L. Pearson, and F. R. Merritt. *Phys. Rev.* **95**, 844, 1954.

[176] E. I. Rashba. *Sov. Phys. Solid State* **2**, 1109, 1960.

[177] J. L. Truitt, K. A. Slinker, K. L. M. Lewis, D. E. Savage, Charles Tahan, L. J. Klein, J. O. Chu, P. M. Mooney, A. M. Tyryshkin, D. W. van der Weide, R. Joynt, S. N. Coppersmith, M. Friesen, and M. A. Eriksson. In M. Fanciulli, editor, *Electron Spin Resonance and related Phenomena in low-dimensional Structures,* **115** of *Topics in Applied Physics* Springer-Verlag Berlin, 2009.

[178] T. P. Mayer Alegre, F. G. G. Hernandez, A. L. C. Pereira, and G. Medeiros-Ribeiro. *Phys. Rev. Lett.* **97**, 236402, 2006.

[179] A. F. Zinovieva, A. V. Dvurechenskii, N. P. Stepina, A. I. Nikiforov, A. S. Lyubin, and L. V. Kulik. *Phys. Rev. B* **81**, 113303, 2010.

[180] N. S. Bennett, N. E. B. Cowern, A. J. Smith, R. M. Gwilliam, B. J. Sealy, L. O'Reilly, P. J. McNally, G. Cooke, and H. Kheyrandish. *Appl. Phys. Lett.* **89**, 182122, 2006.

[181] N. Sugii, S. Irieda, J. Morioka, and T. Inada. *Journal of Applied Physics* **96**, 261, 2004.

[182] L. Liu. *Phys. Rev. Lett.* **6**, 683, 1961.

[183] S. Ketharanathan, S. Sinha, J. Shumway, and J. Drucker. *Journal of Applied Physics* **105**, 044312, 2009.

Acknowledgements

This work would not have been possible without the help and various support from many different parties. Especially, I would like to thank:

Prof. Dr. Bernd Büchner, for giving me the wonderful opportunity to carry out my research at the IFW and for giving important stimuli to this work.

Prof. Dr. T. Schäpers for agreeing to review this thesis.

Dr. Vladislav Kataev, for his comprehensive explanations and general support. As the leader of the ESR group he allowed me to pursue projects with great freedom and was always available for helpful suggestions and stimulating discussions about experiments and all matters concerning this work. I am grateful to him for giving me the opportunity to spend time at the Zavoisky Physical-Technical Institute in Kazan.

Prof. Dr. Oliver G. Schmidt for his interest and his suggestions regarding the work on the SiGe quantum dots.

Dr. Armando Rastelli for his support and coordination of the SiGe quantum dot project from the side of the IIN. Although usually busy he was always willing to meet and to provide helpful suggestions and ideas.

Prof. Dr. Vladimir Fomin for many discussions about modeling in general and modeling with nextnano^3 in particular.

Dr. Mathieu Stoffel for providing the SiGe quantum dot samples and Dr. Christoph Deneke for performing the TEM images.

I cannot cherish enough the help of Dr. Fabio Pezzoli, who did not only grow

the SiGe quantum dot samples and conducted AFM and PL measurements, but who always was available for discussions and from whom I learned a lot about the SiGe systems. I am also very grateful for his critical reading of parts of this thesis.

All members of the ESR group during the time of my PhD, for help with experiments, many discussions and shared hours spent in the laboratory: Dr. Ferenc Murányi, Dr. Uwe Schaufuß, Dr. Mohammed Yehia Taha Ahmed Elbahrawy, Dr. Andreas Petr, Dr. Yulieth Arango, Alexey Alfonsov and Yulia Krupskaya. Especially Dr. Stefan Bahr for the joint work on the setups for electrical detected magnetic resonance and for reading parts of this thesis.

Dr. Jan Behrends and Dr. Klaus Lips from the Helmholtz Zentrum Berlin for their help and providing their know-how of EDMR setups.

Dr. Ruslan Zaripov for his work and hospitality during my time at the Zavoisky Physical-Technical Institute in Kazan.

Dr. Anja Wolter for many discussions about low-dimensional spin systems, in particular about Linarite, Dr. Anne Arkenbout for providing us samples of the Ni-hybrid and Hemke Maeter for the μSR measurements on it and many helpful discussions.

Dr. Ralf Voigtländer and the IFW Forschungstechnik for discussions and help on the work of the microwave resonators. As a representative of the IFW workshop Steffen Grundkowski, who always did his best to realize my projects in a timely manner. Falk Herold who was a great help with all those little and not so little mechanical constructions which can make life in the laboratory difficult when not available quickly. Regina Vogel for the support with the administrative work in and around the laboratory.

My office roommates Franziska Hammerath, Dr. Guillaume Manilal Lang and Alexey Alfonsov for many scientific and not quite so scientific discussions.

Finally, I would like to thank my whole family and especially Angela for their emotional support during the time of my PhD.

Eigenständigkeitserklärung

Hiermit versichere ich, dass ich die vorliegende Arbeit ohne unzulässige Hilfe Dritter und ohne Benutzung anderer als der angegebenen Hilfsmittel angefertigt habe; die aus fremden Quellen direkt oder indirekt übernommenen Gedanken sind als solche kenntlich gemacht. Die Arbeit wurde bisher weder im Inland noch im Ausland in gleicher oder ähnlicher Form einer anderen Prüfungsbehörde vorgelegt.

Diese Arbeit wurde unter Betreuung von Prof. Dr. B. Büchner am Institut für Festkörperforschung (IFF) des Instituts für Festkörper- und Werkstoffforschung Dresden e.V. (IFW Dresden) angefertigt.

Ich erkenne hiermit die Promotionsordnung der TU Dresden an.

Dresden, den 10.06.2011